

Development of pathfinder missions and instruments  
for the Pacific Ocean Neutrino Experiment

---

Christian Spannfellner

April 15, 2020

Master Thesis



Chair of Experimental Physics with Cosmic Particles

**Supervisor:** Prof. Dr. Elisa Resconi  
**Second assessor:** Prof. Dr. Susanne Mertens



## Abstract

Astroparticle physics enables the study of astrophysical processes and fundamental physics via the observation of cosmic rays, gamma rays, neutrinos, and gravitational waves. The combined detection of those messengers grants a complementary view on the underlying processes and is called multi-messenger astronomy. High energy neutrino astronomy is thereby an essential pillar and relies on the instrumentation of large transparent volumes with photosensor arrays to detect Cherenkov radiation induced by neutrino-matter interactions. The IceCube Upgrade and the Pacific Ocean Neutrino Experiment, which will be discussed within this thesis, aim for an even deeper exploration of the neutrino sky.

After an introduction to astroparticle physics and neutrino detection, the first part of this thesis will cover the development of a third generation calibration module for neutrino telescopes. The Precision Optical Calibration Module is a universal calibration instrument, which emits isotropic light pulses in the nanosecond regime to calibrate the photosensor arrays and access the optical properties of the instrumented volume. The concept has been already successfully tested in the Gigaton Volume Detector at Lake Baikal and ultimately led to the installation of a first pathfinder for the Pacific Ocean Neutrino Experiment. The second part of this thesis introduces these pathfinder missions. The objective of the first pathfinder was to measure the optical properties of the deep seawater at the Cascadia Basin in the north-eastern Pacific. The second pathfinder has been developed over the past year at the Technical University Munich with the main goals of further background characterization, verification of the measured attenuation length, and the development of a suitable deployment strategy for future Pacific Ocean Neutrino Experiment mooring lines. This thesis concludes with a technical design study of a Pacific Ocean Neutrino Experiment mooring line, based on the module developments and gained experiences from the pathfinder missions.

# Contents

<b>1</b>	<b>Astroparticle physics introduction</b>	<b>1</b>
1.1	Cosmic rays . . . . .	1
1.2	Cosmic accelerators . . . . .	4
1.3	Cosmic messengers . . . . .	6
<b>2</b>	<b>Neutrino detection</b>	<b>9</b>
2.1	Neutrino interactions . . . . .	9
2.1.1	Cherenkov effect . . . . .	9
2.1.2	Neutrino oscillations . . . . .	10
2.1.3	Neutrino signatures . . . . .	11
2.2	Neutrino sources . . . . .	13
2.3	Neutrino detectors . . . . .	15
2.4	Prospects of neutrino astronomy . . . . .	17
2.4.1	IceCube Upgrade . . . . .	18
2.4.2	Pacific Ocean Neutrino Experiment . . . . .	18
<b>3</b>	<b>Precision Optical Calibration Module</b>	<b>21</b>
3.1	Motivation . . . . .	21
3.2	POCAM design . . . . .	22
3.2.1	Titanium housing . . . . .	23
3.2.2	Internal construction . . . . .	24
3.3	Isotropy . . . . .	25
3.4	Flasher circuits . . . . .	27
3.4.1	Kapustinsky . . . . .	28
3.4.2	LiDAR-type pulser . . . . .	30
3.4.3	Redundancy modifications . . . . .	31
3.5	Optical emitter selection . . . . .	34
3.6	Photosensor self-monitoring . . . . .	35
3.6.1	Photodiode readout . . . . .	36
3.6.2	Silicon-photomultiplier readout . . . . .	37
3.7	Communication and power electronics . . . . .	38
3.8	Characterization setups . . . . .	39
3.9	Conclusion and outlook on the POCAM activities . . . . .	41
<b>4</b>	<b>Pathfinder missions for P-ONE</b>	<b>43</b>
4.1	STRAW - Strings for absorption length in water . . . . .	43
4.2	STRAW-b . . . . .	46
4.2.1	Standard modules . . . . .	46
4.2.2	Specialized modules . . . . .	49
4.2.3	Deployment strategy . . . . .	50
4.2.4	The instrument tray for the STRAW-b deployment . . . . .	56
4.2.5	Qualification of the module mechanics . . . . .	60

**5 P-ONE mooring line design study 63**

**6 Conclusion and outlook 67**

**A Appendix 69**

    A.1 POCAM . . . . . 69

    A.2 STRAW . . . . . 75



# 1 Astroparticle physics introduction

The field of astroparticle physics covers the intersection between astrophysics and particle physics. The goal of astroparticle physics is therefore two-fold: studying particle physics by means of particles arriving from outer space as well as drawing conclusions about astrophysical processes through those particles. The field has its roots in the discovery of cosmic rays by Victor Hess 1912, which remained the main source of new experimental insight into particle physics for decades, until the dawn of earth-based particle accelerators. Today, cosmic rays still provide insight at energy scales not achievable by accelerators. Presently, the field of cosmic rays presents still various pressing questions related to the origin and the acceleration mechanisms of these extreme particles. Some of the best source candidates for the origin of cosmic rays are correlated with supernova explosions and other even more violent processes in the universe [1, p. 7]. A better understanding of the underlying principles of cosmic ray acceleration may also provide knowledge about the formation of our solar system and galaxy [2, p. 2]. The localization of possible cosmic ray accelerators by observing cosmic rays is difficult as the presence of interstellar and intergalactic magnetic fields deflect charged particles. A combined observation of various cosmic messengers, such as gamma rays, neutrinos, and gravitational waves, is possible by using modern experimental techniques and has great potential in astrophysics. This integrated method to study astrophysical objects is called *multi-messenger astronomy*. The multi-messenger approach to astroparticle physics can be exploited in different ways. The combination of data from different messengers can boost the detection significance of a specific event. A combined data set allows also for more comprehensive modeling of the underlying physical processes. Lastly, in case of pointing observations like it is the case for, among other, radio, optical or ground-based gamma ray observatories, other messengers with large field-of-view, or full-sky capabilities (gravitational waves, neutrinos, space-borne gamma ray instruments) can be used for triggering follow-up observations [3]. The following section introduces cosmic rays, as they are the trigger point for high energy astroparticle physics.

## 1.1 Cosmic rays

Primary cosmic rays are ionized nuclei composed of high energy protons, alpha particles, and heavier nuclei. They fill up space and hit Earth's atmosphere with a rate of around thousand per square meter per second [2, p. 1]. Triggered by collisions of cosmic rays with nucleons in Earth's atmosphere cascades of secondary particles, so-called air showers, are generated. For a cosmic ray proton and a nucleon  $N$  the basic reaction is [1, p. 8]:

$$p + N \rightarrow \pi^{\pm}, \pi^0, K^{\pm}, K^0, p, n, \dots \quad (1.1)$$

Follow-up reactions through pion and kaon decays make up the three main stages of air shower development. The hadronic component is mainly composed of neutrons, protons, kaons, pions, and strongly interacts with nuclei in the air, producing a cascade of hadronic particles with variable energies.  $\pi^{\pm}$  and  $K^{\pm}$  decay and generate a weakly interacting muonic and neutrino

component. Muons with relativistic energies are produced in the shower, capable of reaching Earth's surface even though their lifespan is short. An electromagnetic component is added via the decay of pions and the subsequent production of positrons and electrons. Here, the decay of neutral pions plays a dominant role.

$$\pi^0 \rightarrow \gamma + \gamma \quad (1.2)$$

The hereby induced photons can have energies sufficient for pair production. Besides, photons are also generated by bremsstrahlung of charged particles.

The cosmic ray spectrum as it is shown in figure 1.1, is measured by two major types of experiments. Space-located or airborne instruments measure directly primary cosmic rays while ground-based experiments observe secondary particles induced by the air shower processes. Direct-detection experiments located in space or in the upper atmosphere, such as AMS-02, PAMELA or CREAM [1], are limited to energies lower than  $10^{15}$  eV as the cosmic ray flux drops below 10 events per square meter per year [1, p.87]. Ground-based experiments, which measure the cosmic ray spectra via secondary particles, cover higher energies as they feature larger detector areas, up to thousands of square kilometers [4]. The Pierre-Auger-Observatory located in Argentina is the largest of those earth-based observatories [1].

Particle spectra for non-thermal fluxes, as it is the case for cosmic rays, are described by a power law.

$$\frac{d\Phi}{dE} = A \cdot E^{-\alpha} \quad (1.3)$$

This can be represented as straight line in a double logarithmic depiction. The slope of the line is described by the spectral index  $\alpha$  while A corresponds to the intercept with the ordinate (y-axis) [1, p.9]. As the cosmic ray flux covers a vast energy range ( $10^{12}$  GeV up to  $10^{20}$  GeV) and the flux decreases with increasing energy this technique is also applied to figure 1.1. Additionally a weighting factor  $E^\beta$  for the y-axis can be included in order to flatten a falling spectrum to look for distinct features [1, p.9]. The value of  $\beta$  is variable and depends on the slope of the flux for the corresponding energy ranges [2, p.3].

$$\log \left[ E^\beta \cdot \frac{d\Phi}{dE} \right] = \log \left[ A \cdot E^{-\alpha+\beta} \right] = \log [A] - (\alpha - \beta) \cdot \log [E] \quad (1.4)$$

Three distinctive features are differentiable from the global cosmic ray spectrum. These areas are also separating regions with different spectral indices ranging from about  $\alpha \sim -2.5$  to  $\alpha \sim -3.1$ . At an energy of around  $3 \cdot 10^{15}$  eV the transition region is known as *knee* and marks presumably the maximum energy transferable to cosmic rays via shock acceleration by supernova remnants (SNRs). The second feature known as *ankle* is theorized to flag the advent of particles with an extra-galactic origin. It is situated at roughly  $3 \cdot 10^{18}$  eV [2, p.12, 341]. This hypothesis emerges from the fact that cosmic rays are charged particles and thus are deflected by galactic magnetic fields [1, p.203].

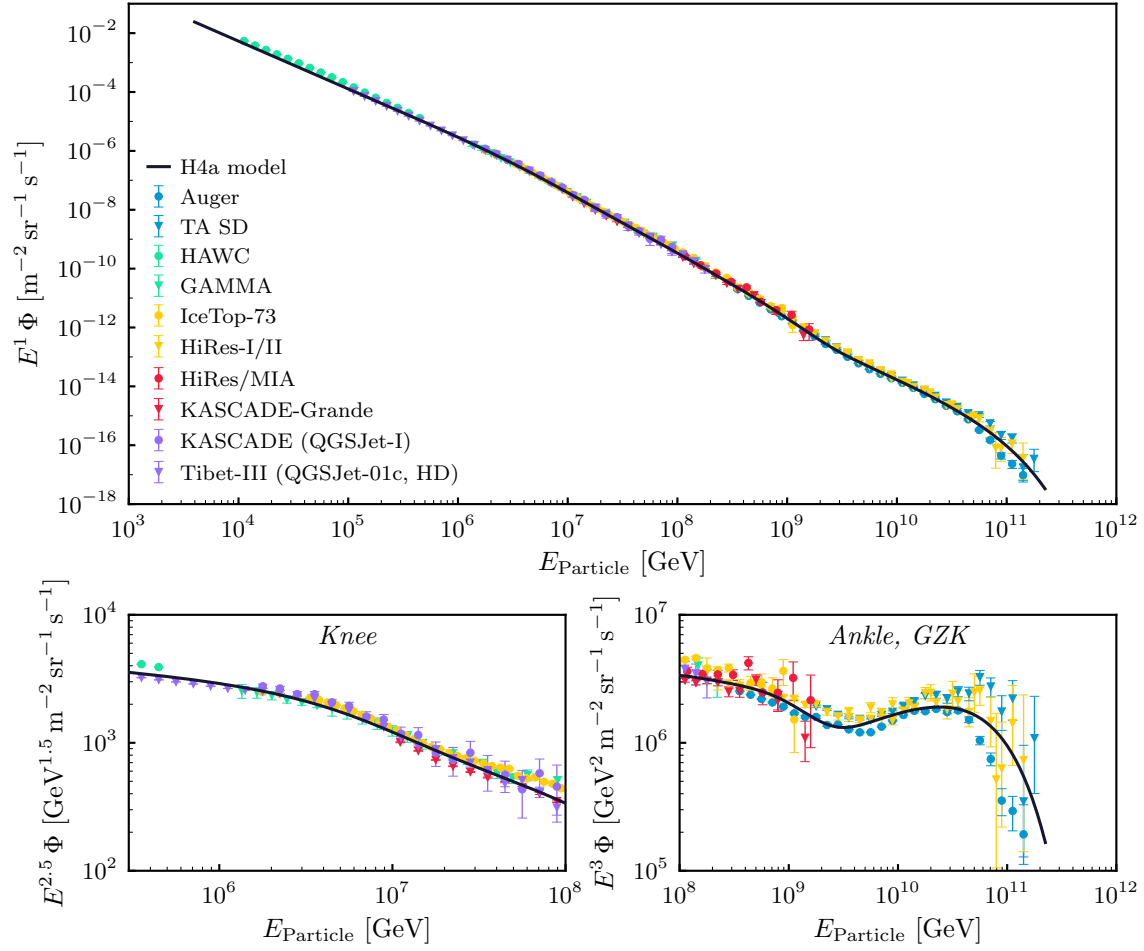


Fig. 1.1: Differential energy spectrum scaled with  $E$  (top) and detailed subplots of the so-called knee (scaled with  $E^{2.5}$ ) and ankle combined with the GZK cut-off (scaled with  $E^3$ ). Figure courtesy of Felix Henningsen with data from T. Gaisser, R. Engel, E. Resconi [2] and K. Krings.

$$\vec{F} = q \left( \vec{E} + \vec{v} \times \vec{B} \right) \quad (1.5)$$

For energies above  $10^{18}$  eV the Larmor radius is large enough that the particle could correlate with their galactic origin. But up to now there is no known galactic source capable of producing particles with energies beyond  $10^{19}$  eV. The deflection of cosmic ray particles in magnetic fields is a disadvantage as messenger in the search for their sources. Gamma rays and neutrinos as neutral particles do not have the same problem hence they cover a central role in the field of multi-messenger astronomy. At the very high energies in the cosmic ray spectrum is the flux cut-off at around  $5 \cdot 10^{19}$  eV. This cut-off was predicted by K. Greisen, V. Kuzmin and G. Zatsepin

in 1966 and is thus called the *GZK cut-off*. It emerges through the interaction of protons with photons of the cosmic microwave background (CMB) during propagation, if the incident proton energy is large enough to produce a  $\Delta^+$  resonance. This decays immediately via two possible channels.

$$p + \gamma_{cmb} \rightarrow \Delta^+ \rightarrow n + \pi^+ \quad (1.6)$$

$$\rightarrow p + \pi^0 \quad (1.7)$$

The positively charged pion decays into  $\mu^+\nu_\mu$  while the neutron is also unstable and decays via

$$n \rightarrow p + e^- + \bar{\nu}_e. \quad (1.8)$$

The second channel produces two photons via the subsequent decay of the neutral pion. Both possible interactions leave a less energetic proton behind and produce high energy neutrinos or photons, which highlights again the importance of neutrinos in the field of astroparticle physics [1, p. 215].

## 1.2 Cosmic accelerators

One of the main open questions regarding the origin of cosmic rays is the one related to the particle acceleration mechanisms. Cosmic accelerators are known within our galaxy and beyond.

**Galactic accelerators.** As aforementioned, the origin of the bulk of cosmic rays up to the knee is considered to result mostly from shock acceleration processes via supernova remnants (SNRs). This theory is additionally supported through the resulting power spectrum of shock acceleration processes,  $\sim E^{-2}$ , which can possibly be altered by propagation and energy losses to the observable  $\sim E^{-2.7}$  on Earth. At shock accelerations, kinetic energy of moving magnetized plasma is transferred to charged particles, subsequently increasing their energy. A single particle can be accelerated several times until it can escape the shock front [2, 5].

SNRs are the result of supernovae. During a supernova the stellar core will be compressed and a rise in the electron Fermi energy allows the generation of neutrons and neutrinos via

$$e^- + p \rightarrow n + \nu_e. \quad (1.9)$$

As neutrinos are only weakly interacting they can escape the concentrated matter. Through the cooling of the matter the density increases, which potentially causes nuclei in the center to become neutron-enriched. As the nuclei get unstable, they eventually break into their components and the abundantly created neutrons become degenerate. The emerging degeneracy pressure eventually aborts the collapse. Since this happens very sudden, the inward dragged

material will bounce against the degenerate core and initiate a shock wave, which creates the explosion. SNRs are then characterized by three phases. The first phase emerges directly after the explosion as the shell expands and sweeps up surrounding media. Here, charged particles can be accelerated by the shocks. Eventually, the surrounding interstellar medium performs too much pressure on the ejecta and forms a reverse shock wave, which is ultimately counteracted by the internal pressure, causing an adiabatic expansion. This is known as the Sedov-Taylor phase and marks the second stage. At the final state radiative losses dominate and cool down the SNRs, finally leading to the collapse.

Pulsar wind nebulae (PWN) are SNRs powered by a pulsar in their center [2, p. 271-276]. The latter is potentially also another possible accelerator. Pulsars, rotating neutron stars, are stellar remnants of massive stars and emerge from their gravitational collapse. The magnetic field of pulsars is extremely high and charged particles can be magnetically accelerated [1, p. 194]. Also, binary systems are possible cosmic accelerator candidates. Here, the accretion of matter by a compact object, for instance neutron stars, pulsars or black holes, from a donor companion, is releasing gravitational potential energy. Through the massive flow of ionized matter large electromagnetic fields are created, which bear the energy to accelerate cosmic particles to high energies [1, p. 199].

**Extragalactic accelerators.** As there are no known galactic sources for the acceleration of cosmic rays beyond an energy of  $10^{19}$  eV, extragalactic sources are considered to do so. The first possible candidates are active galactic nuclei (AGN), the most luminous sources in universe. A central supermassive black hole accretes matter and subsequently emits two relativistic particle jets perpendicular to the accretion disk, capable of accelerating particles to high and probably ultra-high energies. AGNs whose jet cone points towards Earth are called blazars [1, 6]. The origin of gamma ray bursts (GRB), the second candidate, is not yet fully understood. It is anticipated, that there must be a powerful driving force behind this phenomenon, such as hypernovae, the merger of two neutron stars or a neutron star with a black hole. In the so-called fireball model, the production of a new compact releases a lot of gravitational energy. Partly carried away by neutrinos and gravitational waves the remaining energy releases a high-temperature, opaque fireball which consists of photons, electrons, positrons and baryons supplied by a bipolar jet. This fireball expands relativistically through the internal radiation pressure. Hereby shocks develop and particles can be accelerated to high energies. As it further expands the fireballs optical depth declines and becomes increasingly transparent to radiation. This allows the photoproduction of pions and subsequently neutrinos. Photons are produced as the accelerated particles undergo deflection by electric or magnetic fields, releasing energy in the form of synchrotron radiation and bremsstrahlung. Also the inverse Compton effect plays an important role for their generation [6, 2, 7].

### 1.3 Cosmic messengers

Cosmic rays and their origin may also be studied by secondary particles which can reach Earth, unlike charged cosmic rays, unhampered. As was already outlined these secondary particles are e.g. gamma rays and neutrinos. However, no evidence for a direct correlation of both is given and the production mechanisms may differ. Photons are produced by electromagnetic interactions (synchrotron radiation and bremsstrahlung) and also by the decay of neutral pions. Whereas neutrinos are especially produced by decay processes of hadrons (e.g. pions, kaons). As a consequence, the primary cosmic ray particles must interact with some target to produce the secondaries. Two main possible scenarios arise through this confinement: a diffuse production of secondary particles via interaction of the cosmic ray within the interstellar medium and point-like sources, where accelerated particles interact in the direct vicinity of the source. The latter is known as *astrophysical beam dump* and allows the localization of high energy accelerators [7, p.332]. These cosmic sources accelerate protons and create hadrons through hadronuclear or photohadronic interactions, whereas the hadrons decay and subsequently generate neutrinos and, in the case of the neutral pion, photons [2, p.282].

$$p + p \rightarrow \pi^{\pm}, \pi^0, K^{\pm} + X \quad (1.10)$$

$$p + \gamma \rightarrow \Delta^+ \rightarrow n + \pi^+ \quad (1.11)$$

$$\rightarrow p + \pi^0 \quad (1.12)$$

Within this section, a brief introduction into these uncharged cosmic messengers shall be given, concluded by a concise overview of gravitational waves.

**Gamma rays.** As the cosmic rays traverse the universe they might produce photons along their path via various processes. One of them is the emission of photons through the deflection of cosmic ray particles by magnetic or electric fields within the universe, commonly known as synchrotron radiation (deflection in magnetic fields) and bremsstrahlung (electric fields). Another possible channel is the production of neutral pions  $\pi^0$ , which can for instance happen through the collision of cosmic rays with gas molecules.

$$p + p \rightarrow p + p + \pi^0 \quad (1.13)$$

As previously mentioned the  $\pi^0$  decays subsequently into two gammas. Another important production mechanism of high energy photons is the inverse Compton effect. It describes the process in which ultra-relativistic electrons scatter on photons and transfer some of their incident energy to the latter. Synchrotron radiation, bremsstrahlung, as well as the inverse Compton effect are leptonic processes, while the production via  $\pi^0$  is a hadronic process. When it comes to the detection of gamma rays one needs to consider that the universe, and to a larger extent also the atmosphere, is opaque to photons within certain wavelengths and therefore acts as a

filter. For example, PeV photons ( $10^{15}$  eV) underlie the conversion into an electron-positron pair by interaction with a CMB photon and the chance to reach Earth is small. Besides that, our atmosphere is not transparent for high energy gamma rays [1, p.11, 255, 282]. From this knowledge, two main detection techniques were established. The first is space-based and covers a broad energy region from a few MeV to a few GeV. However, as the  $\gamma$ -flux declines after a few hundreds of GeV the statistics in the small detector area, mainly limited by costs for space missions, is too low to perform adequate astronomy. Higher energy ranges can be measured by ground-based Imaging Air Cherenkov Telescopes (IACT) which are large arrays of telescopes that measure the light produced by the Cherenkov effect. As gamma rays interact electromagnetically within the atmosphere they can produce electrons and positrons with adequate energy to produce a Cherenkov light cone. This effect is as well quite important for the branch of neutrino astronomy and thus will be highlighted in section 2.1.1 as part of the neutrino detection principles [1, p.282].

**Neutrinos.** Neutrinos are solely weak interacting neutral leptonic particles, predicted by Wolfgang Pauli 1930 to solve the puzzling mystery of the continuous spectrum of the beta decay. In contrast to cosmic and gamma rays, they are much harder to detect due to their low cross section and the constraints set by the limitation to weak interactions. However, they thus provide also valuable insight into the high energy universe. Other than cosmic ray particles they are neutral, do therefore not underlie deflections by electric or magnetic fields and can traverse vast cosmic distances unimpeded. Hence, they allow for point source searches, which would be otherwise limited to cosmic rays with an energy of around  $10^{20}$  eV. Although the latter are constrained to a horizon of around 100 Mpc ( $1 \text{ pc} \approx 10^{16} \text{ m}$ ) as they are interacting with the CMB photons by the GZK effect. The gamma horizon, on the other hand, is limited by the interactions with the infrared and cosmic microwave background and comports itself to some ten millions parsecs for photon energies at  $10^{12}$  eV and decreases to around 100 kpc for photons with an energy of  $10^{15}$  eV. Neutrinos can travel unaffected through dense environments in the universe and are therefore valuable cosmic messengers in the field of high energy astrophysics [8, p.23]. On these grounds, the following chapters will focus in more detail on neutrino detection and its promising future given by the advent of new calibration tools and detectors.

**Gravitational waves.** Even though gravitational waves are unrelated to electromagnetic radiation and thus are not secondary cosmic ray messengers, like gamma rays and neutrinos, they are valuable contributors to multi-messaging astronomy and allow for a different view into the universe. Gravitational waves are tiny distortions of space-time caused by the most violent processes and very high energetic events in the universe, which involve the acceleration or deformation of huge masses. Prime examples are the collapse of two black holes, the merging of two neutron stars, or supernovae. Gravitational waves caused by these violent events start to propagate through the universe and disrupt, by squeezing or dragging, space-time. In this picture a certain similarity to water waves produced by throwing a stone into a pond becomes applicable. Gravitational waves have been predicted by Albert Einstein in his general theory of relativity in 1916. Although the first evidence for their existence could only be made several years later, in 1974, via the observation of a binary pulsar and the mathematical modeling of its merging speed through the loss of energy. However, those confirmations are only of mathematical nature and it took until September 14th, 2015, when the first physically measured distortion, caused by

two colliding black holes could be measured by the two Laser Interferometer Gravitational-Wave Observatory (LIGO) interferometers. This observation marks the first evidence of an inspiral and merger of binary black holes with stellar masses and flags also the beginning of gravitational wave astronomy. As messengers, they are very weakly interacting and therefore carry unimpeded information about their origin while electromagnetic radiation is highly affected by matter interactions (deflections and absorption, as highlighted in the previous sections). Gravitational waves thus allow a direct view into their universe and origin. Albeit, the signal that emerges once a gravitational wave passes through the Earth is vanishingly low. Hence, to detect gravitational waves, systematic errors need to be eliminated. For instance tiny quakes and other small vibrations can disturb the signal on Earth. The LIGO interferometers work with a laser beam that extends four kilometers into two directions. To exclude systematics the signal of the two similarly constructed LIGO observatories, stated in the USA in Livingston and Hanford, are compared with each other and only a coincidence signal is considered as a potential event [9, 3]. However, the localization of the source is only possible by triangulation of the signal performed by at least three detectors. Therefore a global network has been formed, consisting of the two LIGO interferometers, Virgo located in Italy, GEO600 in Germany, and KAGRA in Japan [10].

## 2 Neutrino detection

Neutrino detectors rely on the same principle, that is, the instrumentation of a vast volume in a transparent medium, such as ice or water, at great depths using a three-dimensional array of photon detectors. This approach follows a three-folded assault. Firstly, the large instrumented volume bears many target nucleons for neutrino interactions. Secondly, the great depth ensures the shielding from secondary particles mainly produced by cosmic rays. And lastly, the clear medium allows the propagation of Cherenkov photons produced by the neutrino induced secondaries. As Cherenkov photons can be measured by the photosensor array, direction and energy information are obtained. This can be used to search and investigate high energy astrophysical sources. This chapter will highlight some important aspects of neutrino physics to understand the underlying principles of high energy neutrino astronomy.

### 2.1 Neutrino interactions

Neutrinos belong to the group of leptons but unlike their counterparts, electrons, muons, and taus, they are not electromagnetically charged, and hence do not participate in electromagnetic interactions. Naturally, leptons are also not involved in strong interactions. On these grounds, neutrinos are exclusively weakly interacting [7, p.1]. Weak interactions are one of the four fundamental forces that are known as yet and are mediated by gauge bosons, more precisely the  $Z^0$  and the  $W^\pm$  bosons. As their large mass ( $m_{W^\pm} = 80.398 \pm 0.025$  GeV and  $m_Z = 91.188 \pm 0.002$  GeV [7, p.60]) limits the propagator associated with the exchange of the bosons, the weak interaction is ultimately suppressed [11]. The detection of high energy neutrinos grounds on their interaction with a nucleon  $N$  within or in the vicinity of the instrumented volume of the detector. This happens either via charged current (CC) or neutral current (NC) interactions. While the former is mediated by the  $W^\pm$  and the latter by  $Z^0$  bosons. Corresponding to their charged counterparts neutrinos occur in three flavors, which is indicated by  $l=(e, \mu, \tau)$ . Large volume detectors do not observe the interacting neutrino itself but charged particles generated by these processes. The main principle of neutrino detection lies then on the measurement of photons produced by these secondary charged particles via the Cherenkov effect, which will be explained hereafter.

$$\nu_l + N \rightarrow l + X \quad (\text{CC}) \quad (2.1)$$

$$\nu_l + N \rightarrow \nu_l + X \quad (\text{NC}) \quad (2.2)$$

#### 2.1.1 Cherenkov effect

Cherenkov radiation is caused by a charged particle with a velocity that exceeds the speed of light in a dielectric medium. That is, for a medium with refractive index  $n$

$$c_n = \frac{c}{n} \quad (2.3)$$

with  $c$  as the velocity of light in vacuum. The refractive index  $n$  is wavelength dependent. Charged particles traversing the detector medium at speed  $v$  will lose some of their energy along the path as they polarize surrounding molecules and orientate dipoles. As soon as the particle has passed, the dipoles will go back to their ground state and release energy in form of electromagnetic radiation. Once the charged particle is faster than the speed of light in the medium the electromagnetic waves will interfere to a characteristic light cone with angle  $\theta$ .

$$\cos \theta = \frac{c}{v \cdot n} \quad (2.4)$$

An estimate for the released number of Cherenkov photons  $N_C$  per unit distance traveled  $dx$  and unit wavelength interval  $d\lambda$  by a charged particle with charge  $q = z \cdot e$  can be obtained by the following equation [12, 1, p.324].

$$\frac{d^2 N_C}{dx d\lambda} = \frac{4\pi^2 q^2}{hc\lambda^2} \left( 1 - \frac{c^2}{n(\lambda)^2 v^2} \right) \quad (2.5)$$

Cherenkov photons are produced with a distinctive wavelength dependency of  $1/\lambda^2$  in a wavelength range between 300 and 600 nm [13]. Photons propagating from emission to the receiving sensor undergo absorption and scattering in the respective medium. These propagation effects have to be considered for simulation and reconstruction of events [13]. For this a detailed understanding of the optical properties is vital.

### 2.1.2 Neutrino oscillations

Neutrinos are produced and detected in a specific flavor state, which causes the production of distinctive secondaries with different signatures at interactions. Furthermore, neutrinos are capable of changing their flavor. This is called *neutrino oscillation*. As this affects the detection, neutrino oscillations in vacuum shall be briefly introduced in the following. Neutrinos do have flavor (electron, muon, tau) and mass eigenstates, in the case of a non-vanishing rest mass of the neutrino the eigenstates do not have to be identical, although both are connected with a certain matrix. In particular, this means that a certain flavor eigenstate is a quantum-mechanical superposition of mass eigenstates. Mathematically this can be described by a rotation matrix.

$$\begin{pmatrix} |\nu_e\rangle \\ |\nu_\mu\rangle \\ |\nu_\tau\rangle \end{pmatrix} = \begin{pmatrix} U_{e1} & U_{e2} & U_{e3} \\ U_{\mu1} & U_{\mu2} & U_{\mu3} \\ U_{\tau1} & U_{\tau2} & U_{\tau3} \end{pmatrix} \cdot \begin{pmatrix} |\nu_1\rangle \\ |\nu_2\rangle \\ |\nu_3\rangle \end{pmatrix} \quad (2.6)$$

For neutrino oscillations this matrix is known as the Pontecorvo-Maki-Nakagawa-Sakata (PMNS) matrix and is parameterized by the mixing angles  $\theta_{12}$ ,  $\theta_{23}$ ,  $\theta_{13}$  and a CP violating phase angle  $\delta_{CP}$ . Up to now several experiments put successful effort in the determination of those values [1, p.414]. Time development of a neutrino produced with a flavor  $\alpha$  at a source at  $t = 0$  follows

$$|\nu_j(x, t)\rangle = \sum_i U_{\alpha i} e^{-iE_i t} |\nu_i\rangle. \quad (2.7)$$

The relativistic energy can be approximated by

$$E_i = \sqrt{m_i^2 + p_i^2} \simeq p_i + \frac{m_i^2}{2p_i} \simeq E + \frac{m_i^2}{2E} \quad (2.8)$$

with  $E \approx p$  as neutrino energy and  $p \gg m_i$ . The three mass eigenstates  $m_i$  develop differently in time, which leads eventually to a different composition. Hence, the final flavor state can differ from the initial one. The oscillation probability can be described by

$$P(\alpha \rightarrow \beta) = |\langle \nu_\beta | \nu(x, t) \rangle|^2 = \delta_{\alpha\beta} - 4 \sum_{j>i} U_{\alpha i} U_{\alpha j} U_{\beta i} U_{\beta j} \sin^2\left(\frac{\Delta m_{ij}^2 L}{4E}\right) \quad (2.9)$$

using CP invariance [7, p.195]. Neutrino oscillations are only possible as long as one mass eigenstate differs from zero, thus neutrinos must have a non-vanishing rest mass, which is in conflict with the current standard model and indicates that it is not complete yet. Equation (2.9) bears two interesting features, firstly, it depends on the mass difference  $\Delta m_{ij}^2 = m_i^2 - m_j^2$ , which means that oscillation studies cannot yield an absolute mass limit. Besides that, two mass hierarchies are possible and several experiments pursue the goal of measuring the exact order. Secondly, the transition probability depends on the fraction of the distance to the origin  $L$  and the neutrino energy  $E$ , which is an important factor for the sensitivity of oscillation experiments. This affects also neutrinos of cosmic origin, due to the large distances they travel from their production site [7, p.195, 201]. Particularly this means that the three-flavor oscillation averages out over astrophysical distances. Once astrophysical neutrinos arrive at Earth they will have nearly equal fractions independent from the initial flavor received at the production. Neutrino detectors measure flavor-independently and show distinct signatures due to the different leptons released in the associated CC interactions.

### 2.1.3 Neutrino signatures

Neutrinos are produced and detected in a specific flavor [7, p.194]. Hence, as mentioned in the previous section, they show different signatures once they interact within the detector medium as the generated secondary particles have distinct follow-up processes. As astrophysical neutrinos are highly energetic they are capable of penetrating nucleons and trigger hadronic cascades caused by strong interactions. Out of this, two main event types can be classified in a neutrino detector: track and shower events. Neutral current events are flavor independent and will only produce hadronic cascades. Charged current events differ for the three flavor types and are more complex, as will be highlighted in the following.

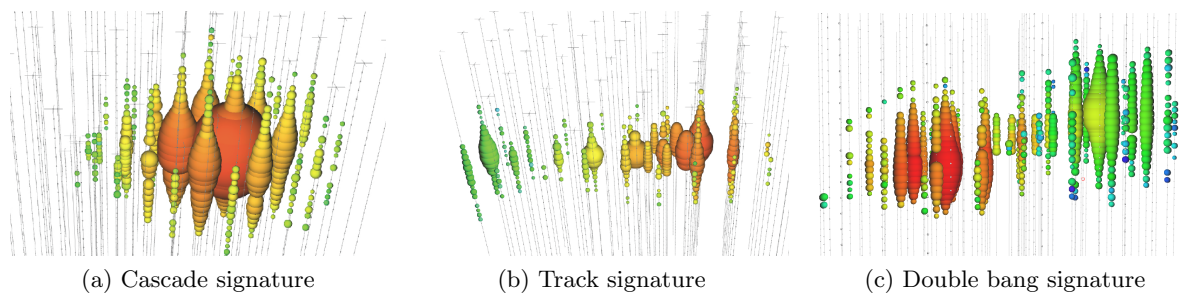


Fig. 2.1: Examples for event signatures for the different neutrino interactions. As the double bangs are very close to each other they are nearly indistinguishable from cascade events, higher detection probabilities can be achieved by closer instrumented volumes. Figures taken from [14].

**Shower-like events.** Neutral current events show the same signature for all neutrino flavors, namely a hadronic cascade. The main secondary particles generated in the cascade are pions, kaons, protons, and neutrons, whereby the fractions differ. As pions decay through the already discussed channels, also muons are produced, which can carry away a significant amount of the energy. The majority of the interaction energy is spent on the initiation of the hadronic cascade. Besides that, some of the initial interaction energy is carried away by the scattered neutrino. Hadronic showers show large event fluctuations as they naturally have a lot of free parameters for the production of secondary particles. Once high energy electron neutrinos interact in a charged current event they will generate a high energetic electron. As the electron propagates it will produce photons via bremsstrahlung. This leads to the production of an electromagnetic shower, whose length is correlated to the initial energy of the electron. For a 10 TeV electron this is a length of around 8 m in water [1, p. 329]. Which is, compared to the spacing distances of the optical modules in a detector, short. Out of this the signature follows a point-source structure as the Cherenkov photons distribute isotropically around the arguably short shower axis. As of yet, there is not much directional information obtainable by electromagnetic cascades.

**Track-like events.** A very distinguishable signal in a detector is caused by CC muon neutrino interactions. Thereby a muon will be released, which leaves a noticeable track signature in the detector. The path length of the muon depends on their initial energy and is in water around 5 km for a 10 TeV muon. Theoretically, the track can be used for point-source search. Practically, this is more difficult since the photons produced along the track underlie scattering and absorption processes within the detector medium. This must be taken into account for the reconstruction of the track, as it is done for instance by a likelihood function comparing the time and position of fired photosensors to the expectation of the Cherenkov signal. Hence, for an exact reconstruction, detailed knowledge of the optical properties in the detector medium is essential [1, p. 329].

**Double bang events.** High energy tau neutrino interactions bear the most significant signature. The produced tau neutrino can traverse the detector for a certain path length before it decays, which produces a second shower. Once both interactions occur within the detector

volume and the path length is sufficiently long, the signature is quite unique as it shows the initial shower, a track, and a second shower. Thus it is also referred to as double bang event [1, p. 330].

## 2.2 Neutrino sources

Apart the previously mentioned astrophysical processes as the origin of neutrinos, various other sources exist. The neutrino flux depicted in figure 2.2 gives an estimate of natural neutrino sources, which will be covered hereafter. Besides that, also artificial processes, for instance in reactors or accelerators, contribute to their production.

**Cosmic neutrino background.** At the beginning of the universe neutrinos remained in an equilibrium state with the primordial plasma. As the universe constantly cooled down they finally decoupled and traverse space, similar to the CMB. Until now they remain undetected. A possible observation would allow valuable insight into the early universe, in particular to the time of the neutrino decoupling (approximately one second after the big bang). Unfortunately, they can currently not be detected by large scale neutrino detectors due to their low energies. Nevertheless, an indirect observation is possible due to their significant effect on the early universe. Especially their relativistic propagation modified gravitational potentials and affected baryonic acoustic oscillations, which are observable by the CMB temperature power spectrum [15, 16].

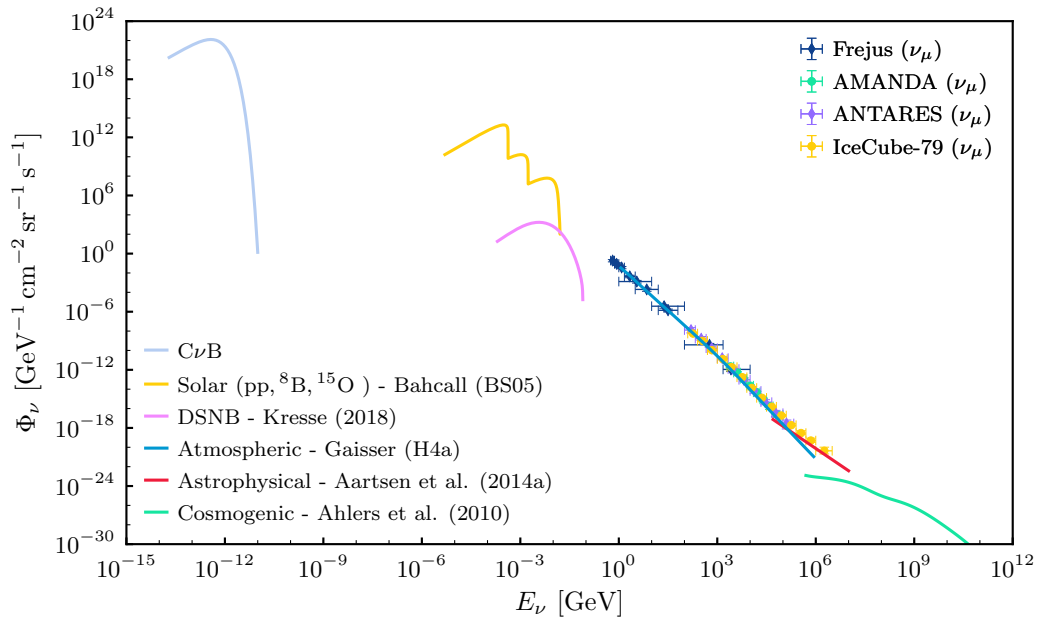


Fig. 2.2: Estimated neutrino flux originating from a variety of sources. For more information on the latter refer to the text. Especial gratitude goes to Felix Henningsen for providing this figure.

**Solar neutrinos.** Solar neutrinos represent one of the key contributors to neutrino physics research. Produced by the CNO cycle or the pp chain they are so weakly interacting that they can escape the sun almost unimpeded. This results ultimately in a large solar neutrino flux on Earth of around  $6 \cdot 10^{10} \text{ cm}^{-2}\text{s}^{-1}$ . Both reaction groups of the thermonuclear fusion within the sun result in the creation of electron neutrinos  $\nu_e$  with an energy of around 1 MeV. Some questions arose as the measured flux did not fit the expected solar neutrino flux in early underground experiments. This deviation would be later known as the solar neutrino problem and finally be solved by the discovery of the already discussed neutrino oscillations [17, 18].

**Supernova neutrinos.** Supernovae are dramatic phenomena in astrophysics and mark the termination of a star by a massive explosion. Besides a vast photon burst they are also accompanied by a fiercely luminous outburst of neutrinos, which can be used to study those phenomena. One of the most remarkable astrophysical events in the last century was the supernova SN1987A in the large Magellanic cloud on 23 February 1987, which provided scientists with valuable data [17, 7]. Diffuse supernova neutrinos are background radiation arising through distant supernovae isotropically distributed in the sky.

**Terrestrial neutrinos.** Beta decays in Earth, for instance in the decay chain of terrestrial uranium and thorium, produce so-called terrestrial neutrinos. Measurements of those neutrinos can help to gain insight into the composition of the Earth mantle.

**Atmospheric neutrinos.** Since cosmic rays interact with nuclei in the atmosphere secondary particles are produced. Among those are hadrons, in particular pions, and at higher energies also kaons. Leptonic decays of pions and kaons lead to the release of muons and neutrinos. While kaons can also decay semi-leptonic, producing electron neutrinos, or hadronic, generating more pions. Muons which decay before reaching ground produce subsequently electrons, electron neutrinos, and muon neutrinos. All neutrinos generated in these atmospheric cascades are called atmospheric neutrinos and pose one of the largest background sources within neutrino detectors. The ratio between produced flavor types, especially at lower energies, where muons tend to decay before reaching the ground, could not be verified with experimental data. This deviancy led eventually to the discovery of neutrino oscillations [17, p. 390].

$$\pi^+ \rightarrow \mu^+ + \nu_\mu \qquad \pi^- \rightarrow \mu^- + \bar{\nu}_\mu \qquad (2.10)$$

$$\hookrightarrow e^+ + \nu_e + \bar{\nu}_\mu \qquad \hookrightarrow e^- + \bar{\nu}_e + \nu_\mu \qquad (2.11)$$

**Cosmogenic neutrinos.** Ultra-high energy neutrinos are produced by the interaction of high energetic cosmic particles with CMB photons. This interaction generates a  $\Delta^+$  resonance, which decays via two possible channels.

$$p + \gamma_{cmb} \rightarrow \Delta^+ \rightarrow n + \pi^+ \qquad (2.12)$$

$$\rightarrow p + \pi^0 \qquad (2.13)$$

The decay of the generated neutron and charged pion opens production channels for ultra-high energy neutrinos. The other channel results in a less energetic proton and a neutral pion.

### 2.3 Neutrino detectors

Neutrino detectors follow, as mentioned at the beginning of this chapter, generally the same principle, which is the instrumentation of a large volume with photosensors to measure the Cherenkov light induced by neutrino interactions. By doing so, the detector is influenced by several environmental factors. In the first place, optical properties of the instrumented volume define and alter the path length of photons produced by the Cherenkov effect through absorption and scattering within the medium. In general, the intensity with initial value  $I_0$  as a function of the distance can be written with the law of Lambert-Beer

$$I(r) = \frac{I_0}{4\pi r^2} \cdot \exp \left[ -r \left( \frac{1}{l_{\text{absorption}}} + \frac{1}{l_{\text{scattering}}} \right) \right]. \quad (2.14)$$

The attenuation length is composed of the absorption and scattering length

$$l_{\text{att}} = \left( \frac{1}{l_{\text{absorption}}} + \frac{1}{l_{\text{scattering}}} \right)^{-1} \quad (2.15)$$

and denotes the distance after the intensity of the radiation decreases to  $1/e$  of the original value. The effective scattering length takes also the occurring scattering angle into account [19]. For neutrino detectors the influence of scattering and absorption length on the attenuation varies accordingly to the medium. In water the absorption length is the prime factor, while in ice scattering effects are predominant. The efficiencies of both detector types depend highly on the instrumented volume. High energy neutrino events can extend over several kilometers but efficient energy measurements are only possible if the majority of the event remains within the extension of the instrumented volume. Also, the overall chance for neutrino interactions scales with the detector volume. Low energy events produce fewer photons and therefore the spacing of the optical modules becomes more relevant. For a denser packed volume, the detection of low-energy neutrino events is easier, as the absorption length can be mitigated. However, for an ideal medium with a very long attenuation length, the spacing could be further apart. Naturally, caused by their low cross-section, neutrino events remain low in statistics. As a consequence of this, background events must be well known to be distinguishable from neutrino-induced interactions. Dominant background in water can be the presence of bioluminescent organisms and potassium decay. Ice, on the other hand, is highly affected by scattering influenced by environmental parameters during the ice sheet formation, such as the atmospheric composition (gases, volcanic ashes, dust).

One of the largest backgrounds in a neutrino telescope are the muons and neutrinos produced in the atmosphere. The flux of atmospheric muons is many orders of magnitude higher than the flux of astrophysical neutrinos and poses the bulk of reconstructed events in a detector, as they can traverse some kilometers in water and ice. In order to reduce the background radiation neutrino detectors are located several kilometers below ground. Like this, a large fraction of incoming atmospheric muons is shielded beforehand. Furthermore, a restriction to up-going events would circumvent the problems induced by atmospheric muons, as the Earth can be used

as shield. Neutrino detectors are the only working telescopes capable of looking downward. On the downside of this, also very high-energetic neutrinos will be shielded by Earth as the cross-section of neutrinos increases with their energy. It is possible to use a dedicated volume within the detector to self-veto atmospheric neutrinos by detecting muons, which typically accompany them and are spatially and temporally correlated. Both factors together, the opaqueness of the Earth and the atmospheric neutrino veto, limit the sensitivity to astrophysical high energy neutrinos to 20-30 degrees around the horizon of the telescope. The remaining part of this chapter will briefly introduce existing detectors and their basic structure.

**IceCube.** IceCube is located at the Amundsen-Scott south pole station and exploits glacial ice as detector medium, with an overall instrumented volume of about one cubic kilometer. The in-ice array hosts in total 5160 digital optical modules (DOMs) deployed in a depth between 1450 and 2450 m below the surface on 86 strings. To install these, a special drilling technique, using hot water, was applied. The DOMs of IceCube are working with a single 10" photo multiplier tube (PMT), which is facing downward while the readout and supply electronics are stored in the upper hemisphere. DeepCore is a sub-array within IceCube specifically designed for low energy detection. The DeepCore array consists of 8 strings with respectively 60 narrower spaced DOMs. It is optimized for neutrino energies around 100 GeV and aims for the investigation of atmospheric neutrino oscillations, neutrinos from WIMP dark matter annihilation, and galactic supernovae. The detection units are completed by IceTop, which consists of 162 ice-filled tanks instrumented with DOMs. The main goal of IceTop is to veto down-going muons but additionally, studies on high- $p_T$  muons, PeV gamma rays, and radiation effects of solar flares are performed. The telescope is completed by the IceCube Laboratory which hosts server rooms, data acquisition, and online filtering computers [20].

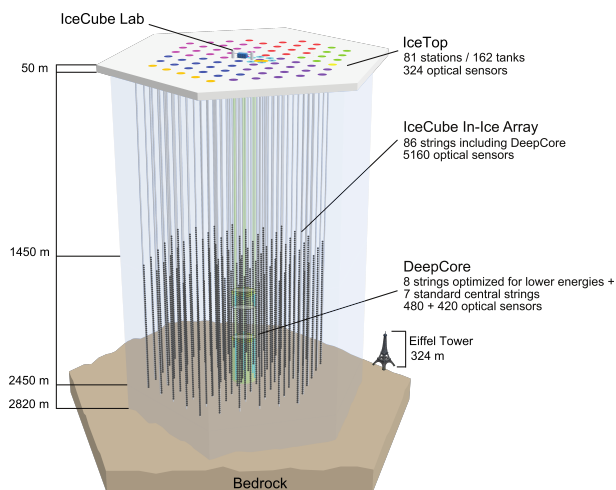


Fig. 2.3: Sideview of IceCube with the components mentioned in the text. Picture taken from [20].

**KM3NeT.** KM3NeT is being constructed at three different locations in the Mediterranean Sea and poses a network of neutrino telescopes. The exact sites are offshore Toulon, France, Capo Passero at Sicily, Italy, and Pylos, Greece respectively. With its design and locations in the Mediterranean Sea, the detector network is optimized for the search of Galactic neutrino sources. Starting points for the design and the beginning of the collaboration were the predecessor experiments NEMO and ANTARES [21, 18]. The modules of KM3NeT are composed of 31 3-inch PMTs, while 18 modules are lined up on two flexible Dyneema ropes. This structure is called detection unit. The final configuration of KM3NeT foresees six building blocks, composed of 115 detection units with varying distances at the deployment sites [22]. One building block covers an instrumented volume of about half a  $\text{km}^3$ , thus the final configuration will instrument

a total volume of around  $3 \text{ km}^3$ . Noteworthy is the deployment technique of the detection units, as KM3NeT is following a bottom-up deployment strategy, with a detection unit enclosed in an aluminum launching vehicle, called LOM. This will be deployed at the seafloor and unfolds the detection unit after an acoustic or ROV-triggered mechanical release. The launching vehicle floats and will be recovered after successful deployment [21].

**Baikal-GVD.** The Gigaton Volume Detector (GVD) is another neutrino telescope currently under construction in the northern hemisphere. It is situated at Lake Baikal, the worlds largest freshwater reservoir. Baikal-GVD follows a clustered structure, whereas one cluster comprises 288 optical modules (OMs) on 8 vertical strings with an inter-string spacing of 60 m and a distance between clusters of around 300 m. As of today, three clusters are deployed, which makes it currently the largest neutrino telescope in the northern hemisphere. The three clusters are depicted in figure 2.4. After completion of the next two stages, Baikal-GVD will instrument an effective volume of around  $1.5 \text{ km}^3$ . The ice cover that

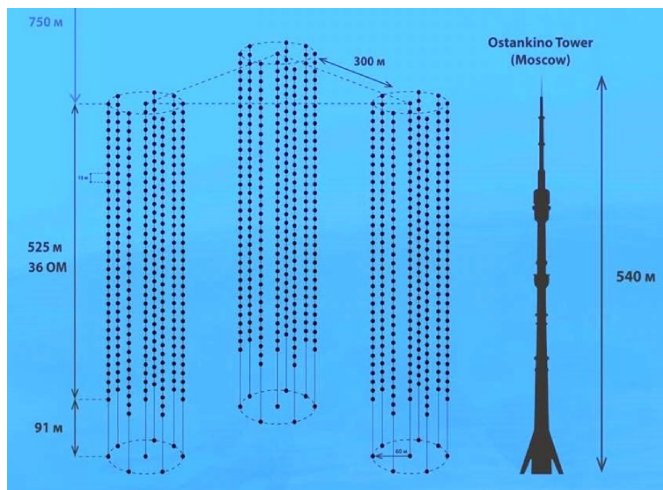


Fig. 2.4: The three currently existing clusters of Baikal-GVD in an artistic depiction taken from [23].

forms during the winter months allows the deployment of strings directly from the top of the lake. Similar to IceCube the OMs of Baikal-GVD host a 10-inch PMT. A global trigger is used for the timing calibration between the different OMs within a single cluster [24].

## 2.4 Prospects of neutrino astronomy

The observation of a high energy muon neutrino by IceCube on the 22nd September 2017 has led to the possible identification of the blazar TXS 0506+056 as potential high energy neutrino source [25]. Follow-up investigations by various other facilities (e.g. MAGIC, VERITAS, Fermi-LAT) have been triggered by this observation. The subsequent detection of gamma rays with energies larger than 100 GeV exposed the probable location of the blazar and its flaring state at the time of the neutrino detection. TXS 0506+056 best-fitting coordinates are right ascension (RA)  $77.43_{-0.65}^{+0.95}$  and declination (Dec)  $+5.72_{-0.30}^{+0.50}$  at  $z=0.3365$ . Spacial and temporal coincidence of the blazar flare and the high energy neutrino is estimated to be at a  $3-3.5 \sigma$  level [26, 25]. The detection of the first cosmic neutrino source pushes neutrino and multi-messenger astronomy additionally. Further exploration of the high energy neutrino universe is being pursued by the on-going construction of large scale neutrino telescopes, as Baikal-GVD and KM3NeT, as well as new installations. These become reality by the planned IceCube Upgrade (ICU) and the vision of a new complementary neutrino telescope in the northern hemisphere, the Pacific

Ocean Neutrino Experiment (P-ONE). Both aim to improve neutrino astronomy and give rise to the development of P-ONE pathfinder missions and a novel iteration of the Precision Optical Calibration Module (POCAM).

### 2.4.1 IceCube Upgrade

The IceCube Upgrade (ICU) is planned as precursor installation for a next generation neutrino telescope in the glacial ice, IceCube-Gen2. Besides its research and development aspects for the latter, the ICU aims also for its own science goals and is mainly constructed as low-energy extension  $O(1 \sim 10 \text{ GeV})$  of IceCube. The ICU array will therefore densely instrument a depth between 2150 m and 2425 m, referred to as physics region, as it is the depth with clearest glacial ice and a low atmospheric muon background. The densely instrumented volume allows measurements on tau neutrino appearances and thus further studies on neutrino oscillations are enabled as atmospheric neutrinos bear mostly electron or muon flavor. The IceCube Upgrade will consist of seven new strings with approximately 700 modules. As the optical properties of the ice pose one of the major uncertainties within the analysis of neutrino detection another main goal of the ICU is the reduction of systematical errors. For this, newly developed calibration devices and optical sensors will be deployed. Among the optical modules are the multi-PMT digital optical module (mDOM), the dual optical sensors in an ellipsoid glass for Gen2 (D-Egg), and a refined version of the former IceCube optical module. The new optical modules aim to improve the photon detection efficiency. Calibration devices are manifold and range from new optical to acoustic emitters [28].

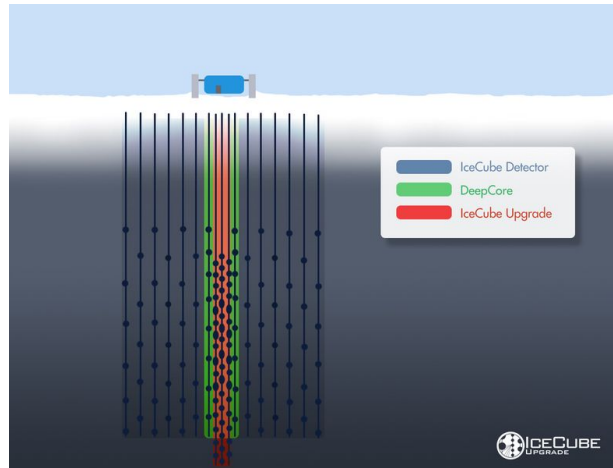


Fig. 2.5: Conceptual illustration of the planned IceCube Upgrade, integrated in the already existing in-ice arrays. It is picturing the increased density of the ICU strings as well as the modules. Figure taken from [27].

### 2.4.2 Pacific Ocean Neutrino Experiment

The opportunity given by an existing deep-sea infrastructure near the coast of British Columbia and the possible improvements in sky coverage by a third neutrino telescope in the northern hemisphere motivate P-ONE. The deep-sea infrastructure is hosted by Ocean Networks Canada (ONC) and comprises two large cabled ocean observatories, namely the North East Pacific Time-series Underwater Networked Experiments (NEPTUNE) and the Victoria Experimental Network Under the Sea (VENUS). NEPTUNE distributes five nodes over the Juan de

Fuca tectonic plate, which serve as connection points for various kinds of experiments. One of those nodes, located at the Cascadia Basin, is selected to host P-ONE. To perform first site characterization measurements the Strings for Absorption Length in Water (STRAW) collaboration was formed and pathfinder missions initiated. The first of which had the main goal to perform on-site measurements of the optical properties, in particular the attenuation length, and also first background characterization measurements. The latter is caused primarily by the presence of bioluminescence and potassium decay. The first STRAW detector has been deployed in summer 2018 and takes data continuously since then. Motivated by the results of STRAW, a follow-up mooring line, STRAW-b, as second pathfinder is currently under development. As a single mooring line with a total length of approximately 450 meters, it pursues a three-fold strategy to further characterize the deployment region. The primary tasks are the verification of the attenuation length measurements of STRAW, an in-depth study of the bioluminescence background and the development of suitable deployment strategies for future P-ONE mooring lines. To achieve this goal, six specialized modules will be deployed among which are two laser instruments, two PMT-based and one CCD-based spectrometer and a muon tracker operating with plastic scintillators. Both pathfinders and an outlook towards the design of P-ONE will be covered in chapter 4 and 5 of this thesis.

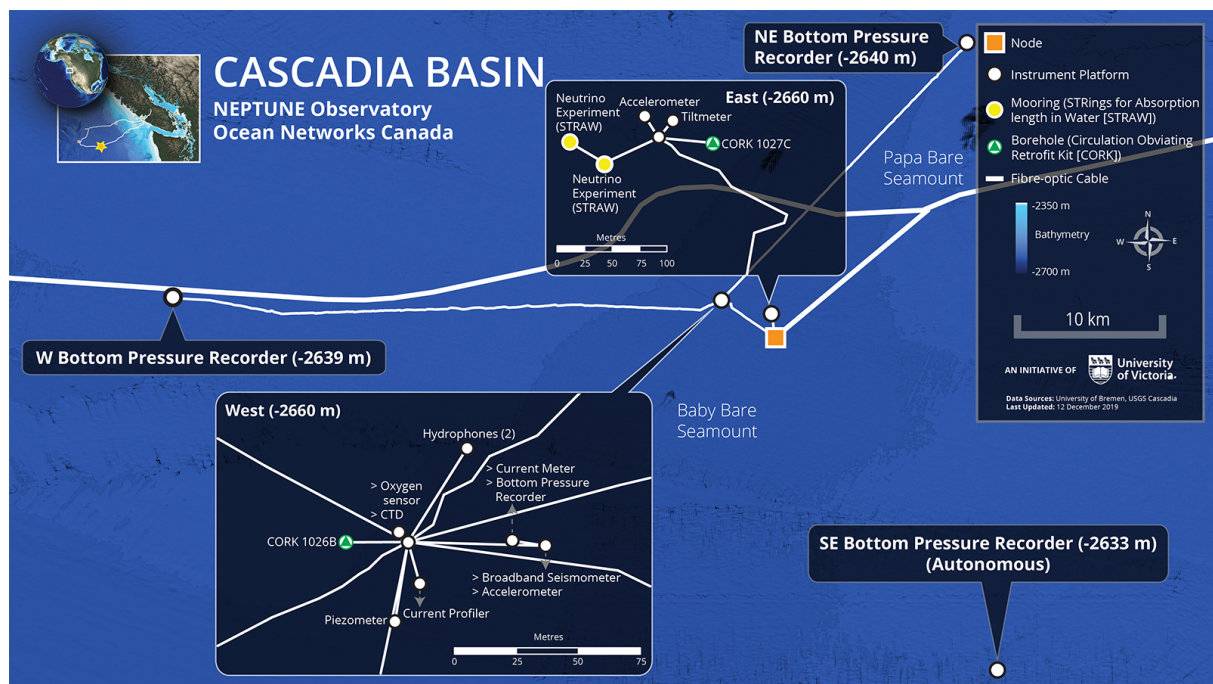


Fig. 2.6: Overview of the Cascadia Basin as part of the NEPTUNE observatory, which is the selected site for P-ONE and hosts currently the pathfinder missions. Picture courtesy of Ocean Networks Canada [29].



## 3 Precision Optical Calibration Module

### 3.1 Motivation

As already outlined in chapter 2, the reconstruction of neutrino induced events relies heavily on the precise knowledge of the optical properties of the detection medium, as they are typically influencing intensities and arrival times of secondary produced photons. Also, detector responses and other systematics, for instance the detector geometry, especially for water-based telescopes, play a major role. Accurate knowledge of these parameters is mandatory for a precise event reconstruction [13]. Grounding on this, the development of a Precision Optical Calibration Module, in short POCAM, was initiated in late 2014. The idea is based on the emission of an in-situ monitored artificial nano-second light pulse to calibrate the surrounding optical modules. First prototypes have been successfully tested in GVD-Baikal and in the scope of the first P-ONE pathfinder mission, STRAW. Now, a novel iteration is in development for the IceCube Upgrade and the first P-ONE mooring lines. The concept of using artificial light sources within the detector volume is not new, in fact, every larger telescope is utilizing a similar technique to access their optical parameters. Nonetheless the POCAM bears due to its absolute intensity calibration, large dynamic range, short nanosecond pulses, and the ability of self-calibration, the potential to function as standard calibration light source for neutrino telescopes. This chapter focuses on the properties of the third POCAM generation, concentrating on new analog circuitry aspects as developed in the scope of this master thesis. Before doing so, the state of the art of calibration in IceCube and other neutrino detectors shall be provided.

IceCube utilizes a flasher board within their DOMs featuring a total of six light emitting diode (LED) pairs circularly mounted around the printed circuit board (PCB) [20]. Every  $60^\circ$  in azimuth the two LEDs are aligned in such a way that, after refraction by the DOM glass and into the ice, one LED emits horizontally while the other at an angle of  $48^\circ$  upward, which is close to the Cherenkov angle in ice. The LEDs can be flashed with a frequency of 610 Hz and an intensity between  $10^6$ - $10^{10}$  photons, with a wavelength centered around 399 nm. By use of the obtained data sets by the LED flasher boards, an estimation of the ice parameters can be performed. The latter are defined by six global parameters, depth-dependent temperature, and as prime factor the scattering and absorption lengths. The glacial ice is averaged over layers with 10 m thickness. The light propagation from the LED flasher boards is simulated by a photon propagator, using varying ice parameters. A global fit for all parameters to the real flasher data could be obtained by a subsequent maximum likelihood analysis, resulting in a table of estimates for depth-dependent scattering and absorption lengths. Within the physics region, the deployment site of the ICU strings, the values range from 20-80 m for effective scattering and 80-260 m for the absorption length [13]. By exploiting the same data set also the observed optical anisotropy of the south pole ice is being investigated. The anisotropy effect is presently characterized by a diagonal matrix, which modifies the scattering behavior [30]. Where the depth-dependency of the anisotropy and comparatively uncertain emission profiles and alignments of the LEDs affect the results. The self-calibration ability and the isotropic emission pattern of the POCAM promises potential improvements, as no initial light emission profile has to be assumed. Detection characteristics, by means of individual relative DOM

efficiencies, are currently approached by measuring cosmic ray induced minimum-ionizing muon events, which offer a reasonably known light yield. As the POCAM provides an isotropic light emission profile, direct measurements of DOM efficiencies can be performed. Hereby potential aging effects of the hardware, which possibly alter efficiency and linearity behavior can be tackled. In addition to that, light signatures can be mimicked by the POCAM, especially cascades or double bang scenarios by timing the light flashes, which allows to access the cascade energy reconstruction by the known total POCAM photon output [31]. One of the major uncertainties within IceCube is the refrozen water in the drill holes, commonly referred to as hole ice. It emerged through the refreezing process in the drill hole and is generally described by a modification of the angular acceptance curve of a DOM. Solely in the case of low-energy reconstructions it is modeled as an ice column with aberrant optical properties compared to the bulk ice [32]. By the aid of POCAMs deployed in different depths, an unimpaired measurement of the in-situ angular acceptance of the DOMs can be performed [31].

The ANTARES collaboration, one of the predecessors of KM3NeT [21], performed site studies with a dedicated mooring line and two optical modules, one light emitter and a PMT-based receiver module. Absorption and scattering lengths were measured with blue (473 nm) and UV (375 nm) light, resulting in values of around 60 m (blue) respectively 25 m (UV) for the absorption length, and 260 m (blue) and 120 m (UV) for the scattering length [19]. This illustrates an inverted distribution to the aforementioned optical properties of glacial ice. Complementary measurements were performed at the other detector sites by the NESTOR and NEMO collaborations using similar setups [33]. Time calibration within a mooring line in KM3NeT utilizes a nanosecond pulser-based LED driver, named Nanobeacon, hosted inside the DOMs while pointing towards the upper modules [34]. Baikal-GVD evaluated the optical properties of the fresh water by the assistance of lasers. In addition to that, a verification of the obtained results could be done by a first prototype of the POCAM [35, 36]. In the scope of P-ONE, site studies were performed by utilizing three POCAMs in the first pathfinder project STRAW. Calibration, during the lifetime of the future detector, will be handled by several calibration modules on the base of the POCAM presented in this thesis. Two of them will be hosted on each single mooring line to calibrate the optical modules of P-ONE.

### 3.2 POCAM design

The POCAM features self-monitored isotropic light pulses with a high dynamic range to serve as a standard calibration device for large-volume photosensor arrays as utilized in high and low energy neutrino detectors. Generally, it consists of light flasher circuits, a diffuser to isotropize the light output, photosensors for self-monitoring, and electronics for readout and data acquisition (DAQ). The development of the POCAM was initiated in late 2014 and its design went through a number of iterations since then. Important milestones have been the deployment in Lake Baikal as part of the Gigaton Volume Detector (GVD) and, motivated by its success, the development of the STRAW mooring lines, which utilize in total three of the second generation POCAMs [37, 38].

### 3.2.1 Titanium housing

To withstand harsh environments like the deep-sea and glacial ice, especially the emerging pressures in water or during refreezing processes, as well as temperature extremes or variations, and corrosion, all the components of the POCAM are encapsulated in a titanium pressure housing. A cut-view of the overall design is given in figure 3.1. The titanium pressure housing was developed in close collaboration with the marine housing specialist Nautilus Marine Service GmbH. It is qualified for a pressure resistance up to 680 bar, tested for temperatures as low as  $-55^{\circ}\text{C}$ , and has been additionally vibration- and shock tested in the scope of STRAW according to the ISO standard 13628-6. The cylindrical design allows a nearly isotropic light emission in the far-field and provides enough space for internal electronics. Especially the design of the hemispheres is important for the overall emission profile of the module. A hemisphere consists of an optical-enhanced borosilicate glass attached via deep-sea rated epoxy resin to the titanium flange. The latter are mounted to the titanium cylinder while two sealing O-rings are closing the module hermetically.

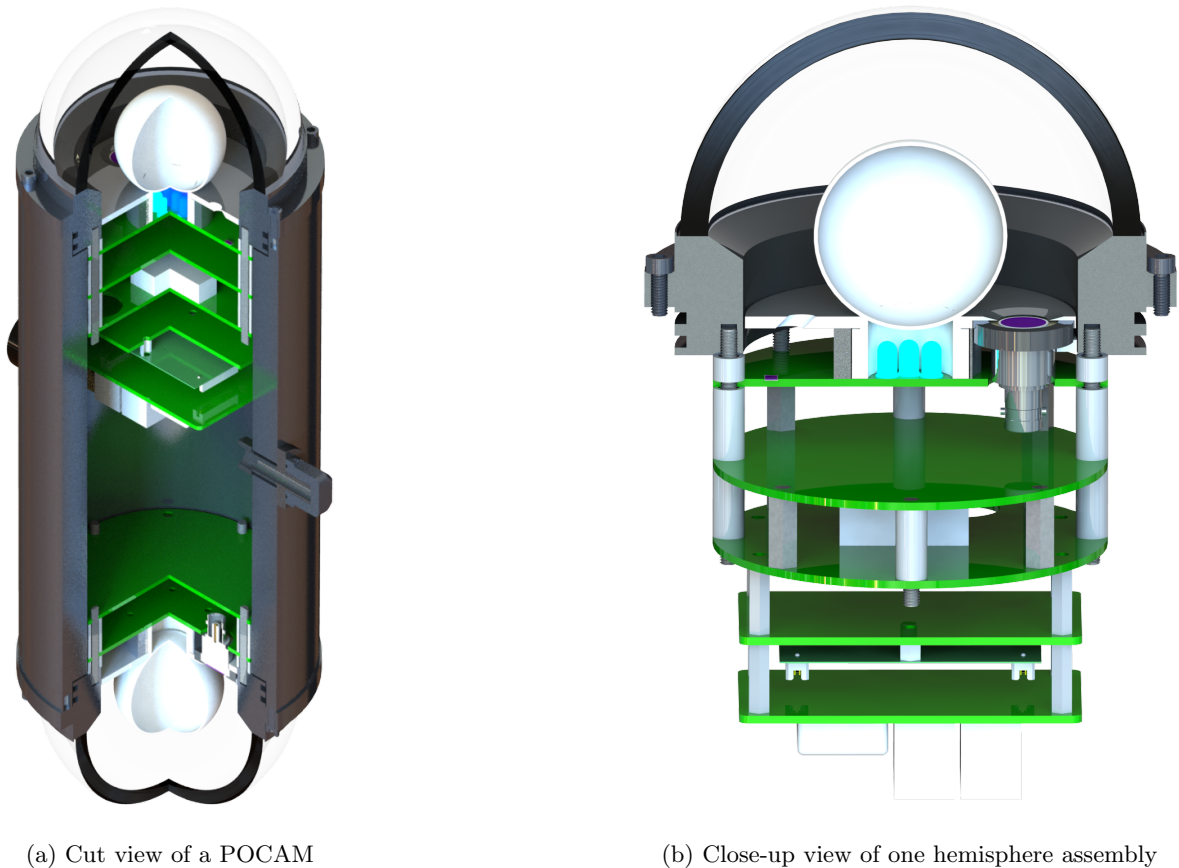


Fig. 3.1: Cut view through a complete POCAM in (a) and close-up view of one hemisphere assembly in (b). For details on the sub-components refer to the text.

The aforementioned environmental resistances have been tested with appropriate internal and external tests. The pressure rating was performed at a special test facility at the housing manufacturer Nautilus. Thereby the module has been enclosed in a pressurized tank and was repeatedly cycled to a pressure of 680 bar. Temperature tests have been performed within our institute. First temperature resistance measurements could be carried out with a fridge kindly provided by the chair of biophysics (E22). Here, the module was cooled down for various time intervals to a total temperature of  $-80^{\circ}\text{C}$  and then exposed to room temperature to initiate an immediate unfreezing process. After every cycle, the module and especially the flanges have been checked for visible damages. The titanium housing remained intact and also the connection of the borosilicate glass to the flange via the deep-sea epoxy resin stayed unimpaired. Additionally, a monitored temperature test has been performed in a specialized freezer where internal pressure, temperature, and humidity have been observed for a total testing period of five weeks and were found to remain stable. In the scope of STRAW, vibration and shock tests according to the ISO 13628-6 standard have been successfully performed at test facilities of the German company IABG Industrieanlagen-Betriebsgesellschaft mbH.

### 3.2.2 Internal construction

The internal design of the POCAM follows a modular approach. Both hemispheres host a combined system of light diffusing PTFE-sphere as well as analog and digital front-end boards. The latter contain the necessary flasher circuits, photosensors for self-monitoring as well as the required power supplies and control by a field programmable gate array (FPGA). As these hemisphere-submodules are constructed as one single stack and mounted to the flange via four threaded bars it is ensured that every submodule can be exchanged. Printed arrows on the circuit boards as well as grooves on the PTFE-sphere mounting guarantee a defined orientation that ensures the validity of the emission profile of the specific assembly. A black coated aperture disk suppresses stray light and ensures that mainly the emission of light by the diffuser is driving the emitted light profile. Besides that, the aperture disk provides fixed solid angles for the two integrated photosensors. It is composed by two half-disks and a mounting ring, which holds the PTFE-sphere. Stainless steel (X5CrNi18-10) has been chosen as material since it provides a similar thermal expansion coefficient to titanium. In terms of thermal expansion also the difference between the PTFE-sphere ( $143.3 \cdot 10^{-6} \text{K}^{-1}$ ) and stainless



Fig. 3.2: Picture of the PTFE-sphere and the aperture disk mounting ring. To account for different thermal expansion coefficients the mounting ring is designed smaller and the sphere is fitted in after cooling it down to  $-50^{\circ}\text{C}$ .

steel ( $16.9 \cdot 10^{-6} \text{ K}^{-1}$ ) had to be considered [39]. To alleviate the risk of loose parts at temperatures reached during the deployment at the South Pole, the aperture ring has been designed smaller than the PTFE neck. The latter can then be thermally fitted at  $-50^\circ \text{ C}$ . As this POCAM generation is specifically designed for the IceCube Upgrade, it hosts three IceCube-specific communication boards to interface with the existing IceCube network. These boards are the IceCube communications module (ICM), a specific power supply, and a PCB with a micro-controller unit (MCU) as core. Their functionality will be covered in section 3.7. This communication stack is provided by the IceCube collaboration and is called mini mainboard (Mini-MB). Each POCAM will host one Mini-MB module which will be mounted on one hemisphere assembly to the so-called distribution PCB. The latter is cabled separately to both hemispheres. Figure 3.3 shows one of the hemisphere-submodules and the IceCube communication stack.

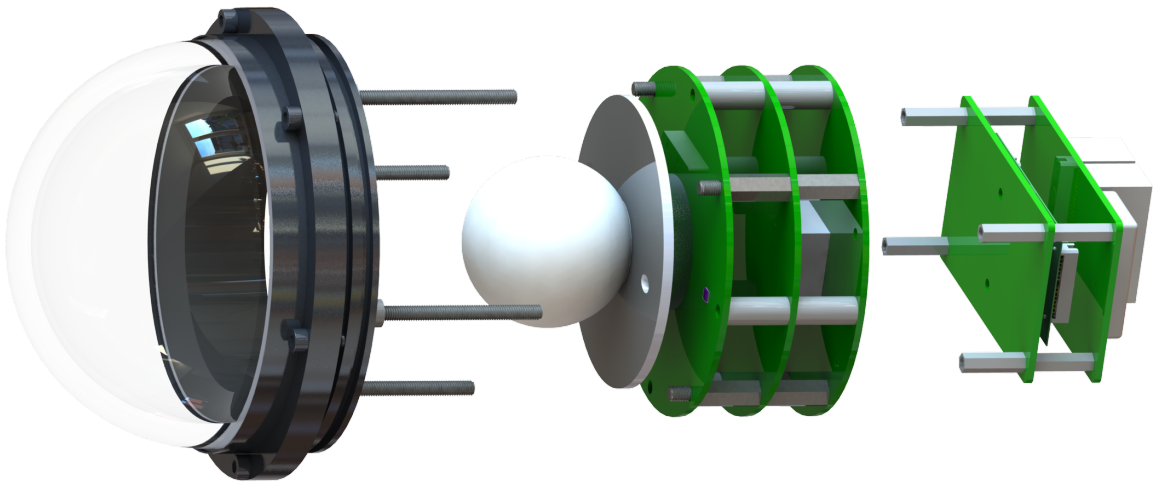


Fig. 3.3: Internal construction of one hemisphere. The PCB stack, comprised of the analog, digital, and distribution board, is mounted together via distance bolts. The PTFE-sphere is fitted in the aperture mounting ring, both parts are afterward screwed to the analog board and aperture disk. The overall stack is connected to the titanium flange via four threaded bars. The Mini-MB of the ICU is mounted to the distribution board.

### 3.3 Isotropy

One crucial aspect of the POCAM is the light emission profile. The goal is here to achieve a nearly isotropic profile. This allows the calibration to work independently from the orientation of the POCAM within the detector volume. Additionally, the POCAM is also self-monitored by two photosensors, which rely on the isotropic light emission. The main principle to achieve isotropy is based on the use of a two-part integrating sphere made from PTFE (teflon) and its intrinsic Lambertian reflective properties. The initial light pulse from the emitter circuits is pre-diffused by a PTFE plug before it is integrated in the sphere. Both parts can be seen in figure

3.2. The general concept has already been proven reliable in the first two POCAM iterations but was revised for this third generation. On that account, we examined slightly different plug and sphere geometries as well as new production techniques for the underlying PTFE. While the former did not show any significant improvements and were quickly disregarded, the latter, in the form of so-called optical PTFE, could enhance the isotropic light emission significantly. Optical PTFE is produced by an isostatic molding technique for teflon granule, which achieves ultimately a better compression compared to uniaxial molding. This improves the surface texture drastically [40]. For the emission profile measurements a dedicated characterization setup was used, which will be covered in detail in section 3.8. Apart from that, a GEANT4 simulation framework setup of the POCAM, created by Felix Henningsen, was used to investigate further optimizations. The simulation reproduces the measured emission profile to within 1%. The difference between normal and optical teflon is shown in figure 3.4 and illustrates the significant improvements achievable by the advanced production technique.

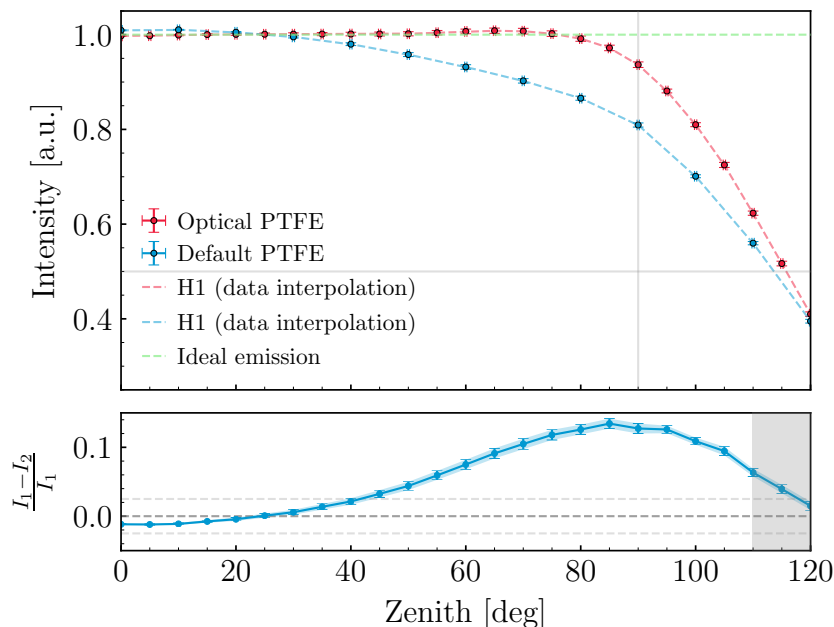


Fig. 3.4: Comparison of optical to normal PTFE, normalized to the intensity between  $0^\circ$  and  $45^\circ$ . Optical teflon shows a nearly constant emission profile until a zenith angle of  $70^\circ$ , normal PTFE still depends on the LED intrinsic cosine emission profile. At  $90^\circ$  the flange waistband is disturbing the emission. The lower plot shows the deviation between both materials. Figure courtesy of Felix Henningsen.

Besides the enhancements made by the material of choice also the internal geometry has been revised. In earlier generations of the POCAM, the center of the teflon sphere was aligned with the glass hemisphere which resulted in a higher dependency on the flange waistband. Especially as the glass sphere is connected to the flange via epoxy it is influencing noticeably the emission profile. Although improvements in the production technique of the flanges achieved a precise

and small waistband edge a small deviation remained observable. To mitigate this an offset of the integrating sphere with regard to the flange equator was simulated. As the results were promising measurements with a full POCAM hemisphere and an offset of 4 mm followed. The simulated data and respective measurements are shown in figure 3.5. Here, the total emission profile is obtained by combining the results of two hemispheres in the far-field. This shows that for a higher offset the effects of the waistband and the cylinder can be mitigated. For the final configuration of the POCAM a total offset of 5.5 mm is envisaged, based on simulation results in ice.

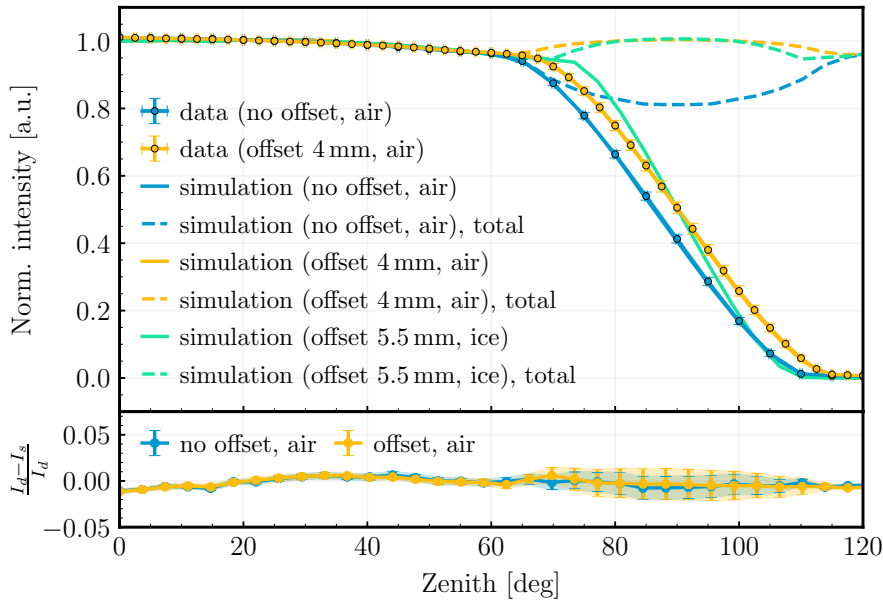


Fig. 3.5: Simulated and measured emission profiles for different offsets between the center of the diffusing sphere and the glass hemisphere. In general, the higher the offset the less severe is the impact of the flange waistband. For the final POCAM configuration an offset of 5.5 mm is planned. The lower plot shows the deviation of the simulated results to the measured data set. Figure kindly provided by Felix Henningsen.

### 3.4 Flasher circuits

The pulse drivers, located on the analog board, are utilized to generate the nanosecond light flashes. Therefore, mostly analog circuitry is employed. The former generations of the POCAM had solely one type of analog flasher, namely the Kapustinsky pulse driver [41], accompanied by a FPGA-based pulser. In the scope of this thesis new pulse drivers have been investigated for the third POCAM iteration. The goal of this was to exploit ultimately a wider dynamic intensity range. Several potential light pulsers were tested, among which many have been disregarded, simply due to underperformance or for non-reliability. Especially the latter posed to be difficult for some devices as they could not handle for instance mild overvoltage peaks or needed to be

individually fine tuned for specific operating ranges. However, as the POCAM will be deployed in harsh and hardly accessible environments, reliability of the module is mandatory. To perform the necessary characterization measurements for the various drivers several PCBs have been designed, which could be utilized in a dedicated characterization setup. The latter will be described in section 3.8. Eventually two circuits were chosen as candidates and will be covered in more detail hereafter.

### 3.4.1 Kapustinsky

The Kapustinsky circuit has been the main LED driver for the first two POCAM generations and benefits from experience and its proven reliability [37]. On that score it will be also used as a crucial pulser in the third POCAM generation. The functional principle relies on a controlled discharge of a capacitor  $C$ , initially charged by a negative bias voltage, via a square trigger impulse signal. The incoming trigger signal opens the NPN transistor and a current flow can be established which subsequently opens the PNP transistor. As a consequence a current path from ground via the LED to the negative bias connection opens. Eventually, the emerging LED flash is effectively cut short as the parallel inductivity counteracts the current flow. The circuit can also be seen as a resonator circuit cut down by a diode after a fourth of the oscillation. A simplified depiction of the circuitry is shown in figure 3.6.

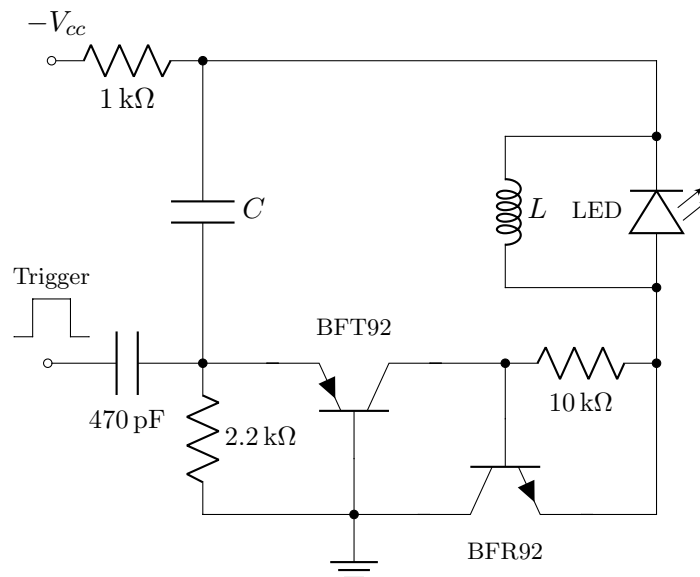
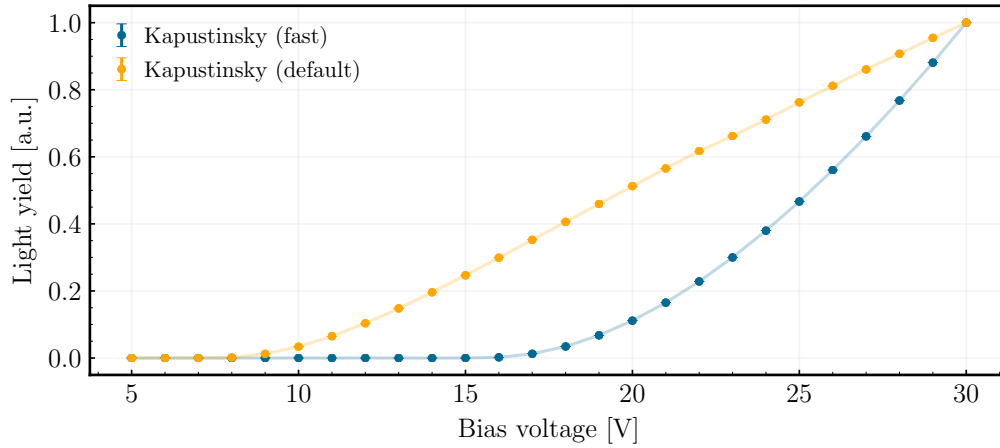


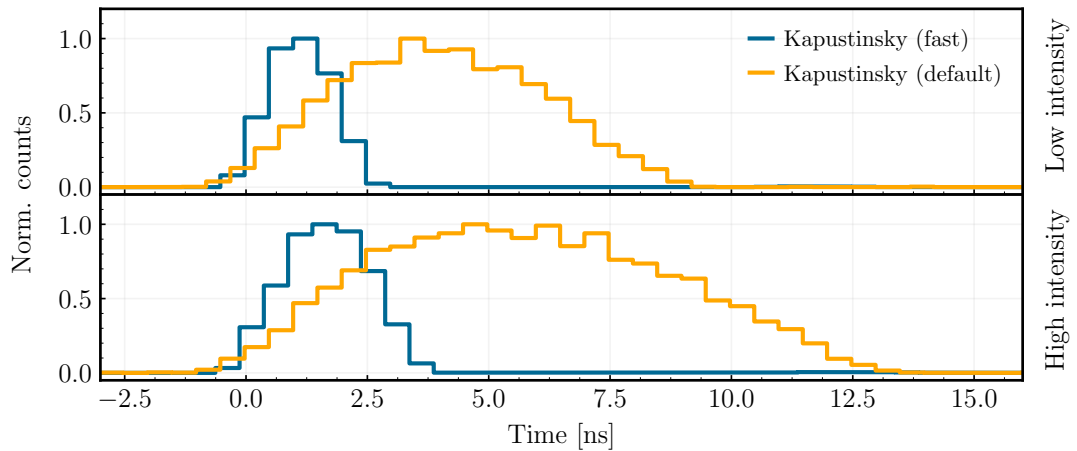
Fig. 3.6: A simplified schematic of the Kapustinsky driver used in the POCAM. The negative bias voltage charges initially the capacitor  $C$  and its discharge is triggered by a square pulse signal. Time and intensity characteristics of the light pulse can be controlled via the values of  $L$  and  $C$ .

The values for the inductivity and the capacity determine the intensity and timing characteristics of the circuit. Generally, longer pulses result for larger values of both [37]. This allows the

utilization of two driver configurations, a faster but dimmer one using a capacity of 150 pF and an inductivity of 22 nH, and a brighter one with a larger capacitor value of 1.2 nF. The latter will be referred to as default configuration in the following. Besides that, altering the achievable intensity is also possible by adjusting the applied bias voltage. This behavior is very linear and can be seen in figure 3.7 (a). The impact of the different capacity and inductivity configurations on the time profile is depicted in 3.7 (b). The former was measured with a photodiode (PD) while the latter was accessed by an avalanche photodiode (APD), using time-correlated single photon counting. In both cases a default 405 nm LED (XRL-400-5E) was used.



(a) Intensity for different bias voltages



(b) Time profiles for both Kapustinsky configurations

Fig. 3.7: The upper figure shows the normalized intensity dependent on the applied bias. Both configurations show a linear behavior. The lower figure shows the different time profiles with respect to the lowest and highest applicable bias voltage. Here, the impact of different values for L and C can be seen.

### 3.4.2 LiDAR-type pulser

A novel type of pulser could be adapted from industrial LiDAR (light detection and ranging) applications. It utilizes a high-current gallium nitride field effect transistor (GaN-FET) capable of switching voltages up to 100 V and currents up to 36 A. These values can be even exceeded once it is used in pulsed configuration [42]. Similar to the Kapustinsky circuit, a controlled discharge of a capacitor bank is initiated by a trigger input signal. The latter controls the output voltage of an ultra-fast gate driver (*LMG1020*) and therefor opens ultimately the GaN-FET (*EPC2001C*), allowing a current flow via the emitter. The basic concept of the circuit is shown in figure 3.8.

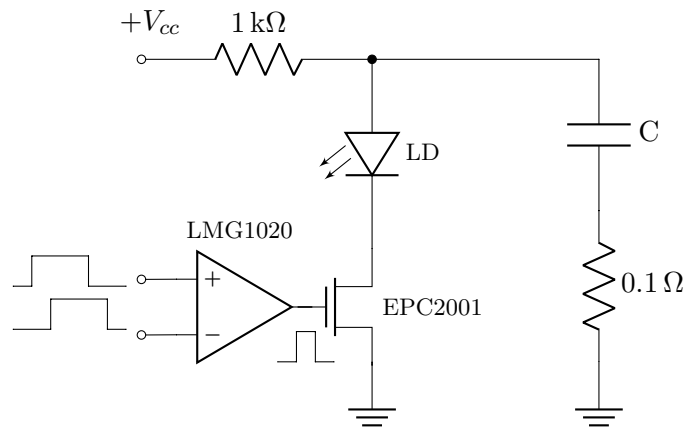
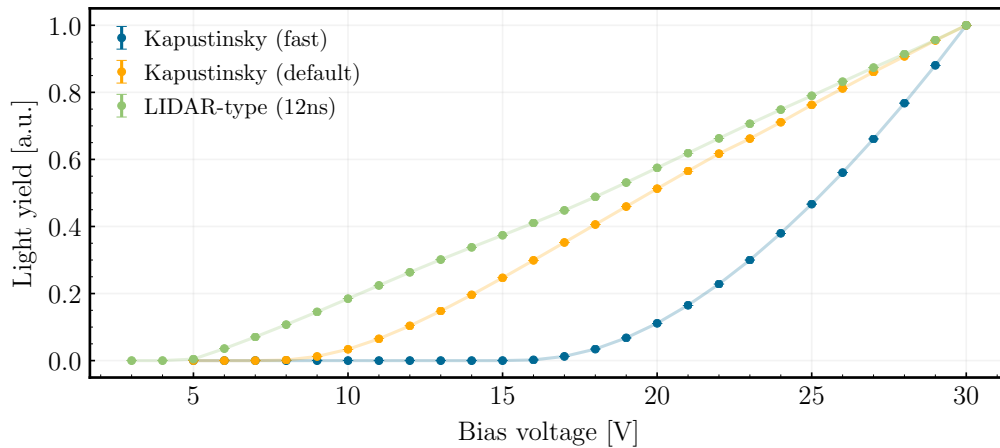
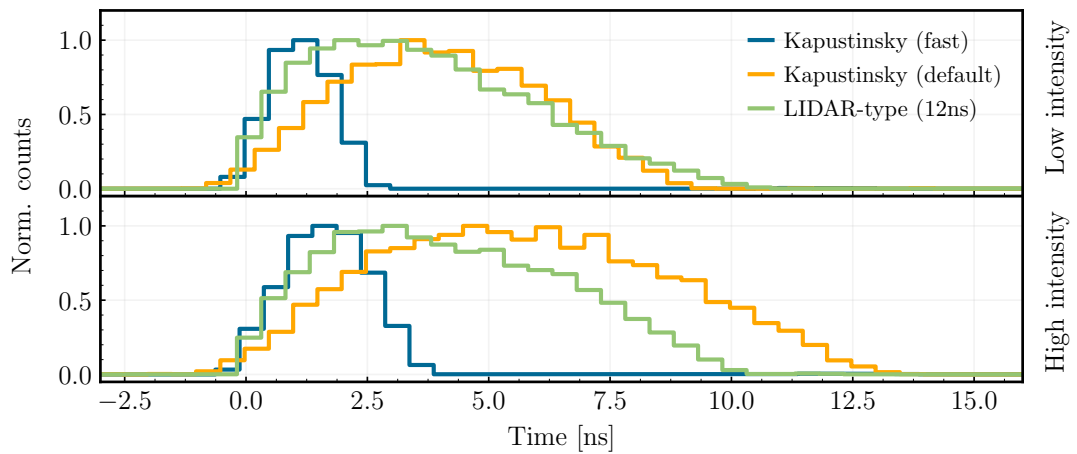


Fig. 3.8: Simplified schematic of the LiDAR-type driver circuit. The capacitor bank is charged via the positive bias signal. A trigger input at the gate driver switches the output high and the GaN-FET opens, allowing the discharge of the capacitor via the emitter. Fine tuning of the timing is possible by applying a delayed trigger signal.

The gate driver offers two logic-level inputs which can be used to fine tune the pulse duration. Therefore both signals are compared internally by the driver while the output follows the difference of both. In particular this means that the pulse driver can be controlled by use of one trigger signal but effectively cut short by a delayed second trigger signal. To avoid additional complexity by supplying two distinct input signals, it is suitable to use a delay of the trigger signal via an RC element. Albeit, the delayed signal must then be buffered by an AND gate before feeding it to the gate driver. To fully exploit the capabilities of the driver the use of a laser diode (LD) is preferable as those offer a higher potential light output. Generally, LDs require larger driving currents, which are simply not obtainable with the Kapustinsky circuit. Furthermore LEDs can withstand the large driving currents achievable by this circuit only to a certain extent. However, UV LEDs can be utilized as they often need large currents to produce a significant light output. Similar to the Kapustinsky driver, the achievable intensity can be determined by the applied bias and also shows a linear response. Here, the effects on the selected pulse duration by different bias voltages is, contrary to the Kapustinsky, hardly observable. The characterization of the pulser has been performed with the same setup as for the Kapustinsky drivers. For this a default 405 nm LD was used (*RLT405500MG*). The results are depicted in



(a) Intensity for different bias voltages



(b) Time profiles for both Kapustinsky configurations and the LiDAR-type

Fig. 3.9: The upper figure depicts the normalized intensity with respect to the applied bias for all flasher types. Every configuration shows a linear response. The lower figure pictures the measured time profiles for the lowest and highest applicable bias voltage for the respective pulse drivers. All of the characterizations have been performed with the default 405 nm LED/LD at room temperature.

figure 3.9, with combined data sets of the three driver configurations for a better comparison.

### 3.4.3 Redundancy modifications

The emitter matrix in each hemisphere is limited by space constraints to a total of six emitters. At first, a symmetrical distribution of two wavelengths per abovementioned pulse driver was considered. However, this implies that the loss of a pulser means also the loss of a specific

wavelength or intensity regime. To mitigate this risk specialized circuitry has been developed to allow for redundancy. In addition to that, different emitter wavelengths can be utilized and driven by various pulsers selectively which ultimately allows a greater variety in the wavelength selection. However, modifying an established driver circuit bears the risk to alter their behavior in an undesired way or the loss of overall functionality. Hence changes need to be carefully considered, tested, and reduced to the necessary minimum. In the case of the Kapustinsky driver additional diodes were integrated in order to block the different charge capacitors from each other. This allows the selection of a specific capacity by switching the applied voltage. To avoid brighter initial pulses the discharge of the unused capacitor must be established by the use of a resistor connected to ground. The circuitry can be seen in figure 3.10. However, two compromises are necessary for this solution. At first, the inductor is shared between both channels which means that the characteristics of the flasher channel can only be altered by the value of the respective capacitor. Besides that, the diode influences the circuit through minor voltage losses and induces a parasitic capacity. Both issues can be mitigated by choosing an appropriate diode and the exact characterization of the complete pulser circuit.

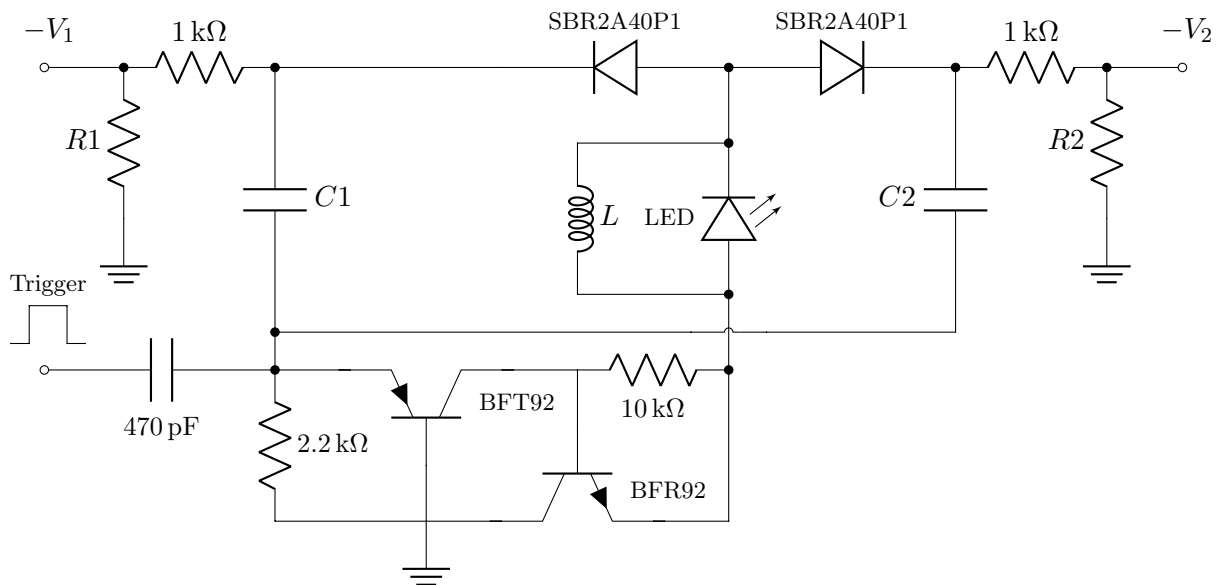


Fig. 3.10: Redundancy modification for the Kapustinsky circuit. Two different LC configurations are possible by selecting the applied voltage on the respective channels. The charging of the unused capacitor is blocked by the respective diode in its path. To avoid brighter initial pulses the discharge of the capacitors is possible via R1/R2.

The LiDAR-type driver is altered in such a way that the connection of in total four emitters to one pair of GaN-FET and driver is possible. This is achieved by the use of optical integrated circuits switchable by an applied external voltage. By doing so the selection of a specific emitter is enabled. Only the respective capacitor bank will be charged while the other can discharge over an additional resistor connected to ground. This ensures that only the selected capacitor can discharge via the LED once a trigger signal is applied. A simplified schematic, displaying

only two emitters, is given in figure 3.11. However, as this does not yet solve the redundancy problem a second driver will be utilized with the same given set of emitters. A selection of the specific driver can then be simply performed by applying the respective trigger signal. Figure 3.12 depicts a general overview of the emitter layout achievable in the POCAM by application of the redundancy modifications. Although both modifications have been tested for functionality and reliability, a complete characterization will be performed with a functional prototype of an analog board. In this way also crosstalk effects between the flasher types as well as parasitic inductivities and capacities induced by the PCB layout can be accessed.

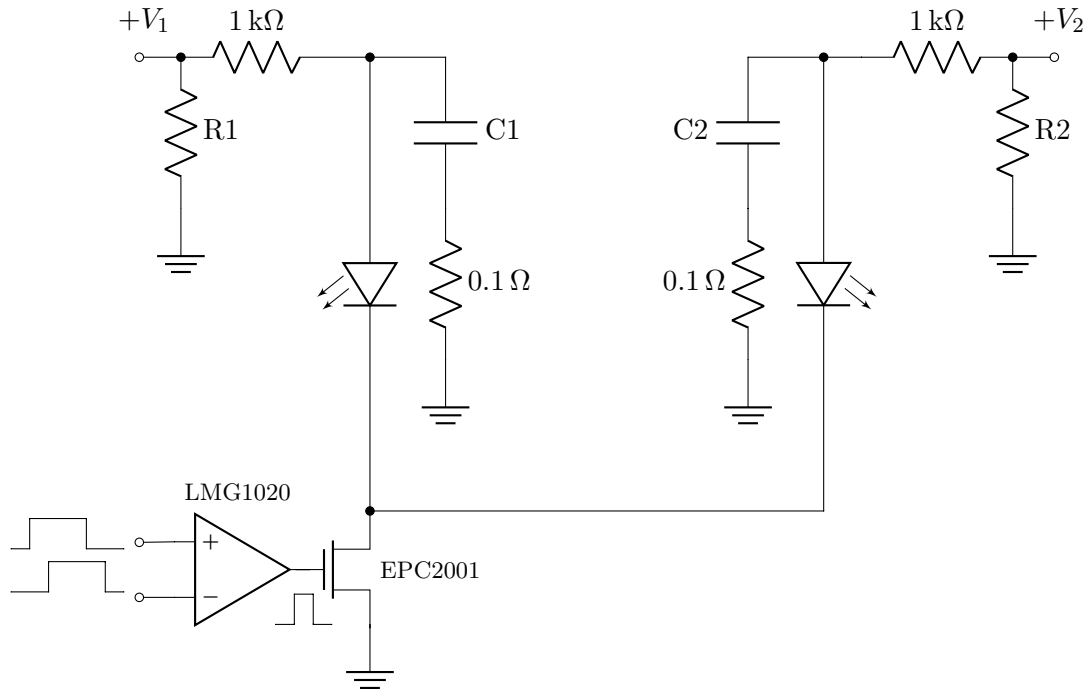


Fig. 3.11: Simplified schematic of the modifications for the LiDAR-type light pulser. By switching the respective voltage a selection of a specific emitter is possible, similar to the Kapustinsky brighter initial pulses are prevented by allowing the discharge of the capacitor bank. Redundancy is achieved by utilizing two gate drivers and GaN-FETs, which share in total four emitters.

### 3.5 Optical emitter selection

The three distinct pulser types offer, as outlined above, different time and intensity profiles. Moreover, the LiDAR-type pulse drivers perform best with laser diodes (LDs), while the current output of the Kapustinsky flashers is only sufficient for light emitting diodes (LEDs). Besides that, the overall performance of the flasher circuits is heavily influenced by the optical emitter itself. Even variations within the same type of emitter can occur through differences in the semiconductor batches between production cycles. An appropriate selection of optical emitters to the respective flasher circuits needs to be performed. The overall emitter layout can be seen in figure 3.12. Here, also the modifications by the aforementioned redundancy circuits are depicted. All of the three flasher types will operate an emitter with a default wavelength of 405 nm. For the LiDAR-type pulser this is the laser diode *RLT405500MG*, for the two Kapustinsky configurations it will be the LED *XRL-400-5E*. The other emitters will be distributed over the considered wavelength regime determined by the acceptance curve of the IceCube DOMs [43]. Various LDs and LEDs have been tested over the course of several weeks. For this, the previously mentioned flasher characterization setup, which is described in more detail in section 3.8, was utilized.

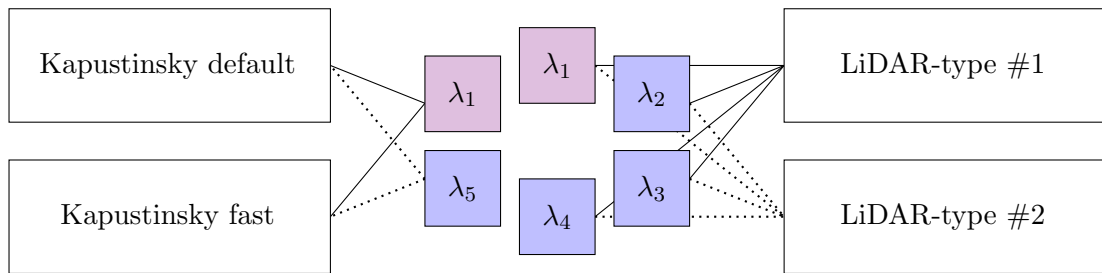


Fig. 3.12: Emitter layout of the POCAM. Two LiDAR-type drivers share in total four emitters (laser diodes and LEDs) while the redundancy modification of the Kapustinsky driver allows the utilization of one LED by two different Kapustinsky circuits.

As outlined in the previous section the intensity characteristics have been accessed by the use of an external photodiode, while the timing behavior was measured by using time-correlated single photon counting with an APD to sample the pulse profile. The latter provides estimates for the achieved FWHM values while the former was used to calculate the attainable total number of emitted photons via

$$N_{ph} = \frac{I_{photo}}{e_{pd}(\lambda) \cdot f \cdot \left(\frac{hc}{\lambda}\right)} \quad (3.1)$$

whereas  $I_{photo}$  denotes the measured photocurrent,  $f$  the flashing frequency and  $e_{pd}$  the wavelength dependent quantum efficiency of the photodiode. The selected emitters and their cor-

Pulsers	Emitter [nm]	Low intensity		High intensity	
		Photons	FWHM [ns]	Photons	FWHM [ns]
Kap. (fast)	XRL-400-5E [405]	$6.3 \times 10^7$	1.4	$2.7 \times 10^8$	2.4
	NSPB300B [465]	$1.2 \times 10^7$	2.6	$5.7 \times 10^7$	3.1
Kap. (def)	XRL-400-5E [405]	$8.5 \times 10^8$	4.9	$4.0 \times 10^9$	8.0
	NSPB300B [465]	$6.0 \times 10^8$	7.6	$2.5 \times 10^9$	10.5
LD (5ns)	XSL-365-5E [365]	$1.3 \times 10^9$	6.3	$1.9 \times 10^9$	6.2
	RLT405500MG [405]	$5.9 \times 10^9$	3.7	$2.9 \times 10^{10}$	4.0
	PL-TB450B [450]	$1.1 \times 10^{10}$	4.4	$4.7 \times 10^{10}$	3.8
	LD-520-50MG [520]	$3.2 \times 10^9$	11.1	$1.4 \times 10^{10}$	6.2
LD (25ns)	XSL-365-5E [365]	$3.0 \times 10^9$	7.3	$7.8 \times 10^9$	10.0
	RLT405500MG [405]	$4.6 \times 10^{10}$	5.5	$1.3 \times 10^{11}$	5.9
	PL-TB450B [450]	$2.1 \times 10^{10}$	5.4	$1.0 \times 10^{11}$	7.3
	LD-520-50MG [520]	$5.5 \times 10^9$	9.7	$2.7 \times 10^{10}$	12.4

Tab. 1: Exemplary light pulser performance for the chosen emitters and their wavelengths at low and high intensity settings, recorded at room temperature. The LiDAR-type driver is referred here as LD and is depicted for two input pulse widths. The scaleable pulse width allows the adjustment of the brightness and, of course, the time profile. The total number of photons was accessed by use of a photodiode.

responding pulse drivers alongside with the achieved values are depicted in table 1. For the LiDAR-type driver two distinct pulse durations have been set. Furthermore, for all flasher types two different intensities, set by the applied bias, are considered. Table 1 shows that the LiDAR-type flasher can achieve a photon output up to two orders of magnitude higher than the Kapustinsky drivers with a comparable time profile. However, the Kapustinsky circuit is extremely reliable and comes with the experience of two former POCAM generations.

### 3.6 Photosensor self-monitoring

The two different photosensors included within the POCAM provide a detector-independent monitoring of the light output. The photosensors are a Silicon-photomultiplier (SiPM) and a photodiode (PD). While the former is used for lower intensities and pulse on-set time as well as duration measurements, the latter accesses integrated charge over a large dynamic range. However, in terms of the PD high intensities are focused. As abovementioned, the aperture disk as part of the internal mounting provides defined solid angles for both sensors. Besides that, it is also used for the mounting of the chosen PD, which is a *Hamamatsu S2281-01*. As SiPM the *Ketek 3315-WB* has been selected. Precise self-monitoring can be achieved by comparing the in-situ monitored light output to the calibration performed prior to deployment. Both distinct sensor readout principles will be introduced within this chapter.

### 3.6.1 Photodiode readout

The photodiode readout is performed by a transimpedance amplifier (TIA) circuitry. For this, the low input current and low noise operational amplifier *AD549S* in photovoltaic mode is utilized. The photocurrent induced by the photodiode is amplified and converted through the TIA according to

$$V_{out} \sim -R_{feedback} \cdot I_{PD} \quad (3.2)$$

while  $R_{feedback}$  denotes the feedback loop resistor. However, as the photodiode exhibits a specific junction capacitance the circuit gain becomes frequency dependent due to the added impedance [44] and follows

$$V_{out} = G(\omega) \cdot I_{PD}. \quad (3.3)$$

Whereby  $G(\omega)$  is still directly proportional to  $R_{feedback}$ , but adds a complex prefactor. For high-frequency applications the frequency dependence can cause ringing due to an effect called gain-peaking. This occurs at a frequency where the gain  $G(\omega)$  finds its maximum, which is without further ado at

$$f_{gp} = \frac{1}{2\pi} \sqrt{\frac{\omega_T}{R_{feedback}(C_{feedback} + C_{PD})}} \quad (3.4)$$

with the transit frequency  $\omega_T$  [45]. By adjusting the value of the feedback capacitor the gain-peaking can be controlled. However, increasing  $C_{feedback}$  comes at the expense of reduced bandwidth and a trade-off has to be found [45]. Although first estimates for a proper capacitor value can be calculated, the overall performance of the circuit depends also heavily on the PCB design as it introduces further capacities or inductivities and adjustments by testing are vital [46]. For the application in the POCAM the feedback values have been set to a resistance of 10 M $\Omega$  and a capacity of 27 pF. The transimpedance stage is followed by an inverting adder with a total gain of

$$g_{adder} = -\frac{R_{feedback}}{R_{input}} \sim -10 \quad (3.5)$$

for the diode path. By adding a DC bias to the amplifier input it is possible to apply an offset on the signal to accommodate for the dynamic range of the analog-to-digital converter (ADC). However, the offset can also be changed by altering the virtual ground on the positive input of the amplifier by a potential divider. Two separate additional inverting amplifiers with a low ( $g_{low} \sim -1$ ) and a high ( $g_{high} \sim -20$ ) gain channel follow the inverting adder. By this, it is possible to tune the signal and their offsets to adjust to the DAQ input voltage range. Figure 3.13 shows the simplified readout concept, albeit, the two distinct offset options are not depicted, but can be seen in the original schematics in the appendix A.6.

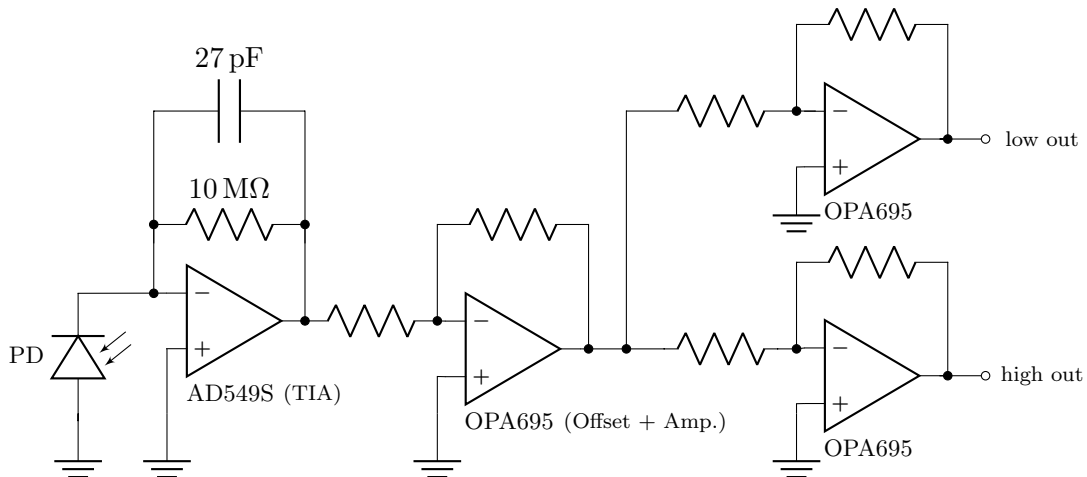


Fig. 3.13: Conceptual view of the photodiode readout stages. The transimpedance amplifier generates an output voltage with respect to the feedback resistor and the induced photocurrent. The output voltage is first amplified and offset by an inverting adder, which is followed by two inverting amplifiers, featuring two distinct gain channels. This permits necessary adjustments to accommodate for the full dynamic range of the future DAQ electronics.

### 3.6.2 Silicon-photomultiplier readout

For the SiPM a two-folded readout is necessary to obtain timing and charge information. However, recording of both, on-set time and charge, comes at the expense of information loss, especially in regard to the charge. To tackle this, the SiPM signal is split in two distinctive paths via two capacitors. The signal is subsequently divided with a respective fraction according to their capacity. Charge information is then obtained by feeding the larger of the two AC-coupled signals into a second capacitor. The latter can be discharged in a controlled manner by grounding either of two resistors. This leads to a discharging curve, which is amplified by a subsequent inverting amplifier. The obtained signal is then fed to a FPGA-based discriminator and a time-to-digital converter (TDC) which accesses the charge by a time-over-threshold (TOT) measurement. Here, the charge is proportional to the signal time-over-threshold, according to the chosen resistor and capacitor configuration, while the discharge constant denotes itself to

$$\tau = R \cdot C. \quad (3.6)$$

Timing information is obtained by use of a fast transistor signal which is controlled by the SiPM response. This signal is eventually also fed to a FPGA-based discriminator and a time-to-digital converter (TDC). The SiPM-readout circuitry has been developed in close collaboration with the GSI Helmholtzzentrum für Schwerionenforschung GmbH located in Darmstadt, Germany. The necessary FPGA and TDC developments have been performed by Michael Böhmer (Zentrales Technologie Labor (ZTL)). A schematic view of the circuitry is shown in figure 3.14.

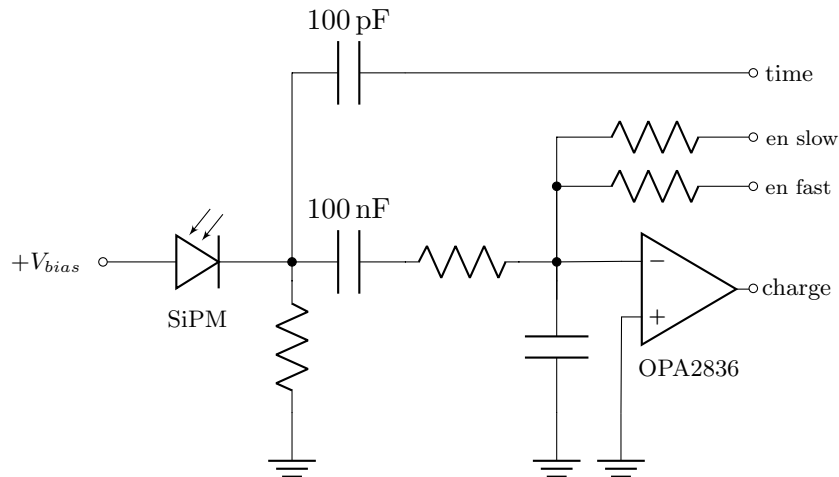


Fig. 3.14: Schematic of the utilized SiPM-readout. The SiPM pulse is split and fed into two channels to obtain charge and timing information. The charge readout relies on the controlled discharge of a capacitor and the correlated measurement of the discharge signal via time-over-threshold recording. Timing is accessed by use of a fast switching transistor. Both signals are fed into a FPGA-based discriminator and eventually a time-to-digital converter. The circuitry has been developed in close collaboration with GSI, located in Darmstadt, Germany.

### 3.7 Communication and power electronics

The basic functionality of the module, by means of the above described analog circuitry for flashing and self-monitoring, and the corresponding control by the digital board, can be adjusted to various specific detector interfaces. As this POCAM generation was specifically adapted to the IceCube Upgrade the communication to the module is mainly handled by three IceCube-specific boards. The interface to the IceCube network is the IceCube communications module (ICM). It links to the IceCube data-, clock- and power stream and provides proper communication protocols as well as synchronization signals. A secondary board, with a micro-controller unit (MCU) as main part, supplies then hard- and software similar to the DAQ of the IceCube Upgrade sensor instruments. This is interfaced by the so-called distribution board which assigns data-, clock- and communication streams as well as power to both hemispheres by use of an FPGA. Every FPGA on the digital board at the respective hemispheres receives thereby slow control commands and clocks from the MCU. This is used to set up the FPGA registers accordingly to the respective measurement run. Thereby parameters for the flasher circuits and photosensors are set correspondingly. The power supply is handled by a separate PCB. For the ICU a 96 V supply and a maximum power consumption of 8 W is foreseen. The internal photosensors will monitor the intensity and timing characteristics once a flash was performed, while the recorded data will be written to the internal FPGA storage. This can be accessed by the MCU board and linked to the IceCube data stream for further offline processing. At the current state the mini mainboard (Mini-MB), containing the ICM and the secondary

MCU board, is in advanced prototyping. The further development of the distribution board and digital board depends on its final design and will be the next important steps for the third POCAM generation.

### 3.8 Characterization setups

The aforementioned flasher circuits and the optimizations regarding the emission profile have been characterized by the use of two dedicated calibration setups. These will be also further utilized to calibrate complete modules individually and shall be covered in greater detail within this section.

**Relative flasher characterization.** The flasher characterization setup utilizes a photodiode, a PMT, an avalanche photodiode (APD), and a spectrometer. All of the four different sensors are located in a dark box, while the flasher circuit itself is placed in a temperature chamber (*ESPEC MC-712*). Coupling of both setups is then performed by a 4-to-1 fan-out fiber connected to the flasher circuitry via a custom-made fiber adapter, which faces directly on the respective emitter. The temperature chamber is capable of reaching, and holding, temperatures between  $-75^{\circ}\text{C}$  and  $+100^{\circ}\text{C}$ . For most detector environments mainly temperature extremes in the subfreezing regime are of interest, especially in the case of glacial ice. Therefore the temperature chamber is mainly used as freezer. To reduce potential systematic uncertainties, especially at the fiber coupling, which could emerge during cooling and heating due to humidity in the chamber, it is flushed with nitrogen. For the calibration of a complete module hemisphere also a temperature-stabilized reference halogen light source will be coupled to the integrating sphere. This allows the correction of potential changes during the calibration, for instance through the mentioned fiber coupling disturbances. The intensity is recorded by the photodiode and the PMT. While the former is readout via the picoamperemeter *Keithley 6485*, the latter is evaluated by a digital oscilloscope. Time profiles are measured with the aid of the APD, using time-correlated single photon counting. A neutral density filter wheel is utilized to achieve low occupancies (sub-10%) to provide appropriate single-photon sampling of the time profile. For the APD readout a high-precision TDC is utilized. Lastly, the emitted spectrum is recorded by the spectrometer, which is accessible by serial commands. A dedicated computer controls all the necessary software as well as peripheral electronics and sub-components. A conceptual view of the setup is given in figure 3.15.

**Relative emission profile characterization.** For the emission profile characterization, a separate dark box with a total length of around 140 cm is used. Here, a fully assembled hemisphere including the integrating sphere, aperture disks, and a dedicated illumination PCB is mounted on a two-axis rotation stage assembly. The latter consists of two separate rotary stages, which feature sub-degree precision. In this configuration, scans of the emitted profile for a given set of azimuth and zenith angles can be performed. The illumination board provides the same layout of the emitter matrix as the analog board but utilizes switchable LEDs in a constantly operated forward mode. A *Keithley 6485* picoamperemeter is used to measure the photocurrent induced by a photodiode, which is mounted on the opposite side of the dark box.

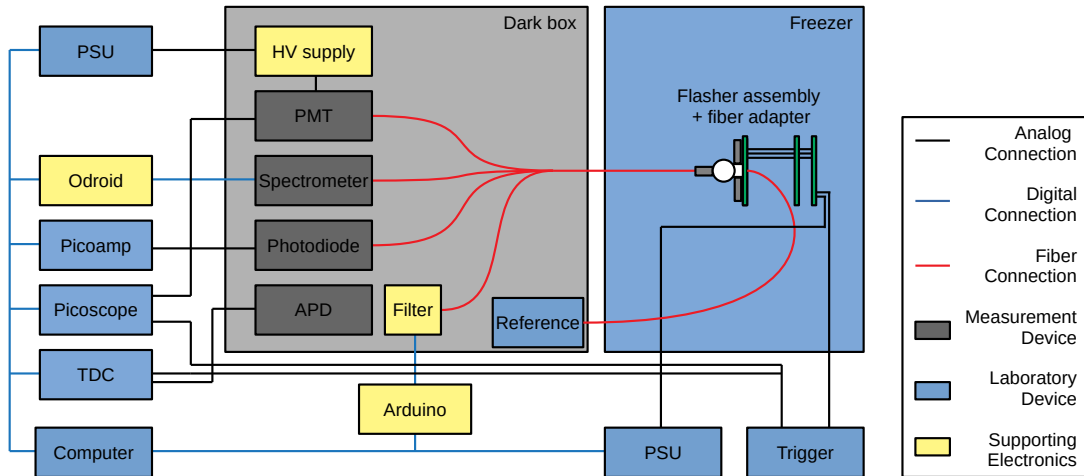


Fig. 3.15: Schematic view of the calibration setup for the flasher characterization. Four different sensor types are located in the dark box while the flasher is placed in a temperature chamber. Image courtesy of Leonard Geilen.

A dedicated computer measures the achieved intensity, sets the azimuth as well as zenith angles, and performs the LED selection. Light baffles mounted between the emitter and sensor are used to reduce the impact of light scattering on the surfaces of the dark box. Additionally, dark current measurements are performed between the runs. Figure 3.16 provides an overview of the workflow of this setup, including the necessary peripheral electronics.

**Absolute calibration.** Complete POCAMs will be absolutely calibrated as well. The instrument will be placed therefore in the aforementioned emission profile setup and the regular photodiode will be exchanged with a NIST-calibrated diode. By iterating through all emitters, pulse drivers, and a set of different configuration parameters, an absolute intensity scale to all previous relative calibrations can be measured, by monitoring the induced photocurrent. This data will be used as reference for the self-monitoring data over the deployment period and can be used to correct the emission in-situ by use of the self-monitoring capability of the POCAM and the linear response of the circuits to the applied bias. Systematic uncertainties of the detected volume and the instruments can be accessed by accurate simulation studies, which should be enabled by precise knowledge of the relative and absolute behavior of the POCAM.

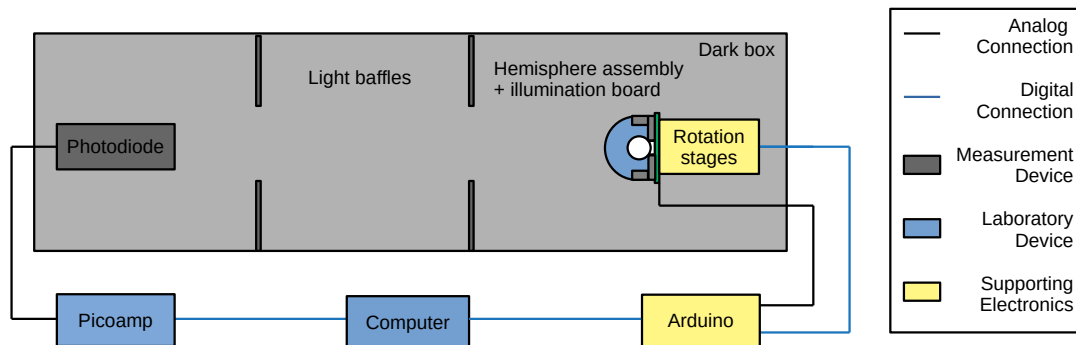


Fig. 3.16: Conceptual workflow overview of the emission profile characterization setup. The hemisphere assembly on the right hand side can be rotated via two rotary stages. The induced photocurrent from the photodiode is measured by a picoamperemeter. Figure kindly provided by Leonard Geilen.

### 3.9 Conclusion and outlook on the POCAM activities

The development of the third generation POCAM for the IceCube Upgrade is in a very advanced stage. In the scope of this thesis, environmental resistance tests for the titanium housing have been successfully performed to ensure its resistance against the harsh environments of future deployment sites. Dedicated characterization setups have been built and utilized to investigate novel pulse driver circuitries and optimizations regarding the emission profile, and will be further employed for the calibration of complete hemisphere assemblies. Here, several flasher circuits have been developed and were examined to improve the dynamic range of the POCAM and narrowed down to two candidates, the Kapustinsky driver and a LiDAR-type pulser. Further modifications for both circuitries allow for redundancy and expand the available set of emitters. Various types of the latter were tested to find appropriate candidates for the two pulse drivers. The photosensor readout has been adapted to temperature stable devices and sensors. Further characterization of the newly developed analog circuitries will be performed with a functional prototype of the analogboard, which allows the access and mitigation of PCB layout induced systematics. The analogboard is currently designed by myself. The development of the digital board by Michael Böhmer as well as the distribution PCB by Felix Henningsen depend on the final version of the IceCube communication module and its supplementary devices, and will go on once a finalized prototype of the latter is available. Parallel to this, simulations for the deployment within P-ONE and adaptations of the communication electronics to the P-ONE infrastructure will start.



## 4 Pathfinder missions for P-ONE

The neutrino sky is presently covered at the very high energies only partially by IceCube due to its location in the Southern hemisphere. More observatories are necessary in the North to complement the coverage of the neutrino sky. The Pacific Ocean Neutrino Experiment (P-ONE) pursues the vision of a new neutrino telescope in the northern hemisphere as addition to the ones existing or currently under construction to close gaps in sky coverage [47]. One of the triggering circumstances that lead to the development of P-ONE was an existing cabled observatory, NEPTUNE, located in the north-east Pacific Ocean on the coast of British Columbia. It is the biggest such installation by Ocean Networks Canada (ONC), an initiative of the University of Victoria. NEPTUNE was finished in 2009 and comprises an 800 km loop of fiber optic cables and provides access at five different nodes, distributed over the Juan de Fuca tectonic plate. Each node serves as connection point for distinct experiments and provides high-bandwidth data (10 Gb/s) and high-power (9 kW/node at 400 VDC) connections [8, p.415]. Here, a junction box (JB) serves as an interface to the experiments, in some cases, a mini junction box (MJB) is used as an intermediate step. The latter is tailored by ONC to the specific experiments and hosts power converters, Ethernet switches, and provides monitoring and control by means of micro-controllers. The node at the Cascadia Basin in a depth of 2600 m is located on an abyssal plain and was selected to host P-ONE. Abyssal plains are submarine surfaces with little deviancy in depth formed by terrigenous sediments [48]. This provides a nearly flat structure, suitable for neutrino telescopes, as they encompass a large area. Eventually, the success of the first POCAM prototype, deployed within GVD Baikal [35], led to the formation of the STRAW collaboration and the initiation of P-ONE pathfinder missions, which will be subject of this chapter.

### 4.1 STRAW - Strings for absorption length in water

The first pathfinder mission STRAW, has the main goal to characterize the optical properties of the deployment site, Cascadia Basin. The focus lies on the measurement of the attenuation length to classify the location in regard to P-ONE. Besides that, also long term studies of the environmental background should be performed. The background is mainly composed of two components: bioluminescence, induced by living organisms in the deep-sea, and radioactivity, primarily potassium decay. STRAW was deployed in June 2018 and continuously takes data since then, the overall design and concept will be explained hereafter.

**Modules and electronics.** STRAW utilizes two types of instruments to access the optical properties: optical emitter and receiver modules. The former are predecessors of the POCAM, described in section 3, while the latter are specially developed sensor modules, called sDOM [38]. Each sDOM utilizes two 3" photomultiplier tubes (*Hamamatsu Photonics R12199*) accommodated in a larger version of the POCAM titanium housing, with one PMT facing downward and the other upward. Data readout is performed with time-over-threshold measurements by a combined system of a TRB3sc and Padiwa board, initially developed at GSI for collider experiments. A dedicated splitting board divides the PMT signal to four levels. By this, four different

thresholds could be configured to achieve a higher sampling rate. Time synchronization is intrinsically performed by combining several TRB3sc boards via a 2 GBit fiber line (TRBnet). However, this was not possible within STRAW as it uses copper cables for communication. An alternative approach was developed by Michael Böhmer (ZTL), in the form of the Medusa board. This is located in the MJB of each string and provides a synchronization signal by use of the LVPECL signal standard to the modules [38]. Both Medusa boards in the respective MJB can be either used in stand-alone or master-slave mode to enhance redundancy. The TRB3sc-based readout will be also utilized as the base for the STRAW-b modules and hence described in more detail within section 4.2.1.

**Deployment and mechanics.** The design of STRAW is based on a two mooring line configuration. Each mooring line hosts four modules, in total three POCAMs and five sDOMs are deployed. Hereby, the POCAM induced light flashes can be detected by sDOMs at various distances. Redundancy is achieved by an almost identical layout of both mooring lines, with aligned modules at different heights. Figure 4.2 provides an overview of the complete structure. However, adequate measurements can only be performed with a free line of sight between the two strings. This is achieved by using two bearing steel lines instead of one. This reduces the risk of twisting of the mooring lines due to the sea current. Furthermore, cable shadows are avoided as the modules can be mounted on one side of the parallel structure. The deployment of each mooring line was performed with remotely controllable winches, depicted in figure 4.1. Here, a complete string with its four modules is wound up on one winch and during the deployment slowly unwound. This operation is performed from the back deck of the deployment vessel while a rigid-hulled inflatable boat (RHIB) and an additional floating buoy secure the string prior to lowering it to the seafloor. The MJB has been attached after unwinding of the complete string and the complete structure was lowered with controlled speed by the aid of a heavy-lift-line. A rotatable anchor allowed ultimately the alignment of the mooring lines. This was performed during the remotely operated vehicle (ROV) operation for the connection of the mooring lines to the JB. Here, also a daisy chain connection between the respective MJBs has been realized to distribute the timing signal by the Medusa board to both strings.



Fig. 4.1: Photography of a mooring line assembly hosted on the winch, as it was lowered into the test pool of ONC. Picture taken by Felix Henningsen.

**Analysis and results.** An initial analysis of the attenuation length was performed by Christian Fruck. Preliminary results were presented during the International Workshop on Next Generation Nucleon Decay and Neutrino Detectors (NNN18) with values of  $31.4 \pm 8$  m for a wavelength of 465 m [49]. Additional analyses to verify the results are currently performed by the University of Alberta (UofA) and within our institute. In terms of background, the rate

ranges from 10 to 100 kHz while peaks to several MHz can be observed, most likely induced by the bioluminescence of ambient deep-sea organisms [38]. Besides these efforts, new instrumentation systems will be deployed in the scope of STRAW-b, which aims for further characterization of the site and the verification of the results achieved by STRAW.

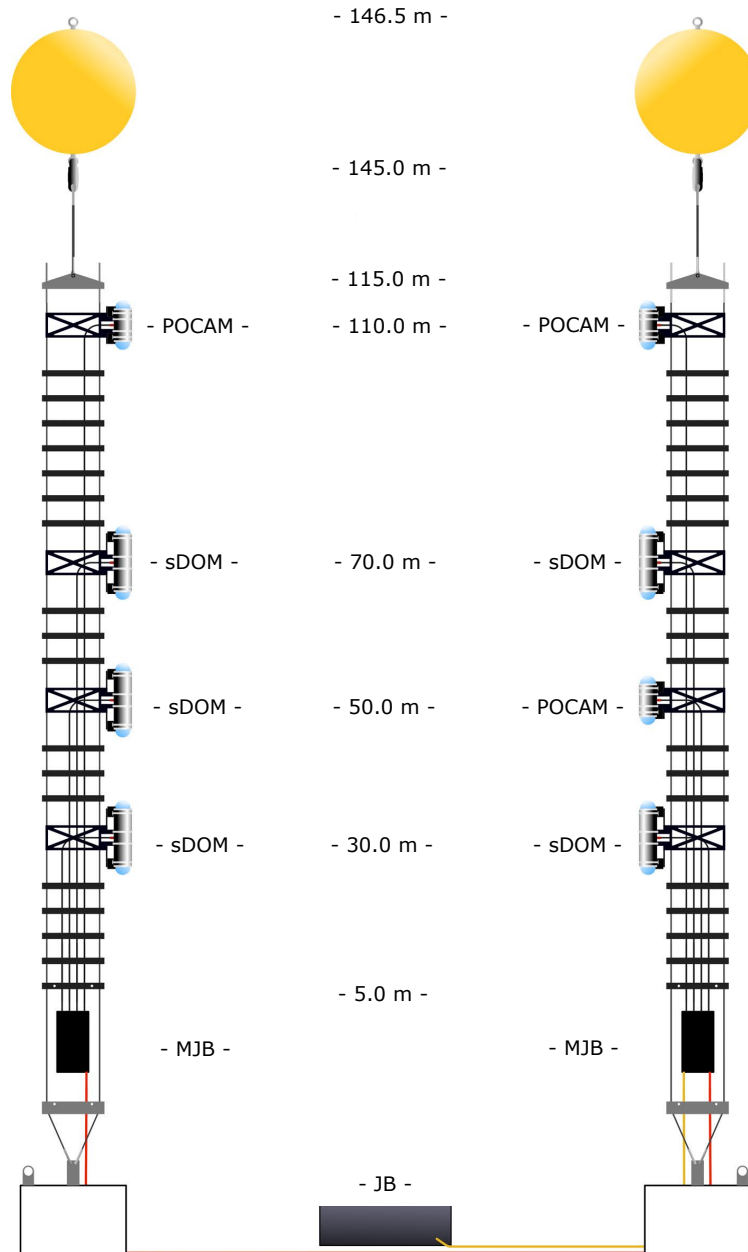


Fig. 4.2: Schematic view of the two STRAW mooring lines. Each string hosts four optical modules, positioned at different heights. The horizontal spacing between the lines is roughly 37 m. For more details refer to the text. Figure courtesy of Kilian Holzapfel.

## 4.2 STRAW-b

The results of STRAW motivated a follow-up mooring line, STRAW-b, as second pathfinder mission. Primary tasks are the verification of the attenuation length measurements of STRAW, an in-depth study of the bioluminescence background, and the development of suitable deployment strategies for future P-ONE mooring lines. The modules of STRAW-b are basically divided into two sections. Standard modules deliver pressure, temperature, and humidity signals from defined mooring line positions and serve basically as checkpoints for a successful deployment. Specialized modules, on the other hand, are pursuing directly the aim for further characterization of the deployment site. The overall design of STRAW-b is hereby based on hybrid optical cables and 13" glass spheres to mimic the envisaged structure of P-ONE as closely as possible. For the complete mooring line, ten modules are planned: two LiDARs, two PMT-based spectrometers, a CCD-based spectrometer, a muon tracker, and four standard modules. The latter serve basically as a base platform for all modules and will be covered in the following.

### 4.2.1 Standard modules

For STRAW-b, one module has been developed as a generalized module. This standard module provides the base for the attachments of the specialized modules. For this, they accommodate a readout system, on the basis of the TRB3sc and a modular mechanical substructure to mount arbitrary supplements for the specialized modules. Besides that, the developed readout system can also be used as core for the optical modules of P-ONE. The standard module delivers data for internal pressure, temperature, humidity, and host magnetic field sensors as well as accelerometers. By this, they provide a valuable ping signal from all module positions, which can be used to monitor their individual system status.

**Electronics.** Data transfer and power connection between the modules and the MJB is handled by individual hybrid cables, called vertical electrical optical cable (VEOC). Each of those cables comprises two 22AWG copper wires, used for power supply, and two single-mode fibers for communication. The readout is centered around the TRB3sc, an integrated readout system on the basis of an FPGA with central trigger system, slow control, gigabit Ethernet and time-to-digital converters (TDC). This device has been developed for collider experiments by GSI in Darmstadt and benefits therefore from experience and proven reliability. The front-end to the TRB3sc is the so-called Padiwa, which amplifies and shapes the signal of the 16 inputs to allow a proper time-over-threshold measurement. The photosensor signal of the individual specialized modules is fed to the Padiwa via the padAdap, a small adapter board. Communication to the devices is handled by an Odroid C2. The connection between the C2 and the TRB3sc is established by a carrier board, called Phobos. Power conversion by means of switchable DC-DC converters, as well as several digital-to-analog converters (DAC) and ADCs are also located on the Phobos. Furthermore, environmental sensors for pressure, temperature, humidity, acceleration, and magnetic field are hosted there and readout by the Odroid via an I2C-connection. Power consumption of the individual DC-DC converters can also be monitored via I2C. As the connection to the Odroid is based on Ethernet, a media converter is utilized as

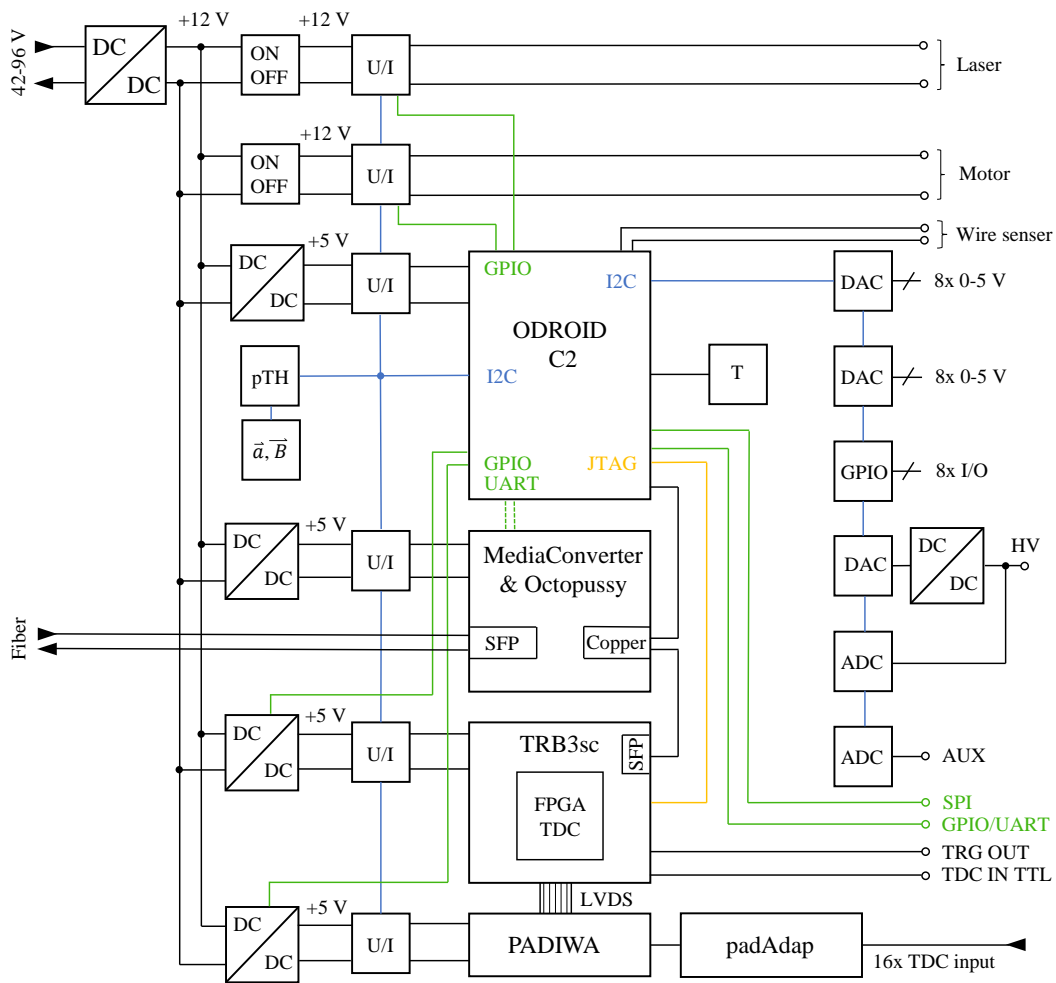


Fig. 4.3: Simplified block diagram of the electronics for the standard module. Specific functions can be tailored to the respective modules by software modifications. For more information on the base electronics refer to the text.

an interface to the VEOC fiber connection. A small supplementary board (Octopussy) replaces the micro controller hosted on the media converter, which transforms it into a configurable Ethernet switch. Port-based VLAN is implemented as startup configuration, isolating the TRB3sc Ethernet port from the SFP uplink. By this, a data transmission overload due to hard- or software failures can be circumvented and the accessibility of the module ensured. Figure 4.3 depicts the general readout structure with the mentioned subsystems. Additionally, a battery-powered data logger (Uboot) is hosted in the modules to record specifically the acceleration and orientation of the instruments during the deployment. A magnet taped to the glass housing must be removed just before the deployment to switch a magnetic relay and initiate thus the data taking by the Uboot. The design of the readout electronics was performed by Michael Böhmer (ZTL) in close-collaboration with GSI.

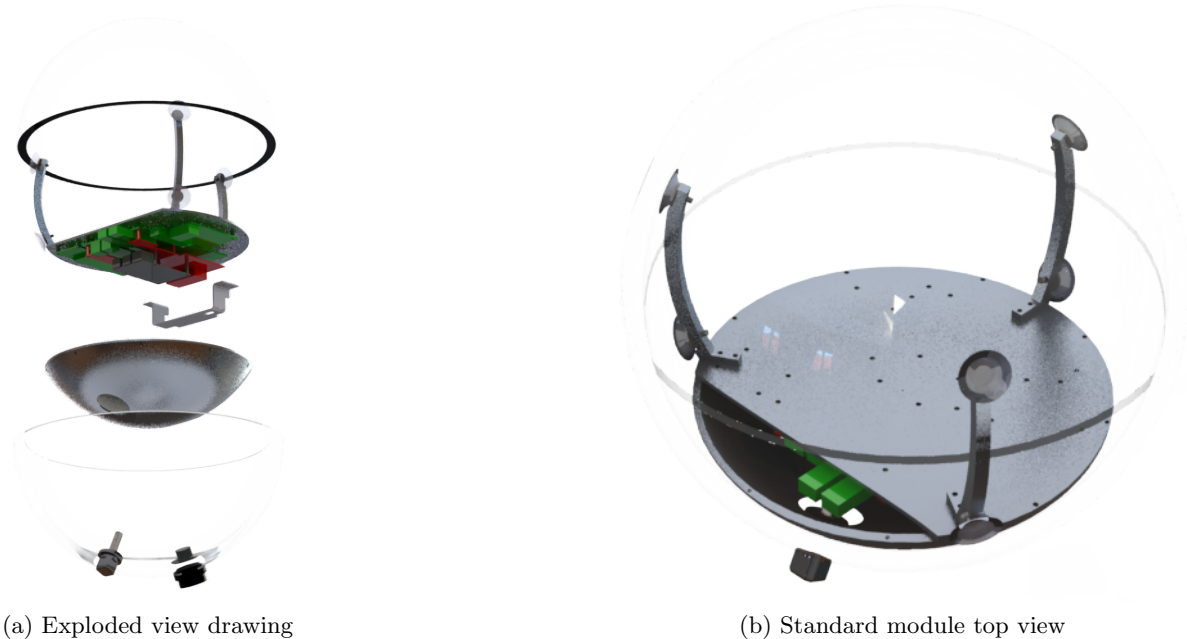


Fig. 4.4: The internal design of the STRAW-b standard module. The readout electronics is mounted upside down on a laser cut aluminum plate. Heat dissipation is performed by an aluminum bowl attached to the glass via optical gel, while the entire structure is held in position by suction cups, which work as springs.

For complementary multi-band attenuation measurements in combination with the spectrometer modules, an additional light flasher has been developed. The design is based on a flash LED driver (*LM2759*) with an I2C compatible interface, commonly used for camera flashes in mobile phones. The *LM2759* controls the current flow through the LED and further allows adjustments in terms of pulse duration and current intensity. The utilization of several flashers within one module is enabled by the use of an I2C address translator upstream to the driver device. Here, the initial address is fed through to the following light flashers, while the onboard translated address is used for the LED driver. The overall schematic of this circuit is shown in the appendix A.13. Calibration and attenuation measurements with the spectrometer modules can be performed by downward facing LED drivers, located in the respective modules above. For this, white and blue LEDs will be utilized.

**Mechanics.** The instruments of STRAW-b will be enclosed in a 13" glass pressure housing produced by Nautilus [50]. Hereby internal and external design goals, as well as constraints, for future optical modules of P-ONE, can be accessed. The main goal for the standard module is to provide sufficient space for the individual supplements of the specialized modules. For this, the previously mentioned readout electronics had to be fitted to a minimal volume within the sphere. Furthermore, the dissipation of heat, mainly induced by the FPGA and the initial DC-DC converter, had to be considered. The overall design of the mechanical substructure

can be seen in figure 4.4. Here, a large heat sink in the form of an aluminum bowl, which is thermally attached to the surrounding glass body by optical gel, builds the foundation. The readout electronics is mounted upside down on an aluminum plate, which can be customized for the respective specialized modules. Only the necessary mounting points for the readout electronics, aluminum bowl, and mounting strives are predefined. The last mentioned strives follow the radius of the sphere and hold the mechanical structure by the aid of suction cups. These are working in this configuration as springs and keep the mechanical structure tightly in position. Besides, also the connection of the aluminum bowl via the optical gel is adhesive and secures the structure additionally. The heat transfer from the FPGA and the DC-DC converter is performed by respective heat sinks thermally connected to the mounting plate and thus to the aluminum bowl. The surrounding ocean can then be used as a heat reservoir by the connection of the aluminum bowl via the optical gel to the glass body. The complete mechanical substructure with enclosed readout electronics is located 75 mm below the sphere equator. Distinctive specialized module supplements can be mounted in the entire remaining space. The glass sphere is closed by sealing and adhesive tapes. Underpressure is applied via a vacuum port afterward, which ensures the seal tightness and eventually sealing the sphere supplementary.

#### 4.2.2 Specialized modules

The further characterization of the deployment site is the task of the specialized modules. The main objectives are the verification of the attenuation length measurements of STRAW and a more profound understanding of the bioluminescence background. The specialized modules will be introduced in this section. However, as they will be subject of different publications, the introduction is limited to a brief overview. As most of the modules perform optical measurements, with exception of the muon tracker, their upper hemisphere is a specifically optical enhanced glass, which allows an unimpeded field-of-view.

**LiDAR.** The LiDAR (light detection and ranging) modules aim to complement the attenuation length measurements of STRAW. The design is based on a *ThorLabs NPL45B* pulsed diode laser with a wavelength of 450 nm, which is rotatable in azimuth and zenith by two rotary stages. Backscattered photons will be focused by a lens system onto a micro PMT device for counting. Calibration of the system is enabled by a photodiode (*PD-S3590-08*), followed by a transimpedance amplifier stage, shown in A.14, and a Hamamatsu spectrometer (*C12880MA*). Here, a reflective foil prevents the photodiode from overexposure and is aligned in such a way that the reflected photons are focused on the spectrometer device. The latter uses a thin sheet of teflon to pre-diffuse the incoming light to account for small misalignments. For the complete STRAW-b mooring line two LiDARs are planned. Hereby, different scattering angles can be scanned by using one as emitter and one as a receiver, also differences of the optical properties due to the ocean depth are accessible. Additionally, by aiming at calibrated reflectors at defined positions along the mooring line the overall attenuation can be measured.

**PMT spectrometer.** Bioluminescence of deep-sea organisms can pose a major background source for ocean based neutrino telescopes [51]. Bearing this in mind, two PMT spectrometers

intend the further characterization of the bioluminescence at the Cascadia Basin. For this, each of the two spectrometers hosts twelve PMTs with different wavelength filters to monitor the spectrum and intensity of nearby bioluminescent organisms. The wavelength regime of the filters is thereby centered around the expected bioluminescence spectrum [52]. Also, by exploiting the quantum efficiencies of two different PMT types (*Hamamatsu R1924A and R1925A*), the overall module efficiency is increased. A specially designed 3D-printed holding structure aligns the PMTs to the same field-of-view by accounting for differences due to their arrangement and refraction. Furthermore, the incoming light is focused on the PMTs by use of lenses. An additional camera within the module is switched on in the case of a bioluminescence burst and aims to depict the respective organism. The previously mentioned LED drivers are used as spotlights.

**CCD-based spectrometer.** The CCD-based spectrometer is a complementary approach to access the properties of the deep-sea bioluminescence at the Cascadia Basin. Other than the PMT spectrometers, it utilizes commercially available small Hamamatsu spectrometer devices (*C12880MA*). The readout is based on an FPGA in combination with an ADC, developed by Michael Böhmer (ZTL). Five of these spectrometers will be hosted inside one module. Similar to the PMT spectrometer, a camera is activated in the case of an emerging signal. The three spectrometers of STRAW-b will be located at different heights to access eventual distinct bioluminescence properties induced by the sea depth.

**Muon tracker.** The muon tracker has been designed to measure the muon rate in the Pacific ocean. For this purpose, it utilizes two separate detection arrays positioned at a certain distance. Each array comprises four plastic scintillator tiles (*BC-404*), where the deposited energy of the muon is readout by SiPM matrices. One matrix consists in total of nine SiPMs in a parallel connection, which is shown in the appendix A.15. Each scintillator tile features two SiPM matrices in opposite corners. The plastic scintillators are enclosed in a diffusive reflecting teflon holding structure to optimize the light yield. Furthermore, highly reflective foils at the bottom and top of each tile minimize losses additionally. Approximate directional information can be obtained in the case of time correlated events in separate scintillator tiles.

### 4.2.3 Deployment strategy

Deployment methods of mooring lines are generally differentiated by two main approaches: top-down and bottom-up. The latter refers to a deployment of an enclosed structure to the ocean bed, while the unfolding of the mooring line is triggered by release mechanisms and subsequently due to the buoyant force. During top-down procedures, the mooring line is lowered to the seabed from the sea surface, often by the aid of a heavy-lift-line from the deployment vessel. Top-down approaches can be performed anchor or buoy first, which refers to the part initially lowered to the sea surface. Buoy first approaches require to stretch the mooring line on the sea surface first, which increases the deployment duration. However, anchor first deployments increase the mechanical stress, due to the sea state and load on the mooring line and equipment. Besides the method, also other aspects need to be taken into account for the deployment. Sea state, wind speed, and swell play important roles as they affect the ship positioning, the crew, and the

scientific instrumentation. Also, the initial positioning of the mooring line is highly influenced by the sea state. The deployment procedure must take this into account and, despite that it can be coupled to a specific sea state, it must be straight forward and fast to account for changes in the weather. Deployment operations are therefore often defined as a daylight operation with a stable weather window for at least 12 hours. Despite that, marine operations and the handled equipment have to be designed in due consideration of the emerging characteristic loads and sea conditions. Besides, they need to be practicable and safe.

The design of the STRAW-b mooring line is centered around the 14 VEOC communication cables, which were inherited from a former experiment. The shortest hybrid cable has a length of 120 m, which iteratively increases by steps of 24 m up to a maximum length of 432 m. As aforementioned, a total of ten instruments will be deployed, which allows to use the remaining four cables as spare and for testing purposes. The hybrid cables are molded in *SEACON OPT-G-4-CCP* dry-mate connectors. Especially the connector was one of the main concerns for the design of the external mounting and the deployment procedure, as they have an approximate length of 20 cm and pose therefore a large lever arm. Hence, the glass sphere could be seriously damaged by mechanical shocks or an increased strain on the connector or cable. Despite this, the optical fibers are susceptible to damages induced by bending stress and squeezing. By taking these factors into account, a buoy first top-down approach has been chosen as the deployment method, similar to STRAW. However, as it was, unlike for STRAW, not possible to store the ten modules alongside the steel line on a single winch, simply due to their amount, the structure had to be separated. Out of this the VEOC and modules are stored on an instrument tray while the bearing steel line is separated on a winch. During the deployment, both structures have to be merged on the back deck of the vessel. The combined parts of the mooring line will be then stretched on the sea surface, while a RHIB and additional floating buoys secure the line. Once the entire mooring is stretched, the anchor will be lowered by a heavy-lift-line. The RHIB, securing the top of the string, moves in parallel back to the main vessel. As soon as the mooring is in a nearly upright position, the anchor is disconnected from the heavy-lift-line by an acoustic release, while the additional buoys ensure that the mooring line floats. The load is transferred to the buoys afterward and the supplementary buoys removed. Finally, the mooring line is lowered in a controlled manner to the seabed by the heavy-lift-line. Inspection of the string and the connection to the junction box will be performed during an ROV operation after the deployment. The deployment method had a significant impact on the design of the single STRAW-b components, which will be covered in the following.

**Steel cable and winch.** The mechanical backbone of STRAW-b is a PG-012 steel cable produced by PFEIFER GmbH & Co. KG. This is a spiral rope with 19 one wire strands and a diameter of 8.4 mm. Along the total length of 444 m, ferrules are attached every 12 m to provide anchor points for the module mountings. A defined rectangular side is used to hold the modules in position, while the pressed part of the ferrule is of cylindrical shape. The wire rope has a minimum breaking load (MBL) of around 68.1 kN and is terminated on both ends with closed swaged fittings. For corrosion protection, the steel is coated with a galfan zinc-aluminum alloy [53]. The steel cable is spooled on a hot-dip galvanized cable reel. For the deployment of the wire rope, one of the winches constructed for STRAW will be reused. They have been designed by Andreas Gärtner and are described extensively in his master thesis [54]. As the winch had

to host the cable reel of STRAW-b, the axis was stripped from STRAW specific components. By use of additional adapter cylinders, the axis could be adjusted to the cable reel and can be reused for STRAW-b. Besides that, no further modifications were necessary. Pictures of the winch and the wire rope are shown in the appendix A.10.

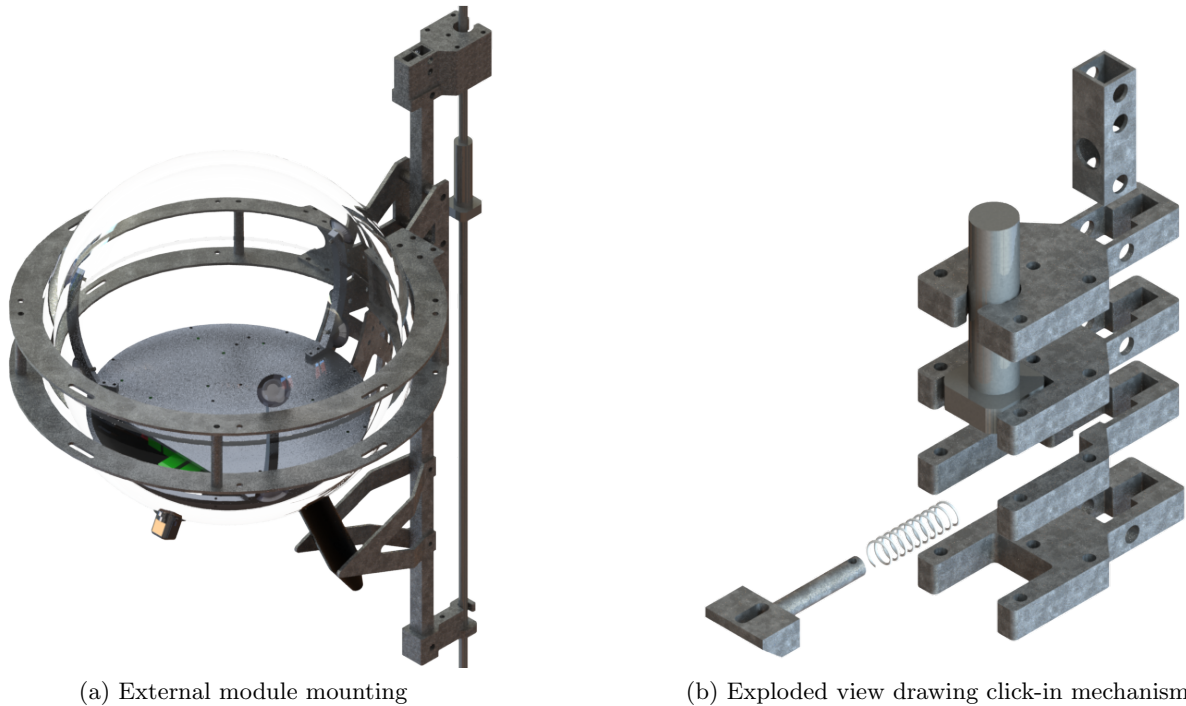


Fig. 4.5: Design of the external module mounting and a detailed exploded view drawing of the click-in mechanism. For more details refer to the text.

**External module mounting.** The external module mounting needs to fulfill several requirements. Firstly, a complement to the ferrules on the wire rope must be provided. Secondly, the glass sphere must be held firmly in place and the field-of-view in the upper hemisphere has to remain unimpeded. And lastly, the design of the external mounting needs to be lightweight as the deployment crew must be able to handle the modules. Besides that, also the aforementioned difficulties induced by the inherited dry-mate connector, due to its length, had to be considered. Several design iterations and prototypes of the module mounting were necessary to address all of those requirements. Eventually, the design depicted in figure 4.5 (a) was chosen. Most of the individual components are laser and water cut steel parts, which can be produced time and cost efficiently. The mounting principle of the sphere is based on two steel rings located 30 mm above and below the equator. By this, the sealing and adhesive tapes remain unimpaired by mechanical stress. The rings were designed with a small gap between the glass and the steel, which was ultimately filled up by an ethylene propylene diene monomer (EPDM) rubber edge protection. EPDM is a seawater resistant synthetic rubber [55]. The external mounting relies on the squeezing of the rubber band to perform enough pressure on the sphere to hold it firmly

in position. The EPDM rubber is robust enough so that the glass is protected from damage.

The other important aspect of the external mounting is the click-in mechanism for the wire rope ferrules. For this, a stack of four steel plates with a thickness of 12 mm is used, which feature different recesses to follow the shape of the ferrule. The basic design can be seen in figure 4.5 (b). By the use of a compression spring and a steel slider, similar to a doorlock, the ferrule can be clicked into the mechanism. The subcomponents of the external mounting are connected via a square profile. Here, one of the holes in the profile is used as fence for the compression spring. The square profile has a total length of 650 mm to cope with the dimensions of the glass sphere and the attached connector. However, as the sphere is offset to the steel cable, tilting of the module has to be prevented. Therefore, two small hooks are located at the lower end of the mounting. By turning the module orthogonal to the bearing steel line, they can be hooked into and the module can be turned again to lock the ferrule. As this needs to be performed on the back deck of the deployment vessel, the mounting needed to be lightweight. The overall weight of the mounting could be reduced to roughly 5 kg, by using recesses and struts rather than full metal parts. The strain on the VEOC is reduced hereby by a two-fold system: the connector attached to the sphere has a static strain relief by means of a cable clamp, whereas the remaining bunch of cables has a certain degree of freedom by the aid of a bungee cord. The maximum elongation of the bungee prevents damages on the VEOC and the connector in the case of increased strain, also once submerged. Protection plates underneath the sphere secure the connector additionally from mechanical shocks. The plates were designed in a triangular shape to ensure that the bungee cord can slip off and knots are prevented during situations where the cord is not under tension.

The design of the external mounting was largely affected by the intrinsically large buoyancy of the 13" glass sphere. Which is, calculated in kilogram, with an assumed seawater density  $\rho_{sw}$  of  $1020 \text{ kg/m}^3$  and the outer radius  $r_{out}$  of 0.1651 m

$$m_{buoyancy} = \rho_{sw} \cdot \frac{4}{3}\pi r_{out}^3 \sim 19.23 \text{ kg.} \quad (4.1)$$

The buoyancy of the sphere is effectively limited by the weight of the glass and the internal mounting. In the case of the standard module, the internal components have a weight of roughly 1.5 kg. The weight of the glass has been calculated with a density  $\rho_{glass}$  of  $2230 \text{ kg/m}^3$  and the internal radius  $r_{in}$  of 0.1531 m to

$$m_{glass} = \rho_{glass} \cdot \frac{4}{3}\pi(r_{out}^3 - r_{in}^3) \sim 8.52 \text{ kg.} \quad (4.2)$$

The volume of the external mounting is due to the laser and water cut parts relatively low ( $5.7 \cdot 10^{-4} \text{ m}^3$ ), resulting in a buoyancy of 0.6 kg. However, taking also the aforementioned weight of the mounting of 5 kg into account, the combined buoyancy of the sphere and external mounting results in 4.81 kg. This value will be even smaller for the specialized modules due to their supplements and a nearly neutral buoyancy can be expected. This implies that the upmost force on the external mounting will occur onshore, during transportation, and deployment. As

described in section 4.2.5 risk mitigation was performed in the form of vibration and shock tests for two modules. Components that could not be tested there, have been reviewed with mechanical engineers and experienced workshop employees within our institute to ensure the mechanical strength. Bolted connections have been designed according to the guidelines given in [56].

Corrosion protection for deep-sea structures has been already investigated by Andreas Gärtner in the scope of STRAW [54]. Based on the gained experience there, the steel parts for the external mounting are hot-dip galvanized. This is a procedure where steel parts are coated with a layer of zinc by submerging them in molten zinc. By doing so, cathodic protection of the steel parts is provided [57]. Furthermore, a hard zinc iron alloy forms at the interface, diminishing the risk of abrasion [58]. The coating reduces also the amount of steel exposed to seawater significantly, which would result in an ideal case to zero exposure. However, the additional zinc layer increases the thickness of the steel parts, which needs to be taken into account in their design, especially for moving parts, like it is the case for the click-in mechanism. Coating of smaller mounting components was performed by submerging them to the zinc bath while enclosed in a drum. By centrifuging the drum a surplus of zinc could be removed, reducing the risk of zinc drop formation, which would impair the click-in mechanism. For the mounting hot-dip galvanized screws are used wherever available, alternatively electro-galvanized screws.

**Buoyancy and anchor.** The buoyancy at the top of the mooring line holds the string in an upright position. For this, it must provide sufficiently large uplift and be dimensioned according to the integrated weight of the mooring line. For STRAW-b the overall weight is estimated to be around 250 kg in water, which includes the wire rope, communication cables, instruments and module mountings. Based on simulations and experiences from STRAW [54], and recommendations from our marine operations specialist Klaus Leismüller, a buoy with an uplift around twice the mooring line weight is required. For this, two spherical buoys from DeepWater Buoyancy with an individual uplift of 311 kg were chosen. These are so-called 44" Hydro-Float Mooring Buoys (*HMB-44-2500*) made of syntactic foam protected by a polyurethane cover, featuring a depth rating of 2500 m. The buoyancy is split to two buoys to provide higher flexibility for their reuse in future projects. Drag on the mooring line is reduced by the use of swivels, which allow the buoys to rotate with the current. For this, *Green Pin G-7713* swivels with a working load limit of 3.3 t are used. The anchor is provided by ONC and is usually made out of discarded train wheels. Unlike as for STRAW, it is not required to have a rotatable anchor. For the anchor weight the double of the buoyancy is anticipated, which in our case is around 1200 kg. This ensures a stable position of the entire mooring line. The recovering of the mooring line is enabled by the use of a so-called ROV release. Here, the ROV can detach the mooring from the anchor by triggering the mechanical release and the buoyant force brings the string back to the surface. A technical drawing of STRAW-b with the positions of the modules and all the components mentioned is depicted in figure 4.6.

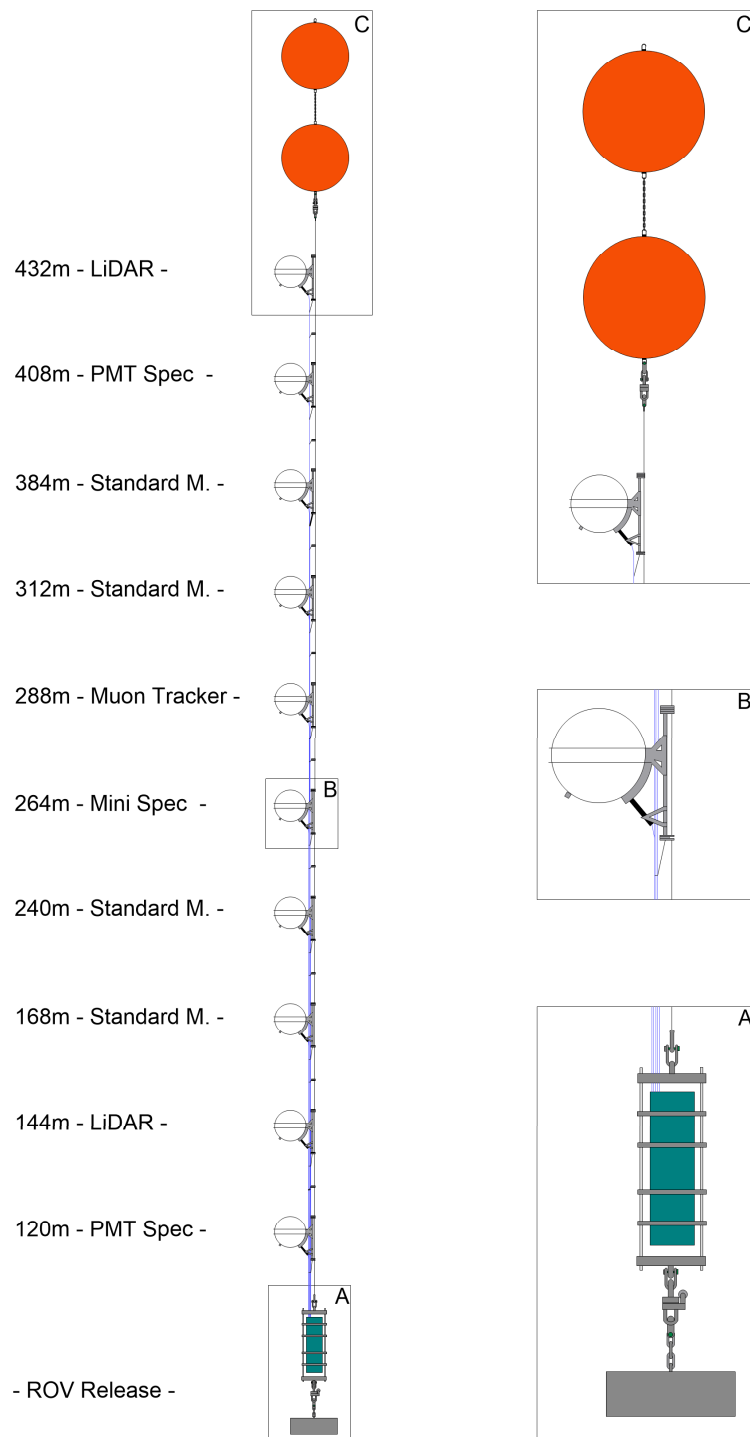


Fig. 4.6: Technical drawing of the STRAW-b mooring line. Details about the subcomponents and the modules are provided in the text.

#### 4.2.4 The instrument tray for the STRAW-b deployment

The instrument tray hosts the modules, the communication cables, and the mini junction box during the deployment. The tray must therefore fulfill several requirements. Firstly, it must bear the weight of ten modules including their mounting, the VEOC, the MJB, and also its own weight. Estimated numbers can be taken from table 2. For every aspect, a safety factor has been introduced. Secondly, it must be large enough to host the VEOC and, as well, provide easy access during the deployment. To avoid torsion and prevent knots, the hybrid cable had to be spooled in an eight. Hereby also the minimum bending radius of the VEOC had to be taken into account, which is, for dynamic bending, approximated with 125 mm. For this reason, in total six PVC-pipes as cable guides are used.

Component	Weight [kg]	Comment
<i>VEOC</i>	250	<i>According to data sheet (55 kg/m in air)</i>
<i>Modules</i>	300	<i>Includes overestimation for every module</i>
<i>MJB</i>	100	<i>Number provided by ONC</i>
<i>PVC pipes</i>	6x20	<i>Estimated value from CAD program</i>

Tab. 2: Estimated weights for the different components hosted on the tray. Every aspect includes a safety factor. The weight of the VEOC has been calculated for the full number of available cables instead for the ten used ones. Also for the modules 30 kg were used, although the weight of a single module should not exceed 20 kg, to ensure safe handling on the back deck. Likewise the weight of the MJB was assigned with a safety factor.

Each side of the instrument tray should store five modules, while the spacing between the VEOC ends is around 24 m. A trade-off had to be found between the amount of cable stored on one loop and the overall dimensions of the tray, especially the depth. Respecting this, a loop with a length of 8 m was considered suitable, which would require to distribute a total of 4 m slack in between two modules to ensure the right distribution of those. Thus, for the total length of 432 m, 54 loops are necessary. Considering a bunch of 10 cables, where each individual cable has a diameter of 7 mm, and assuming that the bunch diameter is determined by roughly four VEOCs, a bar length  $l$  of around 1.5 m is necessary. Contemplating that the VEOC, as well as the ten modules, have to be stored on at least two semi-detached bars to allow the uncoiling on the back deck and to store them in an eight, a structure capable of bearing the integrated weight had to be found. According to this the maximum allowed bending stress for a given material cannot be exceeded and must be calculated via the following assumptions [59, p. 181].

The VEOCs and the modules will be carried by different bars. Thus for the calculation of the bending stress of the rod only the weight of the VEOC and the PVC-pipes has to be considered. The distributed load of them is treated as constant

$$q(x) = q_0 \quad \left( \text{with around } 250 \frac{\text{kg}}{\text{m}} \right). \quad (4.3)$$

The transverse stress is given by

$$\frac{dQ}{dx} = -q \quad (4.4)$$

which can be integrated by using  $q_0$  to

$$Q(x) = -q_0x + c_1. \quad (4.5)$$

The bending moment can then be obtained by

$$\frac{dM}{dx} = Q \quad (4.6)$$

and thus

$$M(x) = -\frac{1}{2}q_0x^2 + c_1x + c_2. \quad (4.7)$$

Boundary conditions for a semi-detached rod are

$$Q(l) = 0 \quad \wedge \quad M(l) = 0 \quad (4.8)$$

and can be used to calculate the integration constants. By doing so, the bending momentum finally amounts to

$$M(x) = -\frac{1}{2}q_0l^2 \left(1 - \frac{x}{l}\right)^2. \quad (4.9)$$

The maximum lies at  $x = 0$ , which delivers a maximum bending momentum of roughly 300 Nm. This value must be used to calculate the maximum bending stress via

$$\sigma = \frac{M}{W} \quad (4.10)$$

with  $W$  as the moment of resistance [60]. This is tabulated for various materials but can also be calculated if the second moment inertia is known. As aluminum profiles were considered as building materials very early in the process,  $W$  could be obtained from their data sheets. For the chosen profiles the moment of resistance is  $46.92 \text{ cm}^3$  [61]. Hence a bending stress of  $6.4 \text{ N/mm}^2$  is obtained. This must be compared to the maximum allowed bending stress for a given material, which in the case of aluminum is

$$\sigma_{allowed} = \frac{195}{s} \frac{\text{N}}{\text{mm}^2}, \quad (4.11)$$

where  $s$  denotes the safety factor [60]. The selected aluminum profiles are therefore suitable as building materials. In the next step the bearing reactions can be calculated via the obtained formulas for the bending momentum and the transverse stress to define the joints. For this, the values at the joint position A ( $x=0$ ) are necessary.

$$Q(0) = q_0 l \approx 3750 \text{ N} \qquad M_A(0) = -\frac{1}{2} q_0 l^2 \approx -2812.5 \text{ Nm} \quad (4.12)$$

These loads must be distributed on several brackets and rods, as especially the momentum is too much for a single joint of most available types. For the instrument tray, twelve large aluminum brackets were incorporated to hold the structure in an horizontal position. Each one of them can take a maximum load of up to 8000 N and a momentum of 800 Nm. Supplementary security is provided by the usage of fishplates on the top four rods and two additional diagonal bars. The design of the tray can be seen in figure 4.7. The combined weight of the hybrid cables and the cable guides is distributed over the four top rods and additionally supported by the four lower bars. For the mounting of the modules smaller bars were chosen. The load on one bar itself comes from a maximum of three modules, while each has a mass of 300 N. As the beams are clamped on both sides the load distribution is equal on every bearing (A, B), and thus need to take up individually

$$A = B = \frac{3}{2} F_M \approx 450 \text{ N}. \quad (4.13)$$

On that account brackets with an individual maximum uptake of 1000 N and 50 Nm were chosen. As the beams are clamped on both sides the momentum on the brackets is considered negligible. Although the load is now partly integrated within the cable rods, the safety factor given by the number of used brackets to account for the values given by equation 4.12 is sufficient. This can be shown by a recalculation with an adjusted  $q_1$  of 450 kg/m.

$$Q(0) = q_1 l \approx 6750 \text{ N} \qquad M_A(0) = -\frac{1}{2} q_1 l^2 \approx -5062.5 \text{ Nm} \quad (4.14)$$

The discussed mounting structure for the VEOC and the modules is mounted on an underlying frame of aluminum profiles. The horizontal structure, bearing the weight of the VEOCs, modules, and PVC pipes, poses hereby a large momentum on the profile underneath and causes a twist angle, which can be calculated via

$$\vartheta = \frac{M_{total} \cdot l_{profile}}{4\pi \cdot G \cdot I_t} \cdot 180^\circ \quad (4.15)$$

with  $G$  as shear modulus,  $I_t$  as torsional moment and the length of the profile beneath the guiding structure  $l_{profile}$  [60]. The missing material values are tabulated for the used aluminum profiles. The total momentum is given by

$$M_{total} = (M_{VEOC} + M_{modules} + M_{pipes}) \cdot l_{height} \quad (4.16)$$

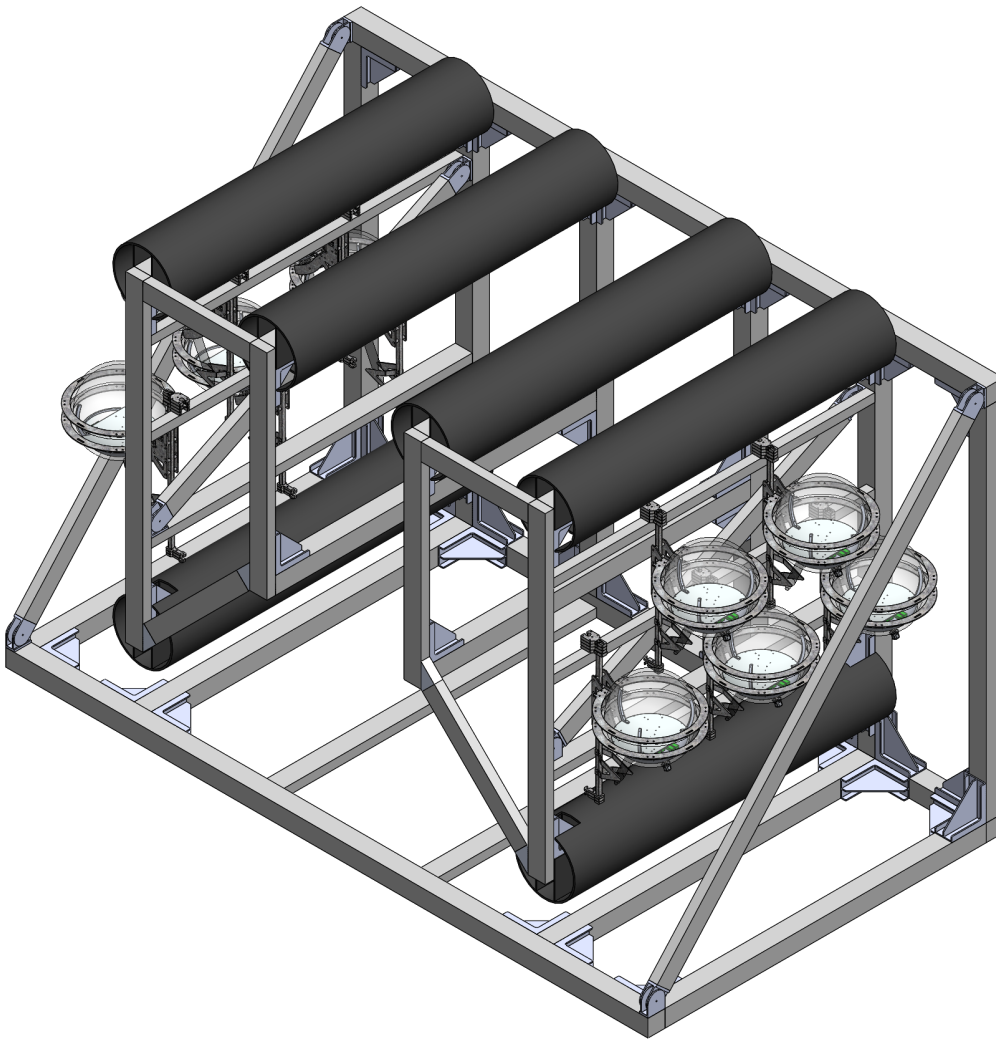


Fig. 4.7: Sketch of the instrument tray with attached modules. The aluminum profiles are depicted by the gray bars. To avoid contact corrosion between the hot dip galvanized module mountings and the anodized aluminum, intermediate protective plates made from PVC are integrated.

and accounts to roughly 12000 Nm. This causes a twist angle of  $16.1^\circ$ . To mitigate this, four rods as strutting were integrated and additionally two diagonal bars, with joints capable of an uptake of 10000 N. Regardless of that, the bending stress of the underlying bar was shortly cross checked with an available construction tool of the aluminum profile manufacturer item Industrietechnik GmbH [61], where approximations had to be made regarding the load distribution. Hereby, the load was assumed to act on the middle of a beam with a length of 3 m, which is clamped on both sides. To account for dynamic stress peaks and the additional weight by the aluminum profiles the load was assumed to be 2000 kg. In that case the bending

amplitude is 9.13 mm and the bending stress 31.97 N/mm<sup>2</sup>, which is still comfortably within the allowed bending stress stated in equation 4.11. Additional transport and crane lifting security is achieved by the use of supplementary bars at the front of the instrument tray as can be seen in figure A.9.

The mini junction box will be stored beneath the cables, therefore a base plate will be mounted on the tray. As this is tailored to the MJB it will be mounted on site at the Marine Technology Center (MTC), to incorporate also possible late changes in the design.

#### 4.2.5 Qualification of the module mechanics

Risk mitigation for the STRAW-b modules has been performed in the form of several tests. Hereby, environmental resistances required for the deep-sea and stress during the deployment could be addressed. In this section, an overview of the performed tests within our university shall be given. The section will be concluded with a concise outlook to additional tests, which will be carried out at the MTC.

**Vibration and shock test.** Drag, induced by seawater currents and the descend velocity during deployment, can cause vibrations in the instruments, bearing the potential to harm electronics as well as mechanics. Besides, vibrations and shocks can also occur during transportation and general handling of the equipment. On that score vibration and shock tests according to the ISO 13628-6 standard were performed for a standard module as well as a prototype of the PMT spectrometer module. The test foresees for each spatial axis a sine vibration with an amplitude of 2 mm for the frequency range 5-25 mm, and afterward 5 g between 25-150 Hz. Shocks with an acceleration of 10 g are performed eight times per direction. Besides that, resonance searches within the tested frequency range of 5-150 Hz before and after the actual tests are carried out. Both modules were tested with the external mounting, however, the square rod and the click-in mechanism had to be replaced by an adapter for the test table, as can be seen in figure A.11 and A.12. The test has been passed by both instruments, also the included readout electronics survived. The only observable issue was the unfastening of four screws at the interface of the readout electronics to the internal mounting plate in one module. However, the test has been finished without these screws. Compensation of this flaw will be performed by means of longer screws and additional use of screwlock in the final design.

**Pressure test.** The pressure in the deep-sea must be handled by the submerged instruments. For the Cascadia Basin in a depth of 2600 m a pressure of 260 bar is expected. The utilized glass spheres are intrinsically already pressure rated, however, by adding specific holes e.g. for bulkhead connectors, their behavior can be altered. For this reason, a separate pressure test for one module assembly was performed. The housing manufacturer Nautilus provides therefor a specific pressure chamber. Here, the instrument is repeatedly cycled to a maximum pressure of 375 bar before holding the pressure for several minutes. For the pressure test, the same module assembly was used as for the vibration and shock tests. The module successfully passed the test, albeit, small detachments of the optical gel to the aluminum bowl could be observed. However, they quickly disappeared by reducing the underpressure in the module and are considered to

be not relevant for the instrument behavior. Pictures of the pressure test are shown in the appendix A.16.

**Durability test.** Between the end of December 2019 and the end of January 2020, a long-term test of a STRAW-b module has been performed. For this, it was submerged in a test-pool while pressure, temperature, and humidity were monitored. The pool was filled with artificial seawater, created by use of *Instant Ocean*, to investigate possible effects on the sealing of the module and the connector. During the overall test period load resistances were used to simulate a working module. The test results are shown in figure 4.8. Despite the jump between the 8th and 11th January, the temperature remains stable except for smaller deviations. The jump in temperature is caused by the ongoing heating of the test room after the Christmas break. Correlated to the increased temperature the pressure also increases. Besides that, the internal pressure remains rather stable at around 275 mbar. The constant decrease in humidity is most likely caused by condensing as the module was not nitrogen flushed.

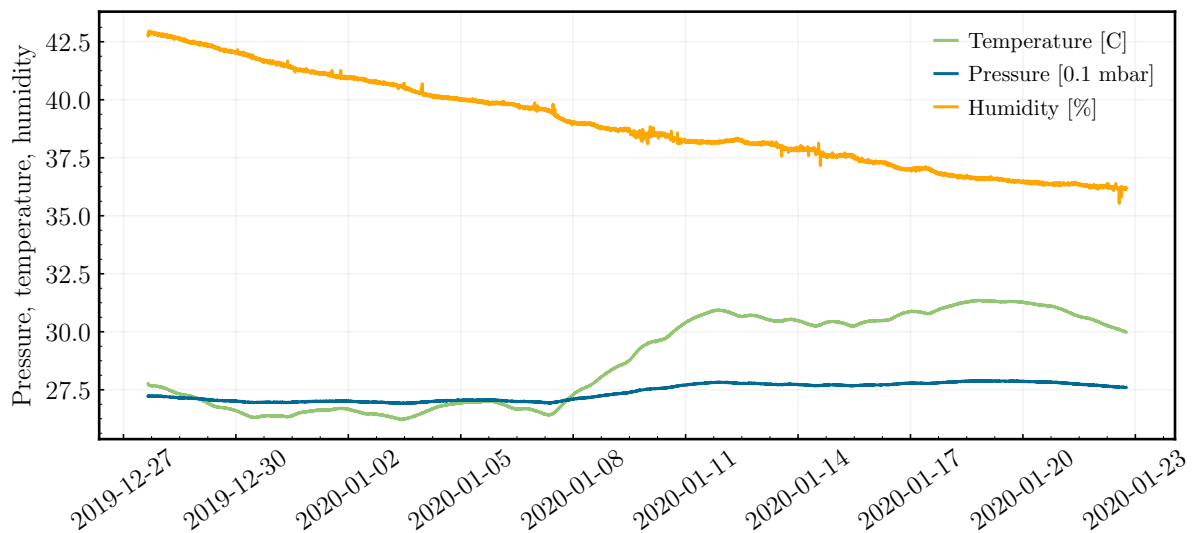


Fig. 4.8: Internal pressure, temperature, and humidity values during the time of the test period. The jump after the 8th of January is caused by the heating of the test room after the Christmas break.

During the commissioning phase at the MTC additional extensive underwater tests are foreseen. The instruments will be tested separately in a saltwater test tank to check for ground faults. Once the instruments have passed, the integrated mooring line will be tested with the connected MJB in a dedicated seawater test pool over the course of several days.



## 5 P-ONE mooring line design study

P-ONE, as new neutrino telescope, aims to complement the working effort of the existing and currently under construction neutrino telescopes. As such, one of the main design requirements is the instrumentation of a large volume with photosensors. P-ONE will follow thereby a clustered structure to remain accessible by ROV operations for deployment, connection, and recovery of moorings lines. Coverage of large volumes can then be achieved by long mooring lines and the expansion of clusters over a large seafloor area. Simulations and design studies for the clusters are currently ongoing and will not be further subjected within this section. However, based on the experiences with the previously discussed pathfinder missions, a design study for a future P-ONE mooring line can be performed.

Currently, a mooring line length between 750 and 1000 m with a total of 20 instruments is foreseen for P-ONE. The P-ONE calibration module (P-CAL) is a POCAM adapted to the P-ONE interface, as discussed in section 3. The P-ONE digital optical modules (P-DOM) will be developed on the base of the standard module, discussed in section 4.2.1. As photosensors around 12 PMTs are planned. For both instruments, an unimpeded field-of-view is inevitable and must be considered in the design of the mooring. The utilization of tightly fitting mooring frames for the P-DOM could be a suitable option. The glass sphere would be enclosed and protected by the frame, and by designing them alongside the optical modules an impairment of the photosensors can be excluded. Furthermore, mooring frames are a commonly used tool in marine operations, which makes them a familiar tool for marine operators, widely available and cost efficient. The protection of the glass module can be performed by the aid of EPDM edge protections or by coating the entire frame with polyvinyl chloride (PVC), with a suitable shore hardness. The latter has been already performed with good experience for prototypes of the STRAW-b external mounting, however, it was eventually disregarded due to time constraints. Additionally, reflections can be avoided by coating the frame with black PVC. Mounting the P-CAL in a horizontal position along the mooring line circumvents cable shadows. Therefor also mooring frames attached to the titanium cylinder of the calibration module can be used. Titanium might be also favorable as material for the external mechanical parts, as it provides high resistance against corrosion [57]. Also, unlike it is often the case for hot-dip galvanized parts due to clogged drill holes and zinc drop formation, no dedicated post-processing is required for titanium.

Optical fibers are inevitable for sufficient data transmission over large distances and will be an important factor for P-ONE. However, the separation of the bearing steel line and the communication cable extends expensive offshore operations and adds additional complexity. A combined backbone in the form of a bearing hybrid electro-optical cable can reduce the deployment and handling effort. This concept already exists in the form of steel ropes molded within the cable, which take up the load. This was suggested from ConceptCables. However, this would make the cable relatively stiff and heavy, which makes storage on a tray difficult. Alternatively, also synthetic fibers can be used to take up the load. Offers for bearing cables of this sort are currently collected. In terms of deployment, a combined backbone would cut costs for winches and wire ropes, as the modules can be deployed directly from the tray. Power to

the modules is provided by means of copper cables. To deal with power losses along the copper wires a separation in two blocks of respectively 10 modules, by an intermediate mini junction box could be performed. This makes also a separation of the mooring line to two instrument trays possible, which reduces their dimensions. Here, essentially the design given in section 4.2.4 might be already sufficient. Possible twisting of the modules can be mitigated by the use of short steel cables, which grab the underlying backbone, forming a triangular structure. By this, the load can be taken away from the backbone and the necessary slack for connections and the guidance of the backbone around the module can be provided. An overall technical design of the mooring line, based on the abovementioned structure, is depicted in figure 5.1.

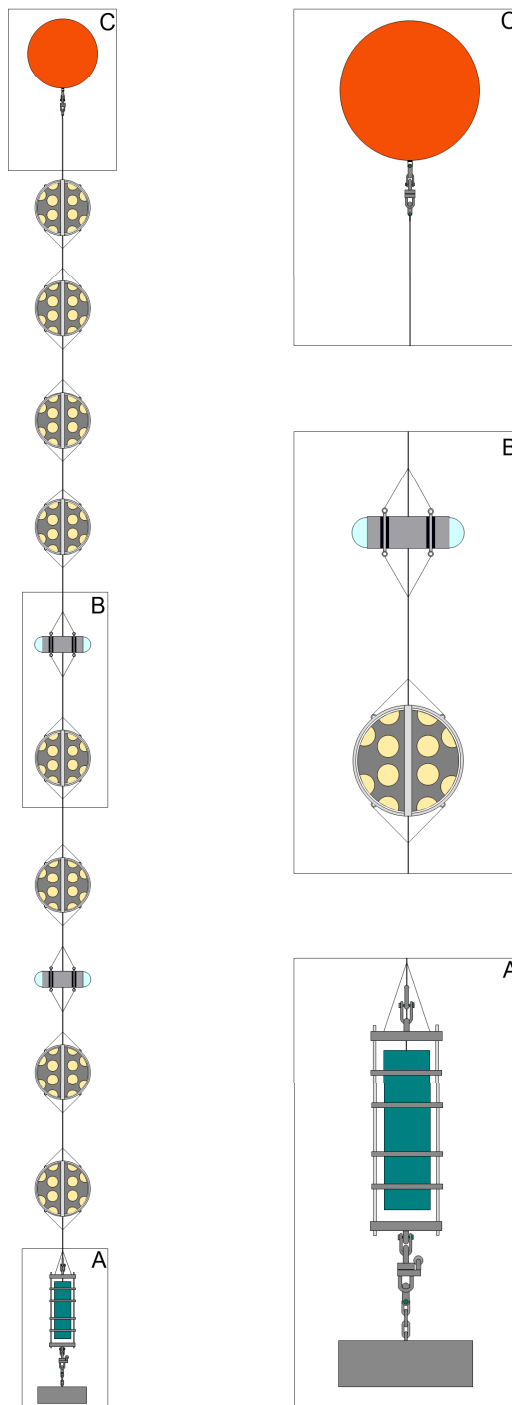


Fig. 5.1: Concept drawing of a future P-ONE mooring line. The mounting of the modules is performed by means of mooring frames. For a final mooring line 20 modules are foreseen, however, only eight are depicted here. For more details refer to the text.



## 6 Conclusion and outlook

The deep-sea infrastructure provided by ONC poses a framework invaluable for P-ONE. Preliminary results of the attenuation length by the measurements of STRAW classify the Cascadia Basin already as a suitable site for a neutrino telescope. Further analysis of the obtained data and the second pathfinder mission aim to verify and extend these results. STRAW-b has been developed in the scope of this master thesis over the past year and is in a very advanced stage. The deployment that was initially planned for June 2020, however, had to be postponed due to the COVID-19 pandemic of spring 2020. Now, a deployment in September 2020 is envisaged but depends heavily on the further development of the pandemic. The design of the P-ONE mooring lines is based on the experiences of both pathfinders, a successful deployment and operation of STRAW-b would qualify the developed methods further. The readout concept and the design of the standard module as well as the new iteration of the POCAM will serve as the foundation for the P-ONE optical modules. For the POCAM, the internal construction, pulse drivers, and photosensor readouts have been revised for the IceCube Upgrade. The isotropic light emission and the dynamic range of the pulse drivers could be thus even further improved.

P-ONE as a cubic kilometer detector in the Pacific Ocean has the potential to greatly improve the exposure of the neutrino sky. New impulses to multi-messenger astronomy can be given by a network of neutrino telescopes, consisting of P-ONE, KM3NeT, and GVD in the northern hemisphere, and IceCube in the southern hemisphere, in the form of a planetary neutrino monitoring system (PLE $\nu$ M) [47].



## A Appendix

### A.1 POCAM



Fig. A.1: Picture of the POCAM after cooling it down to  $-80^{\circ}\text{C}$ . The formation of ice crystals on the surface started immediately after exposing it to room temperature.

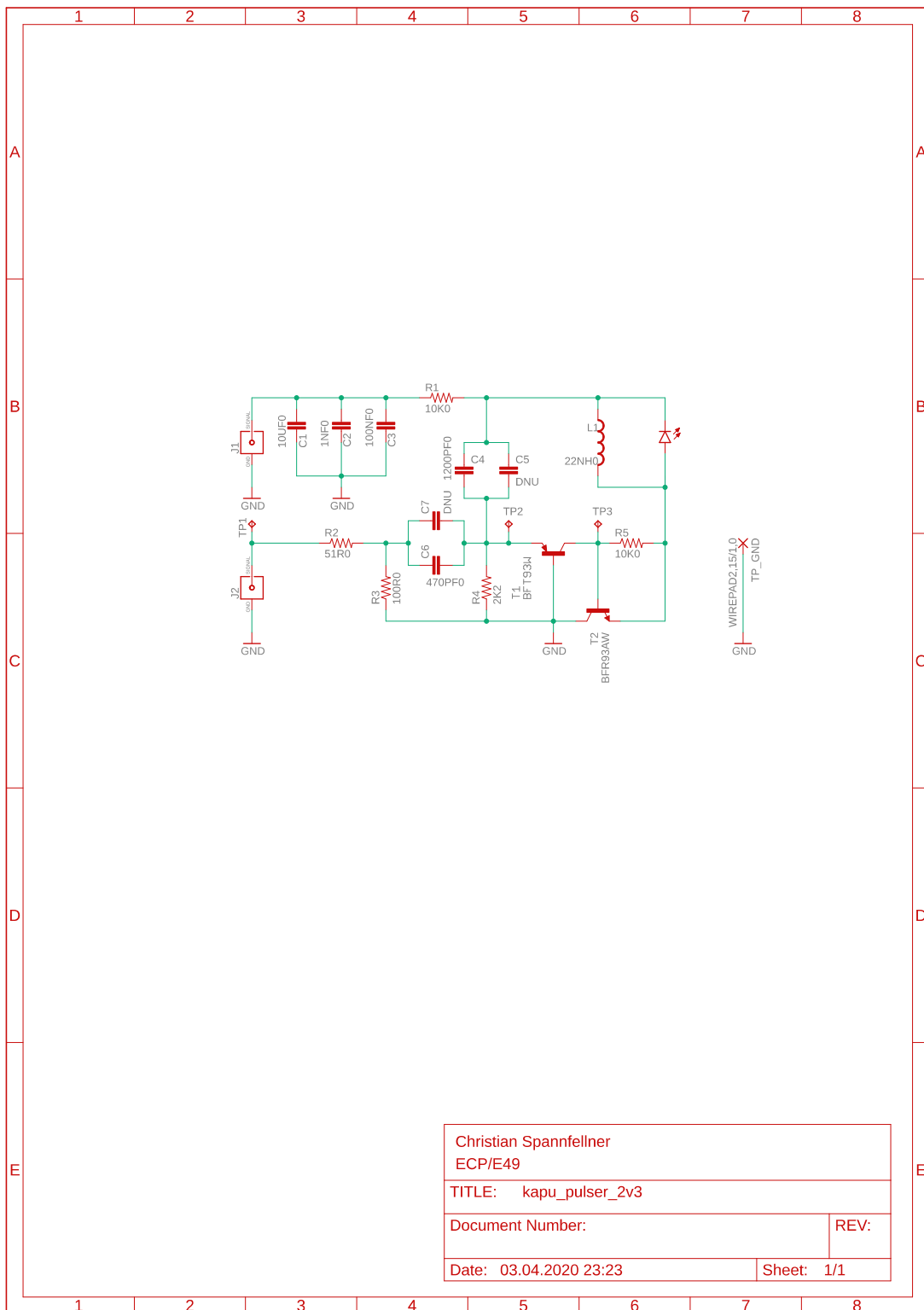


Fig. A.2: Kapustinsky pulse driver schematic.

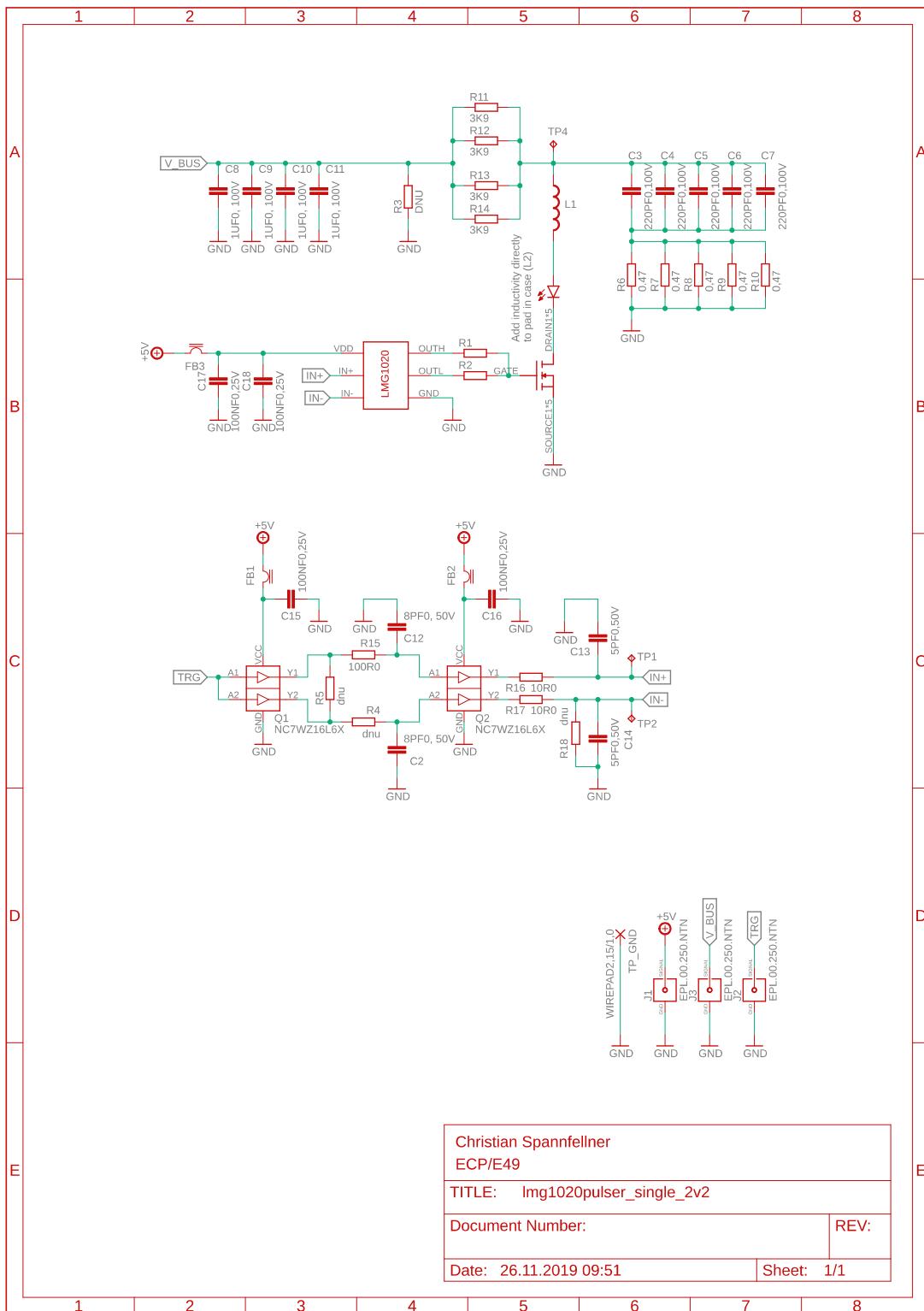


Fig. A.3: LiDAR-type pulse driver schematic. L1 was added for testing purposes but eventually replaced by a jumper.

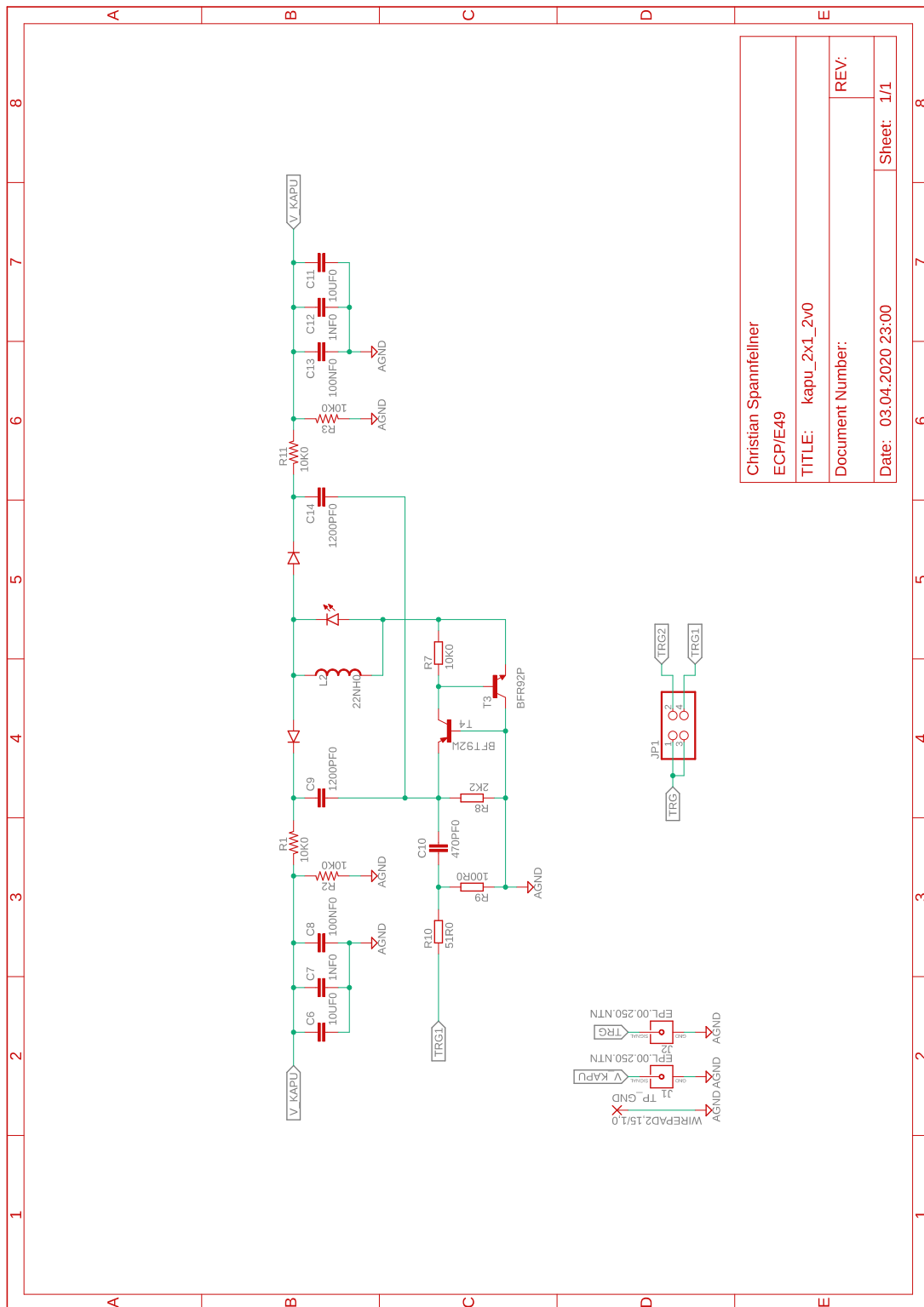


Fig. A.4: Schematic of the redundancy modifications for the Kapustinsky pulse driver.

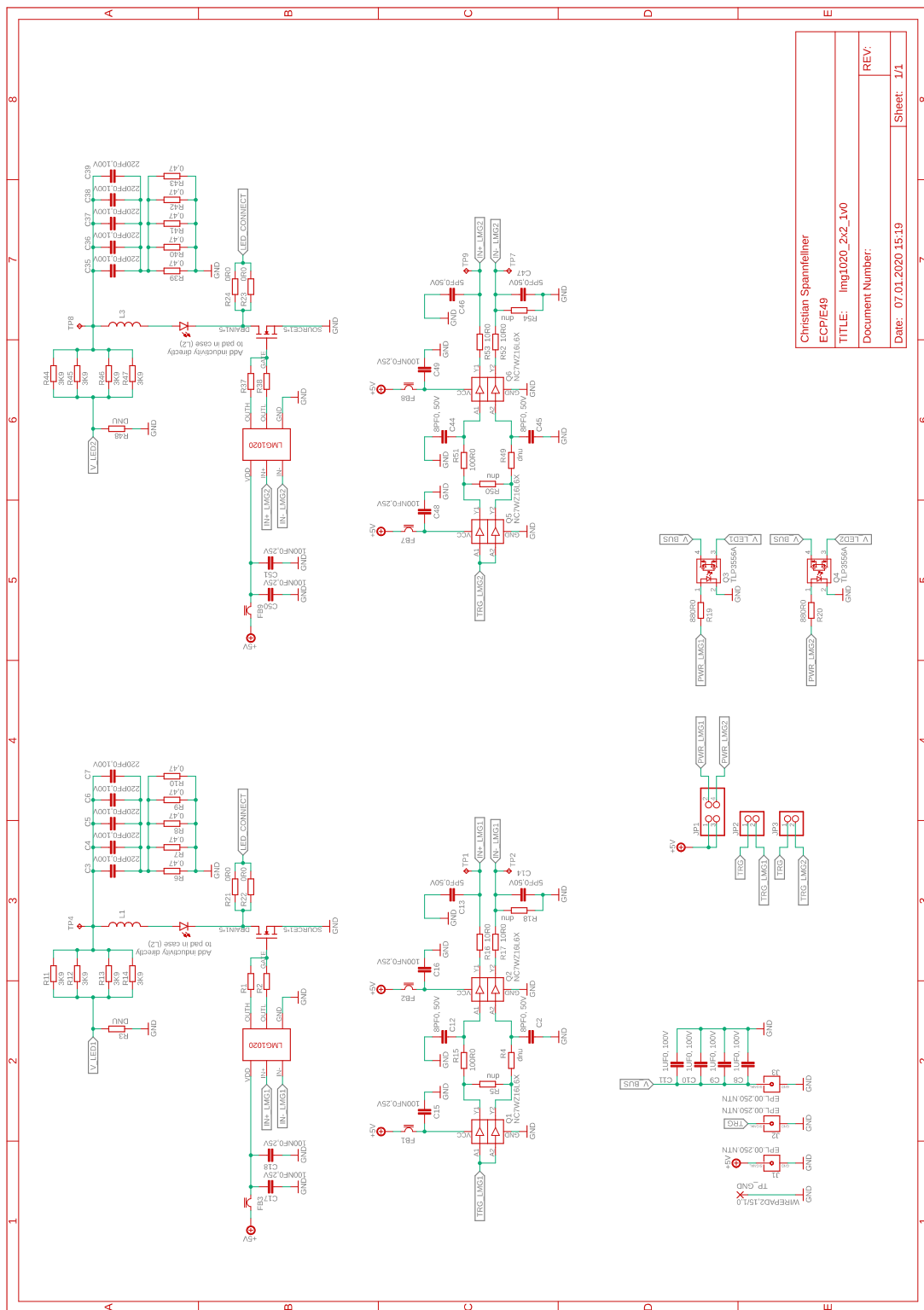


Fig. A.5: Schematic of the test board for the redundancy modifications of the LiDAR-type flashing circuit.

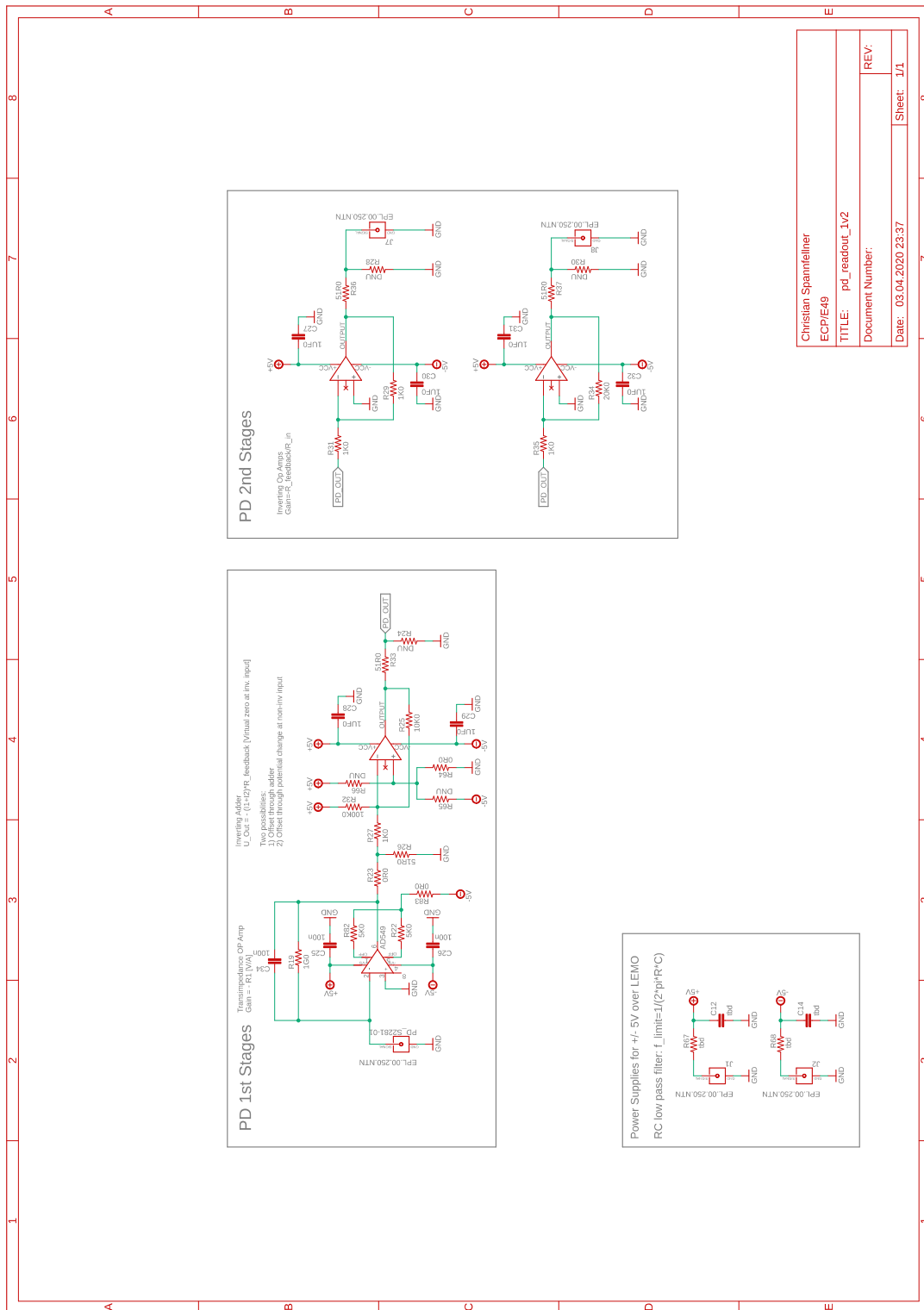


Fig. A.6: POCAM photodiode readout schematic.

## A.2 STRAW



Fig. A.7: The VEOC was delivered in a bunch of fourteen cables. For testing and handling, the individual hybrid cables were separated on single spools. This operation was performed in the main corridor of the engineering department, where the cables could be stretched out over a large distance to handle their internal strain and twists. Pictures taken by Kilian Holzapfel.



Fig. A.8: The hybrid cables foreseen for the deployment of STRAW-b have been bundled again and wound up on the instrument tray. This was performed in a hallway of the physics department, where the floor was marked every 12 m. At these markings, the bungee cords and respective position marks were attached. Upper picture taken by Elisa Resconi.

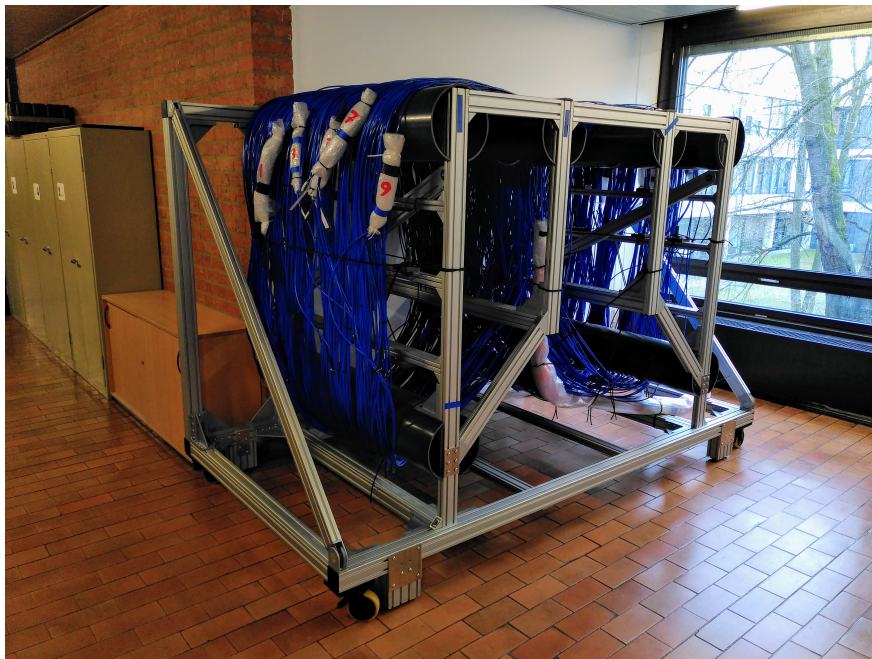


Fig. A.9: Pictures of the instrument tray before shipment. The connectors are aligned on the left and right side, marked with the later positions, and packed in bubble wrap. Additional bars are attached as transportation and lifting security.

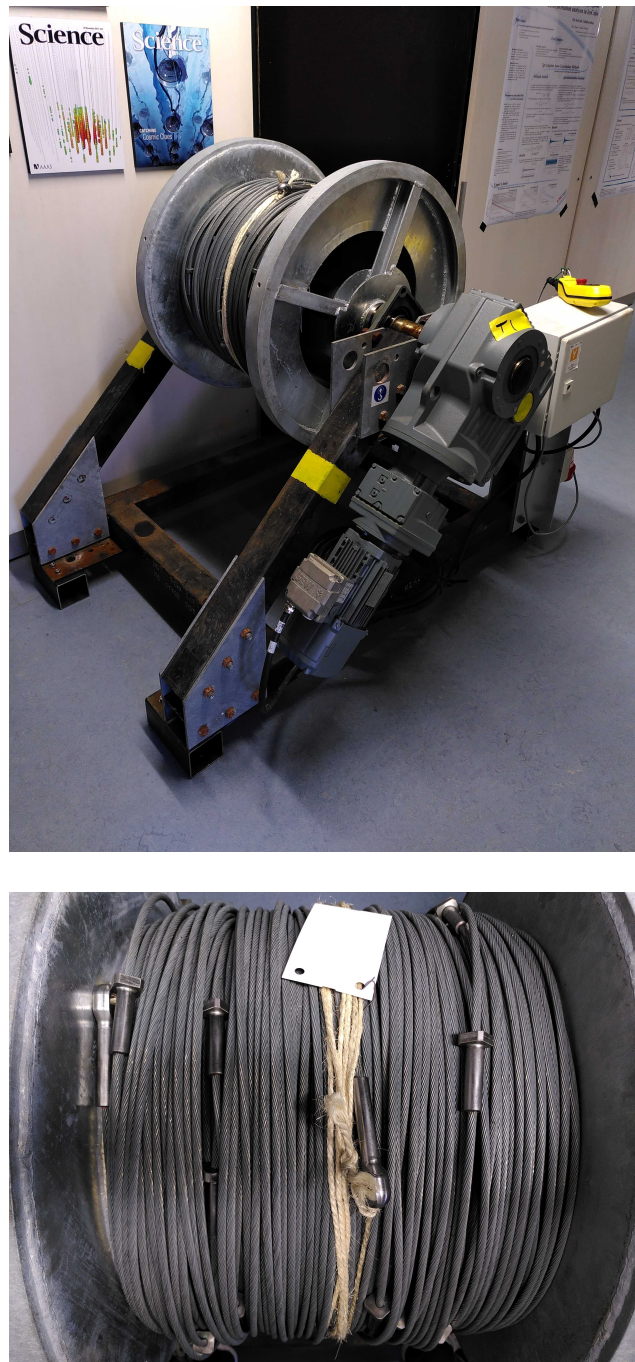
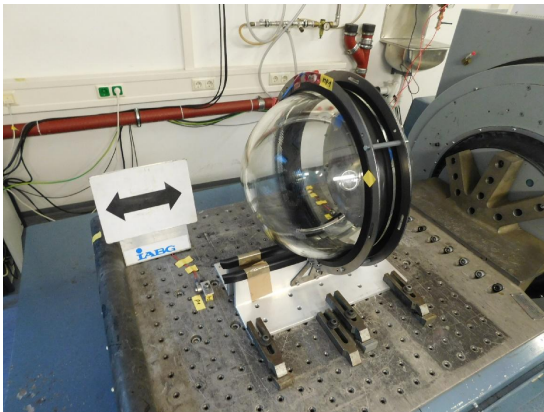
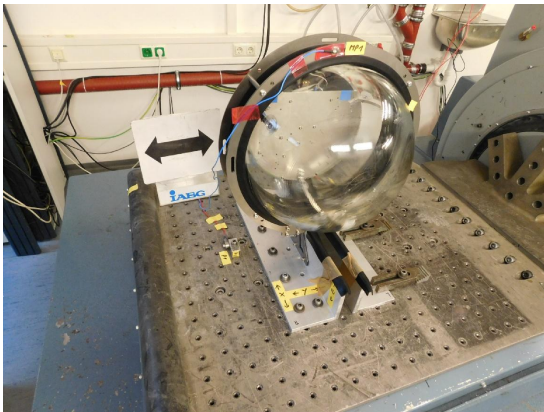


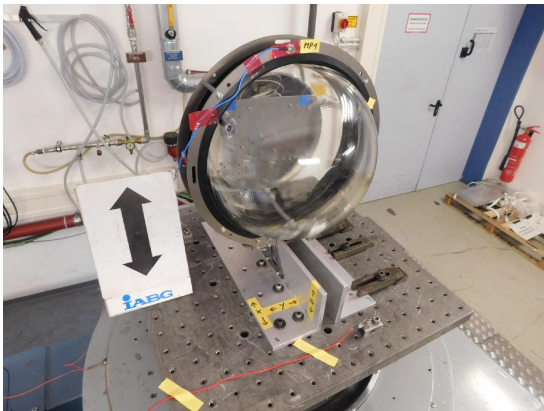
Fig. A.10: Picture of the winch, which was constructed for STRAW and will be reused for STRAW-b. The cable reel with the wire rope for STRAW-b is already mounted. The lower picture is a close-up view of the wire rope and the attached ferrules.



(a) X-axis

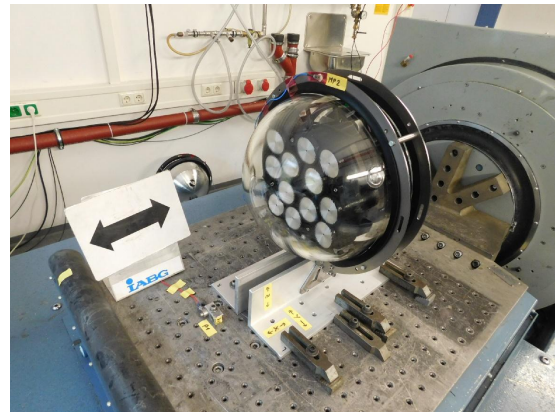


(b) Y-axis



(c) Z-axis

Fig. A.11: Vibration and shock test axes of the standard module.



(a) X-axis



(b) Y-axis



(c) Z-axis

Fig. A.12: Vibration and shock test axes of the PMT spectrometer.

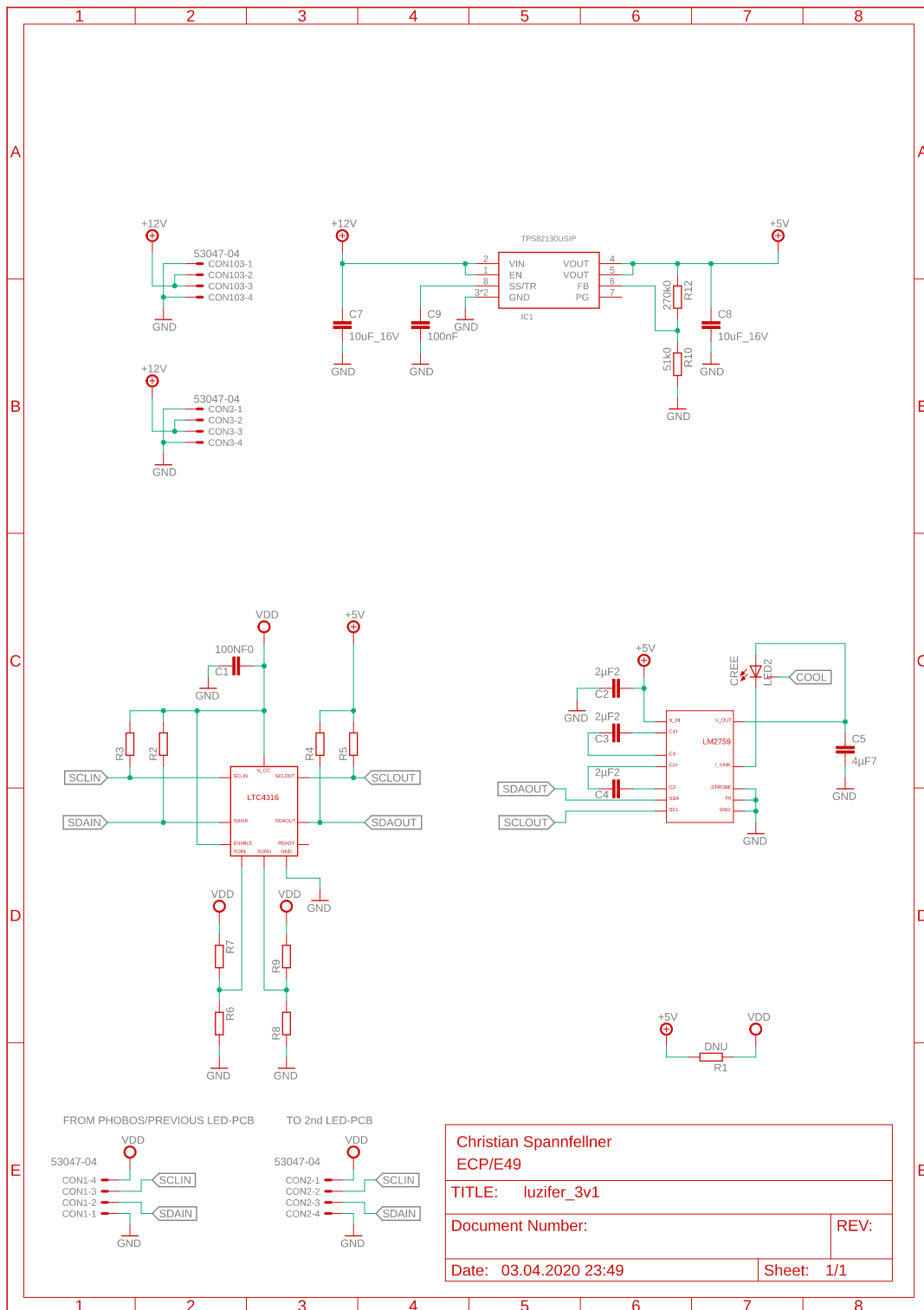


Fig. A.13: Schematic of the LED flasher circuit for the STRAW-b modules, called Luzifer.

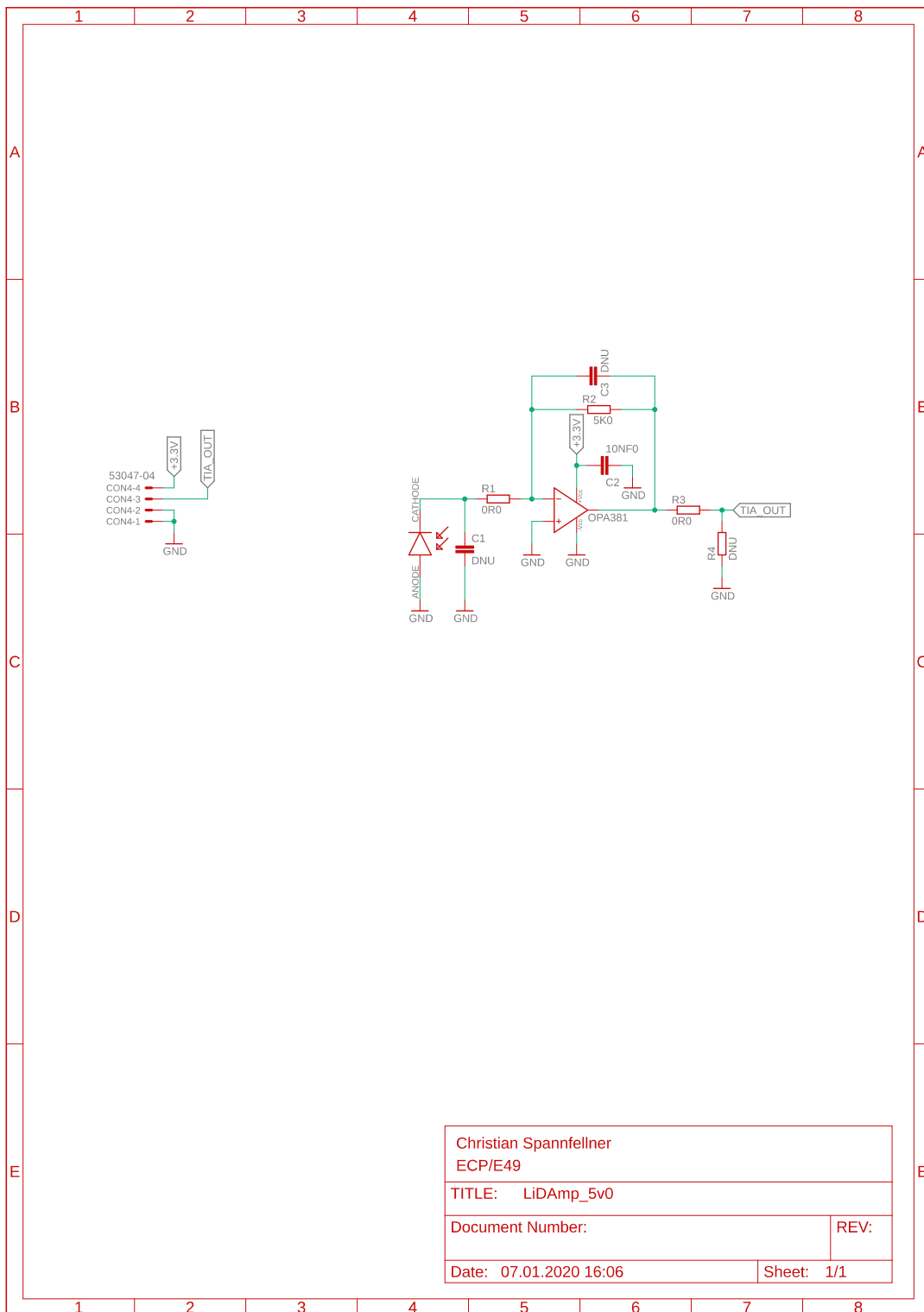


Fig. A.14: Transimpedance amplifier schematic of the LiDAR module.

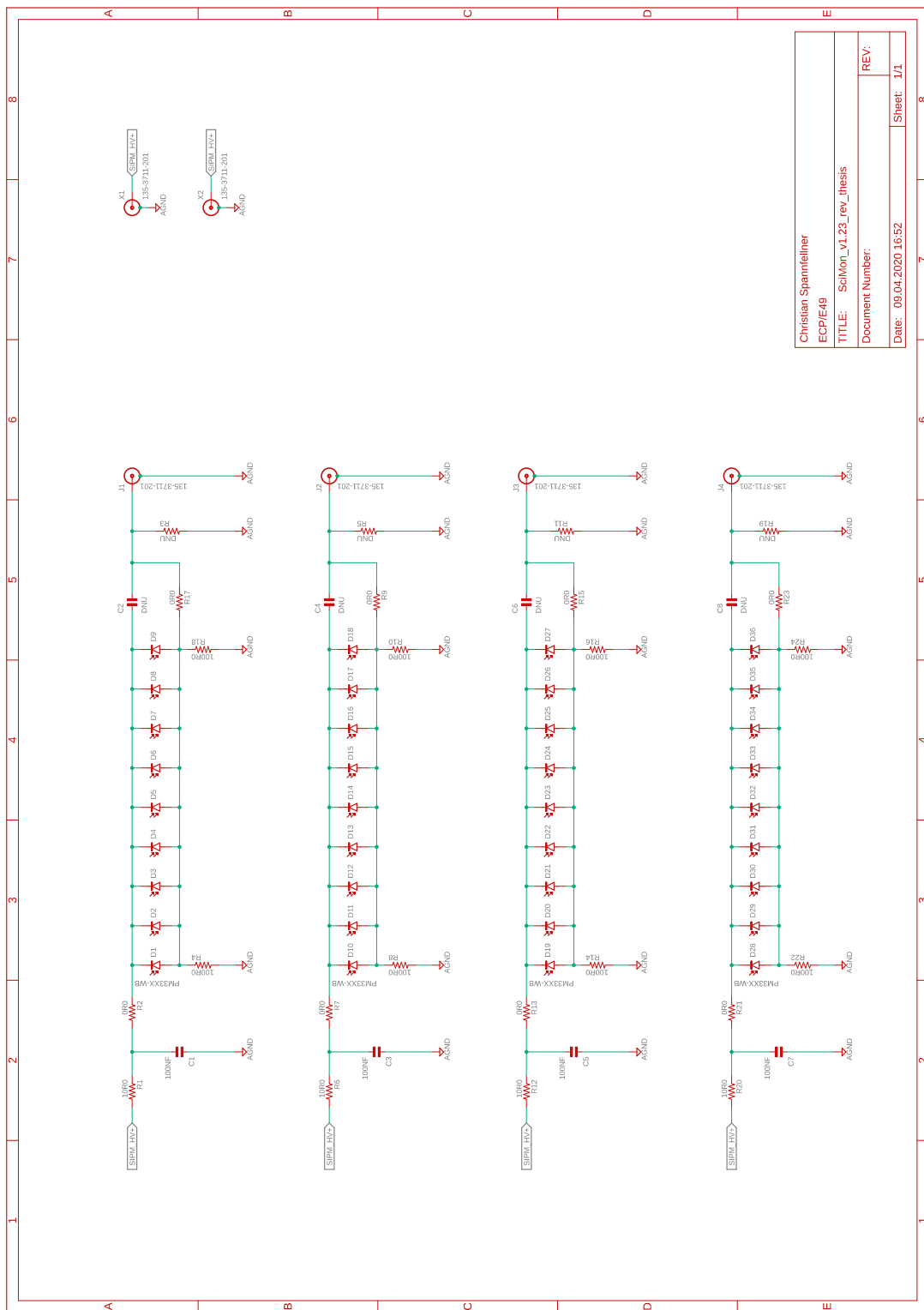


Fig. A.15: Schematic of the SiPM matrices. Four of those PCBs are used in the STRAW-b muon tracker module.



Fig. A.16: Pictures of the standard module assembly after the pressure test. The lower picture shows the gel detachments.



## Acknowledgments

First I would like to thank my supervising professor Elisa Resconi for giving me the opportunity to work in experiments on the frontier of astroparticle physics. It is thanks to her, and the group behind her, that these projects were able to go on successfully. Furthermore, I want to thank her for allowing me to participate in various conferences to meet, and work with, great scientists and experienced engineers.

Evenly, I want to express my gratitude to Felix Henningsen, Christian Fruck, and Andreas Gärtner for their, technically, shared supervision. It is a pleasure to work with you guys and to share countless hours of discussions, night shifts, and coffee breaks. Furthermore I want to thank of course the rest of the pathfinder group: M. Böhmer, L. Geilen, R. Gernhäuser, K. Holzapfel, Na. Khera, Ni. Khera, K. Leismüller, L. Papp, I.C. Rea, L. Ruohan, F. Schmuckermeier, D. Vivolo, and E. Winter. Without your patience, endurance, dedication, and professionalism none of these projects would be possible.

Finally, I would like to express especial gratitude to my family and friends for their support, patience, and distraction during the time-expensive physics studies. Thank you!



**List of abbreviations**

<b>ADC</b> analog-to-digital converter .....	36
<b>AGN</b> active galactic nuclei .....	5
<b>APD</b> avalanche photodiode .....	29
<b>CC</b> charged current .....	9
<b>CMB</b> cosmic microwave background .....	4
<b>DAC</b> digital-to-analog converters .....	46
<b>DAQ</b> data acquisition .....	22
<b>DOMs</b> digital optical modules .....	16
<b>EPDM</b> ethylene propylene diene monomer .....	52
<b>FPGA</b> field programmable gate array .....	24
<b>GaN-FET</b> gallium nitride field effect transistor .....	30
<b>GRB</b> gamma ray bursts .....	5
<b>GVD</b> Gigaton Volume Detector .....	17
<b>IACT</b> Imaging Air Cherenkov Telescopes .....	7
<b>ICM</b> IceCube communications module .....	25
<b>ICU</b> IceCube Upgrade .....	17
<b>JB</b> junction box .....	43

---

<b>LD</b> laser diode .....	30
<b>LED</b> light emitting diode .....	21
<b>LIGO</b> Laser Interferometer Gravitational-Wave Observatory.....	8
<b>MBL</b> minimum breaking load.....	51
<b>MCU</b> micro-controller unit .....	25
<b>Mini-MB</b> mini mainboard.....	25
<b>MJB</b> mini junction box .....	43
<b>MTC</b> Marine Technology Center.....	60
<b>NC</b> neutral current.....	9
<b>NEPTUNE</b> North East Pacific Time-series Underwater Networked Experiments.....	18
<b>OMs</b> optical modules .....	17
<b>ONC</b> Ocean Networks Canada.....	18
<b>P-CAL</b> P-ONE calibration module.....	63
<b>PCB</b> printed circuit board .....	21
<b>PD</b> photodiode .....	29
<b>P-DOM</b> P-ONE digital optical modules.....	63
<b>PKMS</b> Pontecorvo-Maki-Nakagawa-Sakata.....	10

<b>PMT</b> photo multiplier tube .....	16
<b>POCAM</b> Precision Optical Calibration Module .....	18
<b>P-ONE</b> Pacific Ocean Neutrino Experiment .....	17
<b>PVC</b> polyvinyl chloride .....	63
<b>PWN</b> Pulsar wind nebulae .....	5
<b>RHIB</b> rigid-hulled inflatable boat .....	44
<b>ROV</b> remotely operated vehicle .....	44
<b>SiPM</b> Silicon-photomultiplier .....	35
<b>SNRs</b> supernova remnants .....	2
<b>STRAW</b> Strings for Absorbtion Length in Water .....	19
<b>TDC</b> time-to-digital converter .....	37
<b>TIA</b> transimpedance amplifier .....	36
<b>TOT</b> time-over-threshold .....	37
<b>VENUS</b> Victoria Experimental Network Under the Sea .....	18
<b>VEOC</b> vertical electrical optical cable .....	46
<b>ZTL</b> Zentrales Technologie Labor .....	37

---

**List of Figures**

1.1	Cosmic ray spectrum with details . . . . .	3
2.1	Neutrino signatures . . . . .	12
2.2	Neutrino flux . . . . .	13
2.3	IceCube . . . . .	16
2.4	Baikal-GVD . . . . .	17
2.5	IceCube Upgrade . . . . .	18
2.6	Cascadia basin . . . . .	19
3.1	POCAM design . . . . .	23
3.2	PTFE-sphere design . . . . .	24
3.3	POCAM internal construction . . . . .	25
3.4	Comparison of optical and normal PTFE . . . . .	26
3.5	Emission profile with offsets . . . . .	27
3.6	Kapustinsky schematic . . . . .	28
3.7	Intensity and time profile of the Kapustinsky pulse driver . . . . .	29
3.8	LIDAR-type driver schematic . . . . .	30
3.9	Intensity and time profile of the LiDAR-type driver . . . . .	31
3.10	Kapustinsky redundancy modifications . . . . .	32
3.11	LIDAR-type driver redundancy modifications . . . . .	33
3.12	POCAM emitter layout . . . . .	34
3.13	Photodiode readout . . . . .	37
3.14	SiPM readout . . . . .	38
3.15	Flasher characterization setup . . . . .	40
3.16	Emission profile characterization setup . . . . .	41
4.1	Picture of STRAW mooring line assembly . . . . .	44
4.2	STRAW Technical Drawing . . . . .	45
4.3	Standard electronics STRAW-b . . . . .	47
4.4	Standard module design . . . . .	48
4.5	External mounting design . . . . .	52
4.6	Technical drawing STRAW-b . . . . .	55
4.7	InstrumentTray . . . . .	59
4.8	Durability test STRAW-b module . . . . .	61
5.1	P-ONE design study . . . . .	65
A.1	Freezing test POCAM . . . . .	69
A.2	Kapustinsky schematic . . . . .	70
A.3	LiDAR-type pulser schematic . . . . .	71
A.4	Kapustinsky redundancy schematic . . . . .	72
A.5	LiDAR-type pulser redundancy schematic . . . . .	73
A.6	Photodiode readout . . . . .	74
A.7	Pictures of VEOC separation . . . . .	75
A.8	Winding of the VEOC on instrument tray . . . . .	76
A.9	Pictures of instrument tray . . . . .	77

A.10 Pictures of the winch and the wire rope . . . . .	78
A.11 Vibration and shock test standard module . . . . .	79
A.12 Vibration and shock test PMT spectrometer . . . . .	79
A.13 Luzifer schematic . . . . .	80
A.14 LiDAmp schematic . . . . .	81
A.15 SciMon schematic . . . . .	82
A.16 Pressure test standard module . . . . .	83

## List of Tables

1 Emitter performance . . . . .	35
2 Weight of instrument tray components . . . . .	56



---

## References

- [1] Maurizio Spurio. *Particles and astrophysics: A multi-messenger approach*. Astronomy and astrophysics library. Cham et al.: Springer, 2015. ISBN: 978-3-319-08050-5.
- [2] Thomas K. Gaisser, Elisa Resconi, and Ralph Engel. *Cosmic rays and particle physics*. Second edition. Cambridge: Cambridge University Press, 2016. ISBN: 978-0-521-01646-9. DOI: 10.1017/CBO9781139192194.
- [3] Marica Branchesi. “Multi-messenger astronomy: gravitational waves, neutrinos, photons, and cosmic rays”. In: *Journal of Physics: Conference Series* 718 (2016), p. 022004. ISSN: 0004-637X. DOI: 10.1088/1742-6596/718/2/022004.
- [4] The Pierre Auger Collaboration. “The exposure of the hybrid detector of the Pierre Auger Observatory”. In: *Astroparticle Physics* 34.6 (2011), pp. 368–381. ISSN: 09276505. DOI: 10.1016/j.astropartphys.2010.10.001. URL: <http://arxiv.org/pdf/1010.6162v1>.
- [5] Tonia M. Venters et al. *Energetic Particles of Cosmic Accelerators I: Galactic Accelerators*. URL: <http://arxiv.org/pdf/1903.04634v1>.
- [6] Tonia M. Venters et al. *Energetic Particles of Cosmic Accelerators II: Active Galactic Nuclei and Gamma-ray Bursts*. URL: <http://arxiv.org/pdf/1903.04639v1>.
- [7] Kai Zuber. *Neutrino physics*. 2. ed. Series in high energy physics, cosmology and gravitation. Boca Raton, Fla.: CRC Press / Taylor & Francis, 2012. ISBN: 9781420064711.
- [8] Paolo Favali, Angelo DeSantis, and Laura Beranzoli. *Seafloor observatories: A new vision of the earth from the abyss*. Springer praxis books in geophysical sciences. Heidelberg: Springer, 2015. ISBN: 978-3-642-11373-4. DOI: 10.1007/978-3-642-11374-1. URL: <http://gbv.ebilib.com/patron/FullRecord.aspx?p=972305>.
- [9] *LIGO’s Dual Detectors*. 5.02.2020. URL: <https://www.ligo.caltech.edu/page/ligo-detectors>.
- [10] *A Worldwide Network — Advanced Virgo*. 25.3.2020. URL: <http://public.virgo-gw.eu/a-worldwide-network/>.
- [11] Kevin McFarland. *Neutrino Interactions*. URL: <http://arxiv.org/pdf/0804.3899v1>.
- [12] *Nuclear and radiochemistry*. S.l.: ELSEVIER, 2018. ISBN: 978-0-12-813643-0. URL: <http://search.ebscohost.com/login.aspx?direct=true&scope=site&db=nlebk&AN=1561690>.
- [13] IceCube Collaboration et al. “Measurement of South Pole ice transparency with the IceCube LED calibration system”. In: *Nuclear Instruments and Methods in Physics Research Section A: Accelerators, Spectrometers, Detectors and Associated Equipment* 711 (2013), pp. 73–89. ISSN: 01689002. DOI: 10.1016/j.nima.2013.01.054. URL: <http://arxiv.org/pdf/1301.5361v1>.
- [14] *Research Highlights: Neutrino Astronomy and Multimessenger Astrophysics*. 31.01.2020. URL: [https://icecube.wisc.edu/science/highlights/neutrino\\_astronomy](https://icecube.wisc.edu/science/highlights/neutrino_astronomy).
- [15] A. Faessler et al. “Search for the Cosmic Neutrino Background”. In: *Journal of Physics: Conference Series* 580 (2015), p. 012040. ISSN: 0004-637X. DOI: 10.1088/1742-6596/580/1/012040.

- 
- [16] Brent Follin et al. “First Detection of the Acoustic Oscillation Phase Shift Expected from the Cosmic Neutrino Background”. In: *Physical review letters* 115.9 (2015), p. 091301. DOI: 10.1103/PhysRevLett.115.091301.
- [17] Carlo Giunti and Chung Wook Kim. *Fundamentals of neutrino physics and astrophysics*. Oxford and New York: Oxford University Press, 2007. ISBN: 978-0-19-850871-7. URL: <http://site.ebrary.com/lib/academiccompletetitles/home.action>.
- [18] Brigitte Falkenburg and Wolfgang Rhode. *From Ultra Rays to Astroparticles: A Historical Introduction to Astroparticle Physics*. Dordrecht: Springer, 2012. ISBN: 978-94-007-5421-8. DOI: 10.1007/978-94-007-5422-5. URL: <http://dx.doi.org/10.1007/978-94-007-5422-5>.
- [19] J. A. Aguilar et al. “Transmission of light in deep sea water at the site of the Antares neutrino telescope”. In: *Astroparticle Physics* 23.1 (2005), pp. 131–155. ISSN: 09276505. DOI: 10.1016/j.astropartphys.2004.11.006.
- [20] IceCube Collaboration et al. “The IceCube Neutrino Observatory: Instrumentation and Online Systems”. In: *Journal of Instrumentation* 12.03 (2017), P03012–P03012. ISSN: 1748-0221. DOI: 10.1088/1748-0221/12/03/P03012. URL: <http://arxiv.org/pdf/1612.05093v2>.
- [21] Annarita Margiotta. “The KM3NeT deep-sea neutrino telescope”. In: *Nuclear Instruments and Methods in Physics Research Section A: Accelerators, Spectrometers, Detectors and Associated Equipment* 766 (2014), pp. 83–87. ISSN: 01689002. DOI: 10.1016/j.nima.2014.05.090. URL: <http://arxiv.org/pdf/1408.1392v1>.
- [22] Els De Wolf. “Data taking with KM3NeT”. In: *KM3NeT* (22.8.2019). URL: <https://www.km3net.org/data-taking-with-km3net/>.
- [23] A. D. Avrorin et al. “Baikal-GVD: first results and prospects”. In: *EPJ Web of Conferences* 209.3 (2019), p. 01015. DOI: 10.1051/epjconf/201920901015.
- [24] A. D. Avrorin et al. “Status of the Baikal-GVD Neutrino Telescope”. In: *EPJ Web of Conferences* 207 (2019), p. 01003. DOI: 10.1051/epjconf/201920701003.
- [25] IceCube Collaboration. “Neutrino emission from the direction of the blazar TXS 0506+056 prior to the IceCube-170922A alert”. In: *Science* 825 (2018), eaat2890. ISSN: 0036-8075. DOI: 10.1126/science.aat2890. URL: <http://arxiv.org/pdf/1807.08794v1>.
- [26] P. Padovani et al. “TXS 0506+056, the first cosmic neutrino source, is not a BL Lac”. In: *Monthly Notices of the Royal Astronomical Society: Letters* 484.1 (2019), pp. L104–L108. ISSN: 1745-3925. DOI: 10.1093/mnrasl/slz011. URL: <http://arxiv.org/pdf/1901.06998v1>.
- [27] *IceCube Upgrade - SFB1258*. 12.3.2020. URL: <http://www.sfb1258.de/news/first-upgrade-of-the-icecube-neutrino-observatory/1f23e1539d67cdea067eb35a237ef09d/>.
- [28] Aya Ishihara. *The IceCube Upgrade – Design and Science Goals*. URL: <http://arxiv.org/pdf/1908.09441v1>.
- [29] *Cascadia Basin — Ocean Networks Canada*. 28.2.2020. URL: <https://www.oceannetworks.ca/observatories/pacific/cascadia-basin>.
- [30] Dmitry Chirkin and IceCube Collaboration. “Evidence of optical anisotropy of the South Pole ice”. In: *International Cosmic Ray Conference* 33 (2013).

- 
- [31] Elisa Resconi, Martin Rongen, and Kai Krings. “The Precision Optical CALibration Module for IceCube-Gen2: First Prototype”. In: *Proceedings of 35th International Cosmic Ray Conference — PoS(ICRC2017)*. Ed. by Il Heung Park et al. Trieste, Italy: Sissa Medialab, 10-20 July, 2017, p. 934. DOI: 10.22323/1.301.0934.
- [32] M. G. Aartsen et al. “Measurement of Atmospheric Tau Neutrino Appearance with IceCube DeepCore”. In: *Phys. Rev. D* 99 (). URL: <https://arxiv.org/pdf/1901.05366>.
- [33] P. Bagley et al. *KM3NeT: Technical Design Report for a Deep-Sea Research Infrastructure in the Mediterranean Sea Incorporating a Very Large Volume Neutrino Telescope*. o. J. [2009].
- [34] Diego Real and David Calvo. “Nanobeacon: A time calibration device for KM3NeT”. In: *EPJ Web of Conferences* 207 (2019), p. 07002. DOI: 10.1051/epjconf/201920707002.
- [35] Kilian Holzapfel. “Testing the Precision Optical Calibration Modules in the Gigaton-Volume-Detector”. Master Thesis. Munich: Technical University Munich, 2019.
- [36] V.A.Balkanov et al. “In-situ measurements of optical parameters in Lake Baikal with the help of a Neutrino Telescope”. In: *Applied Optics* (1999).
- [37] Felix Henningsen. “Optical Characterization of the Deep Pacific Ocean: Development of an Optical Sensor Array for a Future Neutrino Telescope”. Master Thesis. Munich: Technical University Munich, 19.07.2018.
- [38] M. Boehmer et al. “STRAW (STRings for Absorption length in Water): pathfinder for a neutrino telescope in the deep Pacific Ocean”. In: *Journal of Instrumentation* 14.02 (2019), P02013–P02013. ISSN: 1748-0221. DOI: 10.1088/1748-0221/14/02/P02013. URL: <http://arxiv.org/pdf/1810.13265v5>.
- [39] Bal Seal Engineering Co. *Coefficient of thermal expansion for various materials at different temperatures: Technical Report TR-18 (Rev. F)*.
- [40] Berghof Fluoroplastics GmbH. *Optical PTFE production*. 9.3.2020. URL: <https://www.berghof-fluoroplastics.com/de/kompetenzen/#c2103>.
- [41] B. K. Lubsandorzhev and Y. E. Vyatchin. “Studies of ”Kapustinsky’s” light pulser timing characteristics”. In: (2006). URL: <http://arxiv.org/pdf/physics/0410281v1>.
- [42] Efficient Power Conversion Corporation. *EPC2001C - Enhancement Mode Power Transistor*. 2019. URL: [www.epc-co.com](http://www.epc-co.com).
- [43] *South Pole ICE model SPICE*. 21.6.2012. URL: <https://icecube.wisc.edu/~dima/work/WISC/ppc/spice/>.
- [44] Mohamed Atef and Horst Zimmermann. *Optical Communication over Plastic Optical Fibers: Integrated Optical Receiver Technology*. Vol. 172. Springer Series in Optical Sciences. Berlin and Heidelberg: Springer, 2013. ISBN: 978-3-642-30387-6. DOI: 10.1007/978-3-642-30388-3. URL: <http://dx.doi.org/10.1007/978-3-642-30388-3>.
- [45] Horst K. Zimmermann. *Integrated Silicon Optoelectronics*. 2. ed. Vol. 148. Springer Series in Optical Sciences. Berlin, Heidelberg: Springer-Verlag Berlin Heidelberg, 2010. ISBN: 978-3-642-01520-5. DOI: 10.1007/978-3-642-01521-2. URL: <http://dx.doi.org/10.1007/978-3-642-01521-2>.

- 
- [46] Robert Keim. “Negative Feedback, Part 8: Analyzing Transimpedance Amplifier Stability”. In: *All About Circuits* (6.12.2015). URL: <https://www.allaboutcircuits.com/technical-articles/negative-feedback-part-8-analyzing-transimpedance-amplifier-stability/>.
- [47] Elisa Resconi. *PLEvM - TOWARDS A PLANETARY NEUTRINO MONITORING SYSTEM*. XVIII International Workshop on Neutrino Telescopes, 2019. DOI: 10.5281/ZENODO.3520454.
- [48] *Abyssal plain: Geology*. 11.4.2020. URL: <https://www.britannica.com/science/abyssal-plain>.
- [49] Christian Fruck. *International Workshop on Next Generation Nucleon Decay and Neutrino Detectors (NNN18): STRAW - STRings for Absorption length in Water*. 2018. URL: <https://meetings.triumf.ca/indico/event/27/timetable/#all.detailed>.
- [50] *Vitrovex by Nautilus Marine Service GmbH*. 30.3.2020. URL: <https://www.vitrovex.com/>.
- [51] Imants G. Priede et al. “The potential influence of bioluminescence from marine animals on a deep-sea underwater neutrino telescope array in the Mediterranean Sea”. In: *Deep Sea Research Part I: Oceanographic Research Papers* 55.11 (2008), pp. 1474–1483. ISSN: 09670637. DOI: 10.1016/j.dsr.2008.07.001.
- [52] S. H. D. Haddock and J. F. Case. “Bioluminescence spectra of shallow and deep-sea gelatinous zooplankton: ctenophores, medusae and siphonophores”. In: *Marine Biology* 133.3 (1999), pp. 571–582. ISSN: 0025-3162. DOI: 10.1007/s002270050497.
- [53] *PG-Seilzugglieder — www.pfeifer.info*. 6.4.2020.
- [54] Andreas Gaertner. “Development of an optical sensor system for the characterization of Cascadia Basin, Canada”. Master Thesis. Technical University Munich, 11.12.2018.
- [55] Bürkert Fluid Control Systems. “Chemical-Resistance-Chart”. In: (2018). URL: [https://www.buerkert.de/de/content/download/9318/335016/file/DE\\_Bestaendig\\_D.pdf](https://www.buerkert.de/de/content/download/9318/335016/file/DE_Bestaendig_D.pdf).
- [56] Würth. *Dimensionierung von metrischen Schraubenverbindungen*. URL: [https://www.wuerth-industrie.com/web/media/de/pictures/wuerthindustrie/technikportal/dinokapitel/Kapitel\\_06\\_DINO\\_tech\\_Teil.pdf](https://www.wuerth-industrie.com/web/media/de/pictures/wuerthindustrie/technikportal/dinokapitel/Kapitel_06_DINO_tech_Teil.pdf).
- [57] Hristo Ivanov. “Corrosion Protection Systems in Offshore Structures”. In: *Honors Research Projects* 281 (2016).
- [58] “Was das Feuerverzinken wirklich kann”. In: *JOT Journal für Oberflächentechnik* 50.2 (2010), pp. 34–36. DOI: 10.1007/BF03252512.
- [59] Dietmar Gross et al. *Technische Mechanik 1: Statik*. 14., aktualisierte Auflage. Lehrbuch. 2019. ISBN: 978-3-662-59156-7.
- [60] item GmbH. “Technische Daten zu Profile”. In: (). URL: [https://catalog.item24.de/images/medienelemente/DOK/DATA/DOK\\_DATA\\_profil-tech-daten\\_SDE\\_AIN\\_V2.pdf](https://catalog.item24.de/images/medienelemente/DOK/DATA/DOK_DATA_profil-tech-daten_SDE_AIN_V2.pdf).
- [61] *Produktdetails — item Industrietechnik GmbH*. 14.04.2020. URL: <https://product.item24.de/produkte/produktkatalog/produktdetails/products/konstruktionsprofil-8-1001042794/profil-8-80x80-natur-2627/>.

